



ARCHITECTURE & ENGINEERING

Volume 9
Issue 3
September, 2024



By Architects. For Architects.
By Engineers. For Engineers.

Architecture
Civil and Structural Engineering
Mechanics of Materials
Building and Construction
Urban Planning and Development
Transportation Issues in Construction
Geotechnical Engineering and Engineering Geology
Designing, Operation and Service
of Construction Site Engines

eISSN: 2500-0055
<http://aej.spbgasu.ru/>

Architecture and Engineering

Volume 9 Issue 3 (2024)

ISSN: 2500-0055

Editorial Board:

Prof. Askar Akaev (Kyrgyzstan)
Prof. Emeritus Demos Angelides (Greece)
Mohammad Arif Kamal (India)
Prof. Stefano Bertocci (Italy)
Prof. Tigran Dadayan (Armenia)
Prof. Milton Demosthenous (Cyprus)
Prof. Josef Eberhardsteiner (Austria)
Prof. Sergei Evtukov (Russia)
Prof. Georgiy Esaulov (Russia)
Prof. Andrew Gale (UK)
Prof. Theodoros Hatzigogos (Greece)
Prof. Santiago Huerta Fernandez (Spain)
Yoshinori Iwasaki (Japan)
Prof. Jilin Qi (China)
Prof. Nina Kazhar (Poland)
Prof. Gela Kipiani (Georgia)
Prof. Darja Kubečková (Czech Republic)
Prof. Hoe I. Ling (USA)
Prof. Evangelia Loukogeorgaki (Greece)
Prof. Jose Matos (Portugal)
Prof. Dietmar Mähner (Germany)
Prof. Saverio Mecca (Italy)
Prof. Menghong Wang (China)
Stergios Mitoulis (UK)
Prof. Valerii Morozov (Russia)
Prof. Aristotelis Naniopoulos (Greece)
Sandro Parrinello (Italy)
Prof. Paolo Puma (Italy)
Prof. Jaroslaw Rajczyk (Poland)
Prof. Marlena Rajczyk (Poland)
Prof. Sergey Sementsov (Russia)
Anastasios Sextos (Greece)
Eugene Shesterov (Russia)
Prof. Alexander Shkarovskiy (Poland)
Prof. Emeritus Tadatsugu Tanaka (Japan)
Prof. Sergo Tepnadze (Georgia)
Sargis Tovmasyan (Armenia)
Marios Theofanous (UK)
Georgia Thermou (UK)
Prof. Yeghiazar Vardanyan (Armenia)
Ikujiro Wakai (Japan)
Vardges Yedoyan (Armenia)
Prof. Askar Zhusupbekov (Kazakhstan)
Prof. Konstantin Sobolev (USA)
Michele Rocca (Italy)
Prof. Sergey Fedosov (Russia)
Francesco Di Paola (Italy)

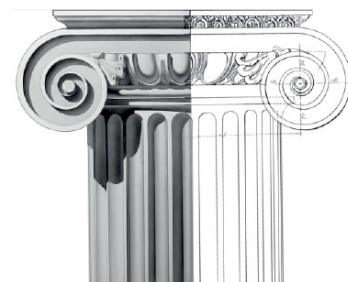


Editor in Chief:

Professor Evgeny Korolev (Russia)

Executive Editor:

Anastasia Sidorova (Russia)



CONTENTS

Architecture

- 3 **Amany Sanad Fouad,
Mohamed Ezzeldin, Ayman Assem**
A novel framework for the application
of topology optimization in lightweight
structures

Building Information Modeling

- 15 **Bani Ferial Brahmī,
Souad Sassi-Boudemagh**
BIM implementation for heritage
renovation throughout project lifecycle:
current use, benefits, and barriers
- 27 **Qiaofeng Shen, Chen Shen, Xun Liu,
Yuan Jia, Jia Qian**
Research on the standardization
and visualization platform for monitoring
and testing data of metro civil facilities
based on big data

Civil Engineering

- 39 **Farid Boursas, Rafik Boufarh,
Abderrahmani Sifeddine**
Experimental investigation on the shear
resistance of I-shaped perforated
connectors in composite beams
- 53 **Viktoria Il'ina, Valeria Strokova,
Vladimir Erofeev, Irina Stepina**
Photo-reactive acrylic-alkyd composition
with biocide additive for wood protection
coating development
- 63 **Terentii Afanasevich Kornilov,
Petr Anatolevich Fedotov,
Alexey Terentevich Kornilov**
Reducing the influence of thermal bridges
in the basement slab of cast-in-situ frame
buildings in extremely cold regions
- 75 **Xu Yun, Chen Bin, Wang Xuejiao,
Liu Yingxin, Wang Heng,
Aleksandr Chernykh, Egor Danilov,
Pavel Koval, Du Mingli, Zhang Zhonghua,
Shi Saisai, Song Chunbo**
A comparison of shear strength
calculation methods for perfobond leiste
shear connectors using the controlled
variable method

Geotechnical Engineering

- 81 **Feknous Hadjer, Della Noureddine,
Denine Sidali, Missoum Benziane Mehdi,
Flitti Abdelhamid, Sert Sedat, Ertan Bol,
Apkyn Ozocak**
Investigation of the shear strength
of reinforced silty sand

Architecture and Engineering

peer-reviewed scientific journal
Start date: 2016/03
4 issues per year

Founder, Publisher:

Saint Petersburg State University
of Architecture and Civil Engineering

Indexing:

Scopus, Russian Science Citation Index,
Directory of Open Access Journals (DOAJ),
Google Scholar, Index Copernicus,
Ulrich's Periodicals Directory, WorldCat,
Bielefeld Academic Search Engine
(BASE), Library of University of Cambridge
and CyberLeninka

Corresponding address:

4 Vtoraya Krasnoarmejskaja Str.,
St. Petersburg, 190005, Russia

Website: <http://aej.spbgasu.ru/>

Phone: +7(812) 316 48 49

Email: aejeditorialoffice@gmail.com

Date of issue: September 30, 2024

The Journal was re-registered
by the Federal Service
for Supervision of Communications,
Information Technologies and Mass
Communications (Roskomnadzor)
on May 31, 2017;
registration certificate of media organization
EI No. FS77-70026

A NOVEL FRAMEWORK FOR THE APPLICATION OF TOPOLOGY OPTIMIZATION IN LIGHTWEIGHT STRUCTURES

Amany Sanad Fouad, Mohamed Ezzeldin, Ayman Assem*

Ain Shams University, Cairo, Egypt

*Corresponding author's email: ayman.assem@eng.asu.edu.eg

Abstract

Introduction: Topology optimization has been widely used in the fields of mechanical and structural engineering. In the field of architecture, especially in the context of lightweight structures, a strong understanding of programming is essential for meaningful involvement. The **purpose of the study** was to establish a fundamental framework that facilitates the seamless implementation of topology optimization in the design of lightweight structures by architects. **Methods:** This work employed a deductive approach to analyze six case studies that involve the application of topology optimization in various lightweight constructions. The analysis was conducted based on a predefined set of criteria. Additionally, the deductive technique was used to establish a framework for implementing topology optimization in the design of lightweight structures. Finally, the framework was used to create an optimized lightweight structure (a pentagonal Roman vault). **Findings:** An analysis of all case studies was conducted using two distinct processes: the form-finding process and the fabrication process. This inquiry aimed to determine the procedural framework involved in the design and fabrication process of each case study. The underlying framework was derived through an analytical comparison of these six case studies. This framework enables the production of an optimized lightweight structure. **Novelty:** This study presents significant findings on topology optimization and its use in lightweight structures, offering essential insights for architects seeking to create aesthetically pleasing and distinctive architectural forms that prioritize high stiffness and low mass.

Keywords: lightweight structures, topology optimization, additive manufacturing.

Introduction

Topology optimization is a mathematical methodology that aims to optimize structures by taking into account several design factors, including applied loads, supports, available design domain, materials, and cost considerations. Using this approach in the initial stages of the design process allows for the creation of designs that have minimal mass and optimal stiffness (Ma et al., 2021; Tedeschi, 2014). The generation of outputs from topology optimization algorithms might pose challenges, necessitating subsequent refinement to ensure the manufacturability of the final result. In certain circumstances, it is possible to directly manufacture the results of topology optimization through the use of additive manufacturing techniques (Woo, 2020). Topology optimization is a form of generative design that leverages the computer's ability to perform rapid computations to generate shapes (Tedeschi, 2014). Topology optimization has drawn the attention of many architects among the different generative design tools due to its capacity to produce attractive organic forms by identifying voids in continuum structures (Liu et al., 2019). More importantly, topology optimization is a performance-based design method that seeks the most efficient

structural form, which means that the resulting configuration corresponds to an optimized material arrangement (Javadi Moghaddam et al., 2023; Xie, 2022). Topology optimization plays a significant role in the field of architecture as it helps determine the optimal placement and dimensions of architectural components. Designers can optimize mechanical components or parts using this technique, which often involves reducing material usage. Topology optimization offers cost-saving solutions thanks to lightweight structures and efficient design procedures. In addition, creating optimal structures that exhibit such characteristics as lightweightness, durability, and cost-effectiveness is beneficial (Liu et al., 2022; Yıldırım, 2022).

Topology optimization solves multiple problems. It has numerous advantages: creating cost-effective and lightweight solutions by reducing unnecessary weight and raw material usage. Design constraints and performance targets are considered early in the design process, resulting in a quicker final design through topology optimization. Topology optimization is increasingly being adopted by various industrial sectors in response to the growing demand for eco-friendly options, aiming to reduce unnecessary material waste for sustainable perfection (Tedeschi, 2014).

There are certain drawbacks associated with topology optimization that should be considered:

a. The use of intricate patterns may have both benefits and drawbacks.

b. Early investments in software, training, and computational resources may be necessary.

c. Manufacturing incurs significant costs due to the expensive nature of some manufacturing methods required for topology-optimized designs.

d. Designers may need to establish manual constraints in order to ensure the feasibility of manufacturing and meet other requirements.

e. Training is a necessary component for the appropriate utilization of topology optimization technologies.

f. Limited use of primary resources: The use of specific raw materials in topology-optimized designs may be subject to constraints or limitations, depending on input parameters.

g. The output quality depends on the accuracy of the input parameters provided by the designer (Sigmund and Maute, 2013).

Additionally, these data-driven topology optimization methods enable the calculation of resistances, damage properties, and structural connections of real materials. Furthermore, they facilitate the exploration of unconventional structural systems and the identification of novel and efficient structural solutions suitable for specific circumstances. The approaches discussed in this study include solid isotropic material with penalization (SIMP), evolutionary structural optimization (ESO), bi-directional evolutionary structural optimization (BESO), and level-set method (LSM) (Bao et al., 2020; Woo, 2020).

Methodology

The methodology employed in this study is based on examining six individual case studies that have implemented a specific topology optimization technique. The selection of these case studies was primarily based on the criteria established by the authors. The mentioned criteria include the following aspects: first, the structure must have a lightweight composition; second, the structure must undergo digital manufacturing using various techniques; third, it must have been designed using one of the topology optimization approaches; and finally,

it must have been constructed within the past decade. The selected case studies, in sequential order, are Pavilion X-Form 1.0 (Bao et al., 2019, 2020), Pavilion X-Form 2.0 (Bao et al., 2022), VOLU Dining Pavilion (Bhooshan, 2017; Louth et al., 2017), Tailored Biocomposite Canopy (Dahy et al., 2020; Martins et al., 2020; Rihaczek et al., 2020), Trabeculae Pavilion (Naboni et al., 2019), and Cloud Pavilion 2.0 (Chen et al., 2019) as shown in Fig. 1.

There are four case studies that exhibit continuum structures, while two case studies demonstrate discrete structures. The pavilions known as X-Form 1.0 and X-Form 2.0, both created by the same team, along with the VOLU Pavilion and the Tailored Biocomposite Canopy, might be seen as examples of continuum structures. Furthermore, both the Trabeculae Pavilion and the Cloud Pavilion 2.0 can be classified as discrete structures. An analysis of all case studies was conducted using two distinct processes: the form-finding process and the production and assembly process. Next, we shall proceed to deduce the sequence of steps involved in the process of designing and constructing each case study, as outlined in Table 2. A comparative analysis was conducted, as depicted in Table 1, to examine the six case studies in relation to various aspects. These aspects include the structural type (with the exception of the Tailored Biocomposite Canopy, all case studies feature a shell structure), whether the structure is considered as continuum or discrete, the approach employed for form finding, the specific topology optimization method utilized (ranging from SIMP to BESO), the materials used, the software utilized, and the fabrication technique employed. The analysis process is a crucial component in establishing the framework for implementing topology optimization in a lightweight structure.

Discussion

To effectively implement topology optimization in the design of lightweight structures, it is important to have the basic geometric configuration of the structure before starting the topology optimization procedure. Based on the examination of prior case studies, it has been inferred that there are two primary procedures for implementing topology optimization in the context of lightweight structures. These procedures encompass the form-finding

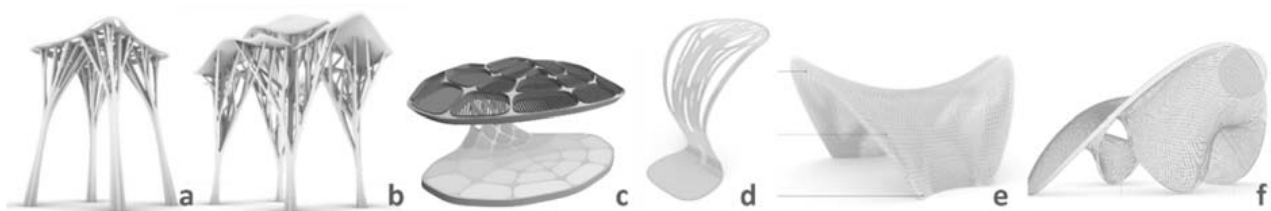


Fig. 1. Six case studies used in the analysis: a — Pavilion X-Form 1.0; b — Pavilion X-Form 2.0; c — VOLU Dining Pavilion; d — Tailored Biocomposite Canopy; e — Trabeculae Pavilion, f. Cloud Pavilion 2.0

Table 1. Comparative analysis of the six case studies applying topology optimization in lightweight structures

Project name	Type of structure	Form finding	TO method	Materials	Software	Fabrication technique
X-Form 1.0 & 2.0 Pavilions	Continuum structure	Tree-like structure form	BESO method	3D printing of fireproof polymeric materials / PETG materials	Ameba in Rhino-Grasshopper	Large-scale robotic 3D printing
VOLU Dining Pavilion	Continuum structure	Curvy clamshell-like structure	SIMP method	Stainless steel, aluminum, and wood	Altair HyperWorks and Altair OptiStruct	CNC laser cutting
Tailored Bio-composite Canopy	Continuum structure	single-curved canopy with no connections	SIMP method	Natural fiber materials / continuous flax fibers	Galapagos & Millipede in Rhino-Grasshopper	TFP (tailored fiber placement) method
Trabeculae Pavilion	Discrete structure	the materialization logic of trabeculae, the interior cells that form the bone microstructure	SIMP method	High-resistance biopolymer	Millipede, Karamba in Rhino-Grasshopper, and Ansys	FDM (fused deposition modeling)
Cloud Pavilion 2.0	Discrete structure	generated using a structural performance-based topological optimization algorithm	SIMP method	3D printing material	Millipede in Rhino-Grasshopper	Robotic 3D printing

Table 2. Comparative analysis of the workflow in the six case studies

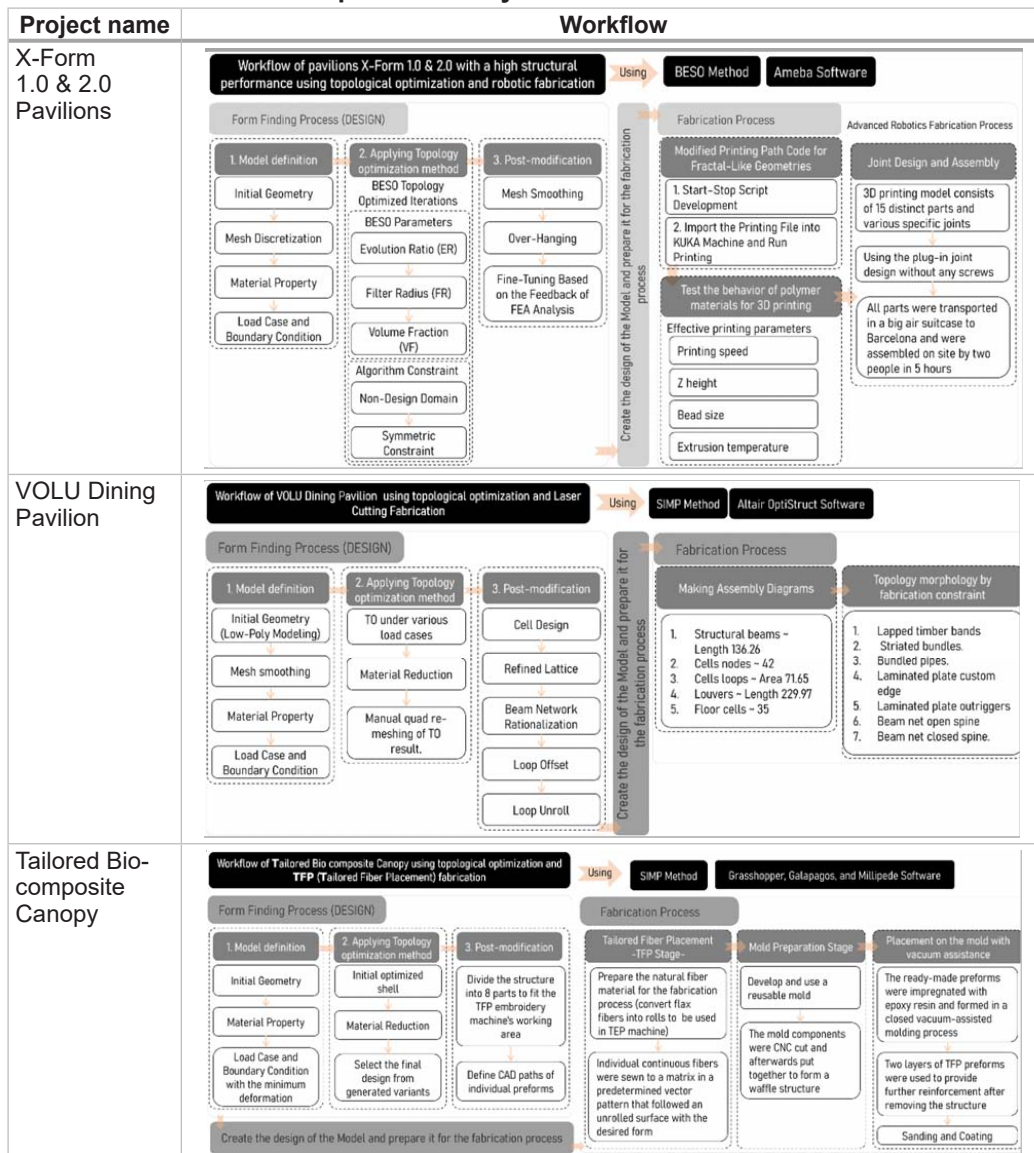


Table 2 (ending)

Project name	Workflow
Trabeculae Pavilion	<p>Workflow of Trabeculae Pavilion using topological optimization and Additive Manufacturing (Fused Deposition Modeling) Using SIMP Method, Grasshopper, Millipede, Karamba, and Ansys Software</p> <p>Form Finding Process (DESIGN)</p> <ul style="list-style-type: none"> 1. Model definition: Initial Geometry (form definition), Applied loads, External Constrains, Cellular Structure 2. Applying Topology optimization method: SIMP TO method, Finite Element Analysis, Define main compression trajectories, Stiffness factor 3. Post-modification: Cell Orientation, Cell topology, Cell thickness, Load-responsive lattice structure <p>Fabrication Process</p> <ul style="list-style-type: none"> Printing Material, Preparation and Testing: 1. Material Comparison, 2. Anisotropy Testing, 3. Material and Printing Refinement Assembly Process: Tectonic System (pre-assembled clusters), Assembly sequence of the clusters Additive Manufacturing: Tessellation, Geometry Optimization, Intralayer Design <p>Vertical flow: Create the design of the Model and prepare it for the fabrication process</p>
Cloud Pavilion 2.0	<p>Workflow of Cloud pavilion 2.0 large-scale robotic 3D printed spatial structure -Discrete system- Using SIMP Method, Using Millipede plugin in Rhino-Grasshopper</p> <ol style="list-style-type: none"> 1. Define the mesh form for the design object. Including Parameters like Thickness, Mesh Density, UV Ratio 2. Design a toolpath to create cellular or other types of supporting structures for space-filling. to check: -If any loaded element exceeds the material strength, - Structural failure from simulation results through modification on mesh parameters in first step. 3. Apply load constraints. 4. Analyze overall structural performance. Make two tests to analyze the structural stiffness. <ul style="list-style-type: none"> using a new and faster approach to reducing modification time and achieving a more successful robotic toolpath design process. one on a printed beam structure connected by five space frame pieces the other on cantilever strut with a total length of 1 m and a combination of n number of space frame parts. 5. Apply 2D topology optimization simulation on a specific mesh surface by using boundary conditions of four fixed supports, 3D printing material, and under gravity load conditions (self-weight). The mesh is divided into 380 intervals in U direction and 42 intervals in V direction and has total 15960 discrete mesh units with 16340 mesh vertices. The topologic-optimized mesh is divided into three zones based on its stiffness level, from weakest to strongest.

process and the fabrication process. The form-finding process refers to the analytical and optimization procedures involved in the design of a structure. The process has three distinct stages: model definition, application of the topology optimization method, and post-modification. The fabrication process has four distinct phases, including the selection of an appropriate digital manufacturing technique, the preparation and testing of materials, the design of fabrication and joints, and the final assembly phase. as can be seen in Fig. 2.

Form-finding process

Model definition

The initial stage, referred to as “Model Definition”, includes a series of four sequential processes. The first step involves establishing the boundary domain for the structure in question, to which the subsequent topology optimization will be applied. The process of mesh discretization involves dividing the mesh into smaller sections to accurately determine the positions of loads. Additionally, it is necessary to specify the material properties by providing the value

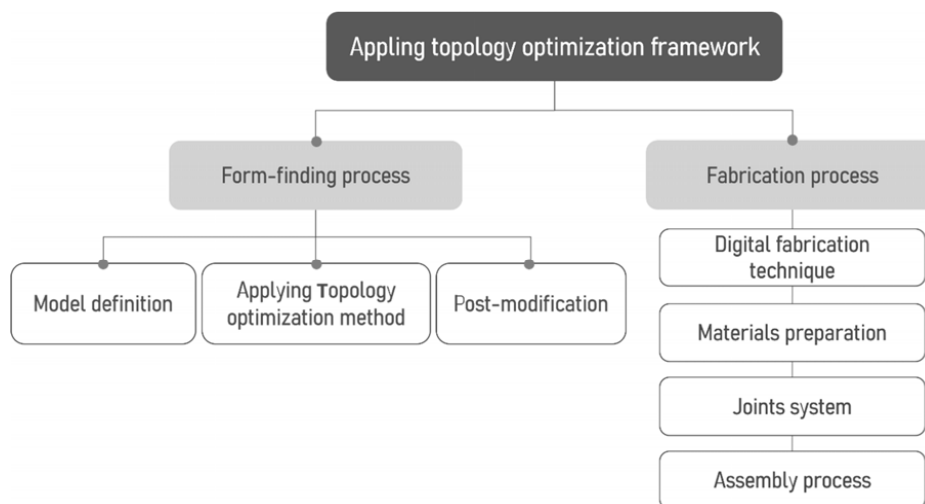


Fig. 2. Primary process of applying topology optimization to lightweight structures (created by the authors)

of Young's modulus in gigapascals (GPa) and the corresponding Poisson's ratio. In conclusion, the applied loads include external loads, the structure's self-weight, the positioning of supports, and structural constraints such as specified openings, doors, or windows, as depicted in Fig. 3.

The authors have developed and presented a case study in order to adhere to and implement the established framework. The chosen design for the vault is a pentagonal Roman vault, which is inspired by

the Mortuary Chapel for the Soriano Manzanet family (architizer.com, 2023). The vault has dimensions of 2.4 m for each side and a height of 2.8 m. It features a total of five openings. Later, the surface was discretized into smaller components to accurately determine the locations of the applied loads. Young's modulus and Poisson's ratio for the PLA material used in 3D printing were determined to be 2.7 GPa and 0.3, respectively. The placements of loads and supports were specified as depicted in Fig. 4.

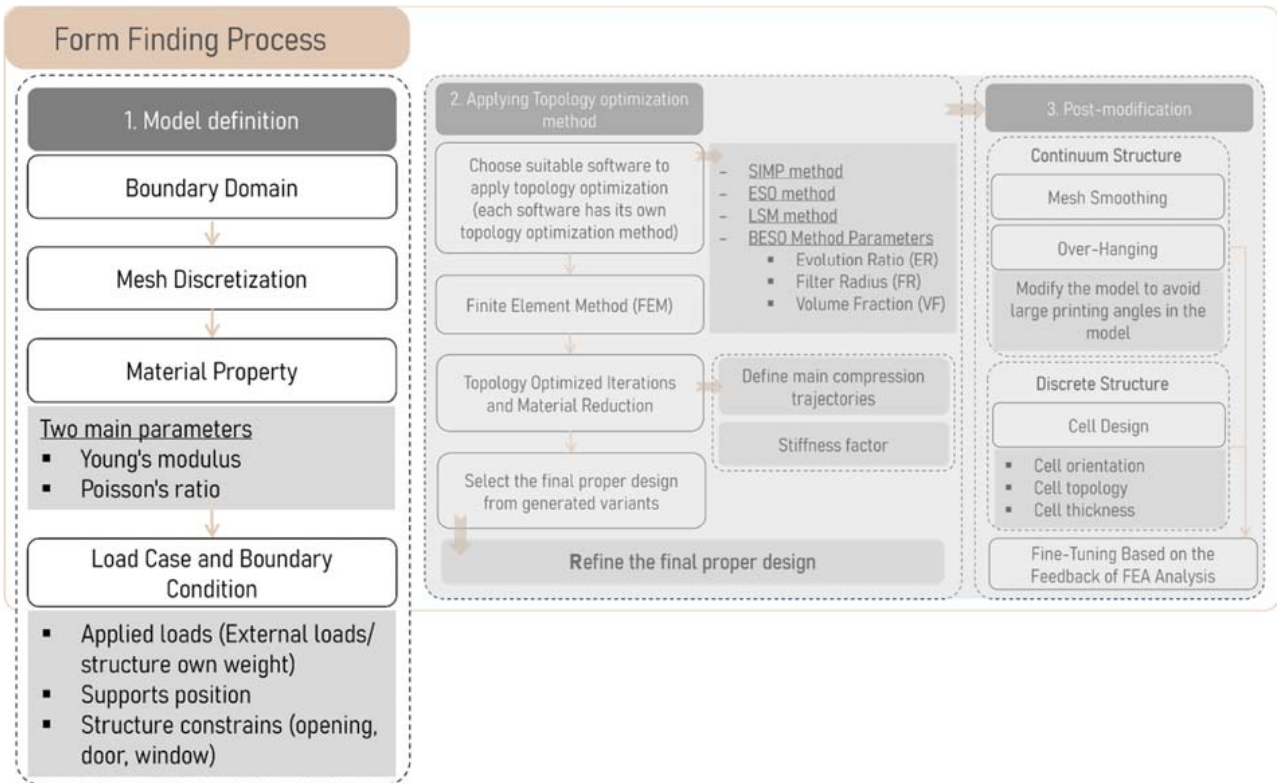


Fig. 3. Workflow of the form-finding process, model definition phase (created by the authors)

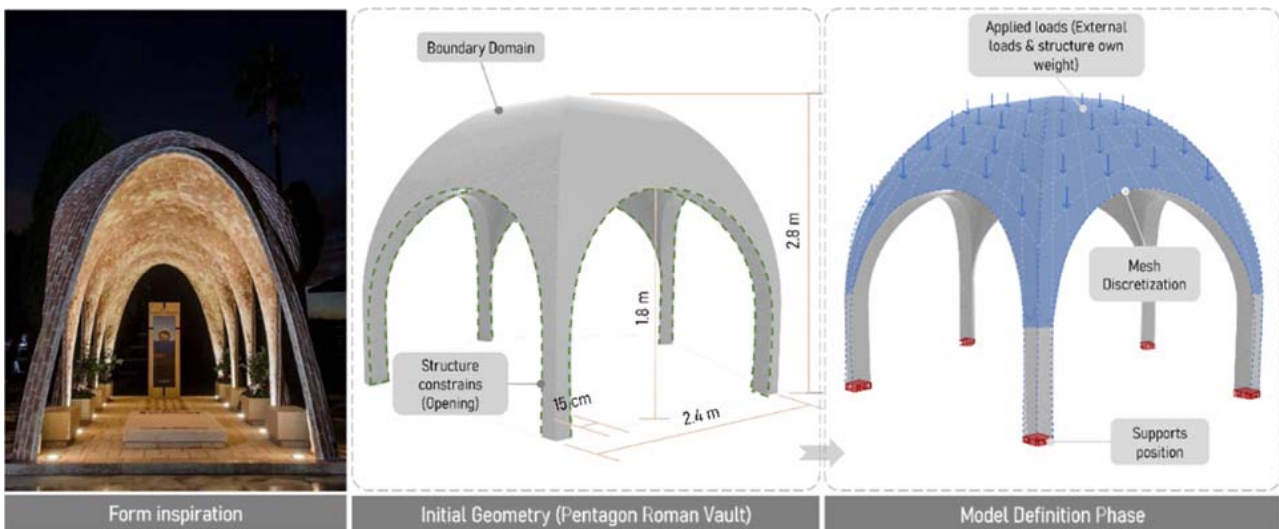


Fig. 4. Case study's model definition phase (created by the authors)

Applying the topology optimization method

The phase under consideration holds significant importance within the form-finding process, as it involves the application of topological optimization techniques. The first step involves selecting the appropriate software. The analytical process subsequently employs the finite element method (FEM) and facilitates material reduction through the software. This results in the generation of several iterations. Ultimately, the selection of the definitive design depends on the final decision. It is worth noting that an increase in the number of optimization iterations directly correlates with a higher level of accuracy in the outcome. If necessary, the designer has the ability to refine the output-optimized design, as depicted in Fig. 5.

The selected case study involves the use of the tOpos plugin in Rhino-Grasshopper, which utilizes the SIMP (Solid Isotropic Material with Penalization) technique. The optimization iteration numbers were set to 50, 100, 200, 300, and 500, as can

be seen in Fig. 6. The final design selected is the one obtained after 500 iterations of optimization, as it has been determined to be the most accurate. The finite element approach, as depicted in Fig. 7, was implemented using tOpos plugin.

Post-modification

The final stage of the form-finding process involves post-modification. During this step, the results obtained from the topological optimization process are adjusted and prepared for the subsequent production procedure. The above-mentioned phase may undergo modification based on whether the structure in question is continuum or discrete in nature. In the case of a continuum structure, the post-modification process involves two consecutive steps, namely mesh smoothing and overhang reduction. Overhang reduction refers to modifying a model to reduce the presence of steep printing angles. If the structure is discrete, the post-modification phase is established during the cell design process with the objective of determining the cell's orientation, topology, and thickness. Subsequently, the model undergoes fine-

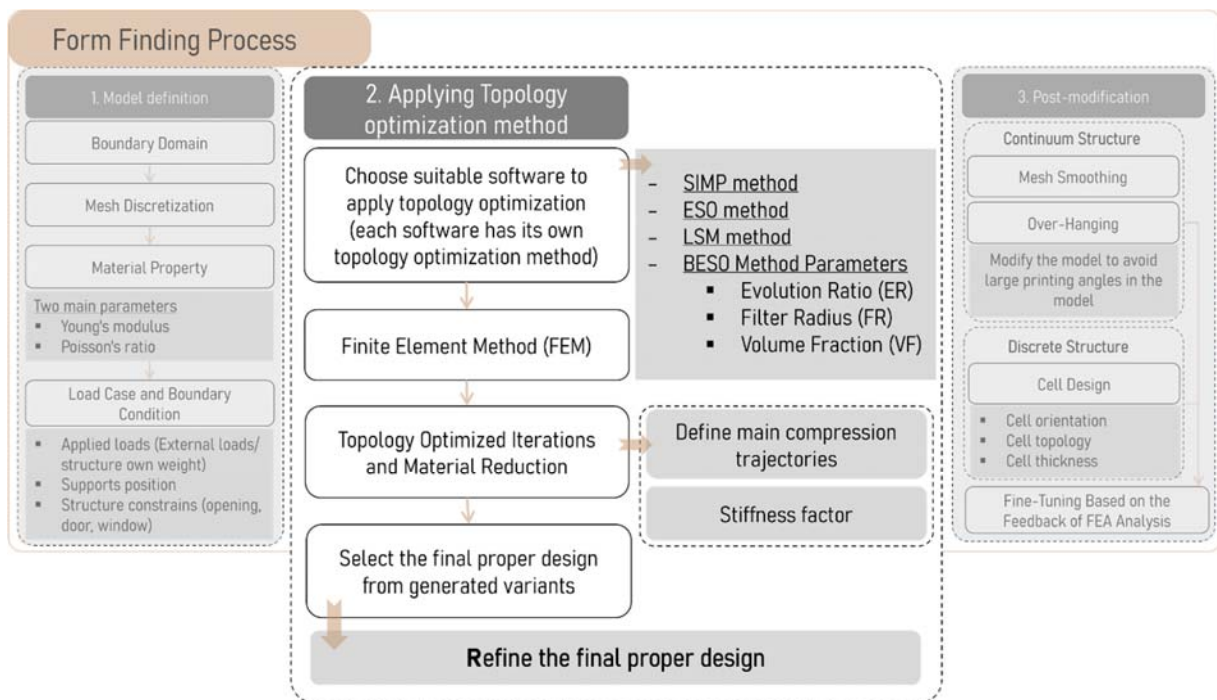


Fig. 5. Workflow of the form-finding process, applying topology optimization method phase (created by the authors)

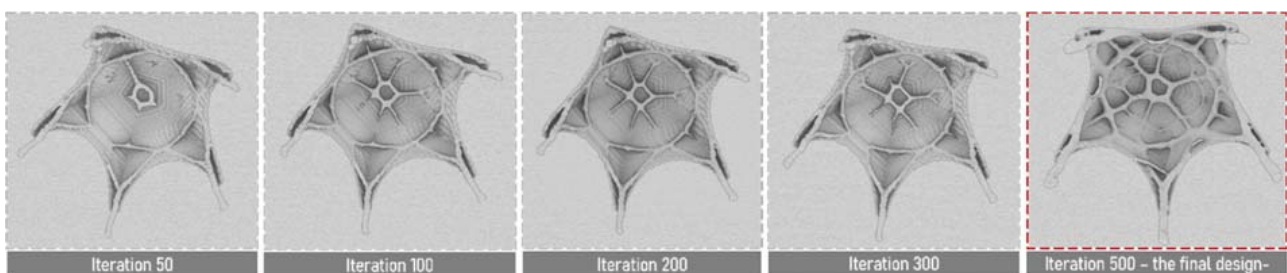


Fig. 6. Topology optimized iterations and material reduction (created by the authors)

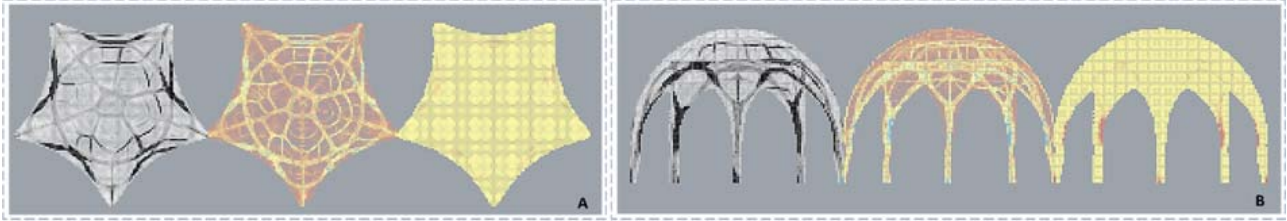


Fig. 7. Topology optimization and FEA. a. Layout; b. Elevation by tOpos plugin in Rhino-Grasshopper (created by the authors)

tuning through the incorporation of inputs obtained from the FEA, as shown in Fig. 8.

The case study model exhibits a continuum structure, thereby necessitating the use of a mesh smoothing technique. Upon reaching the conclusion

of this stage, all advancements related to the case study have been finalized, resulting in the production of the ultimate outcome, as depicted in Fig. 9.

The graphical representation in Fig. 10 illustrates the disparity between the basic geometry and the

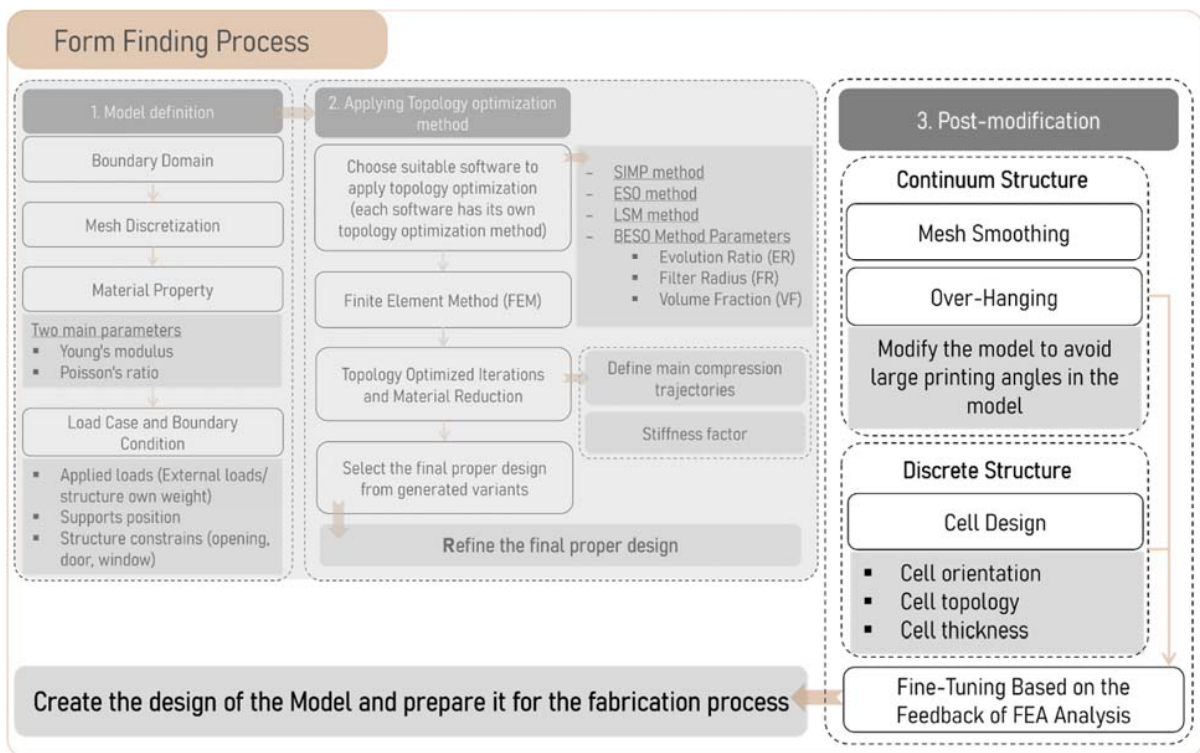


Fig. 8. Workflow of the form-finding process, post-modification phase (created by the authors)

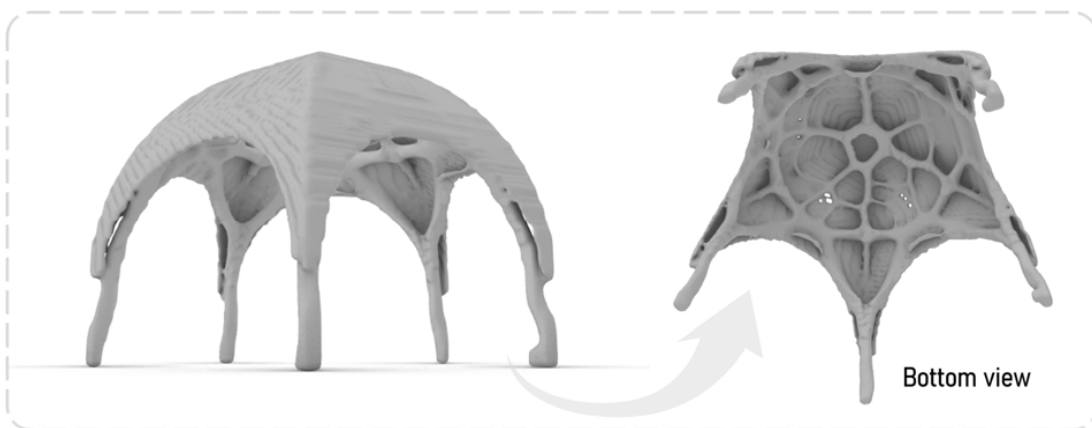


Fig. 9. Final optimized model after the form-finding process (created by the authors)

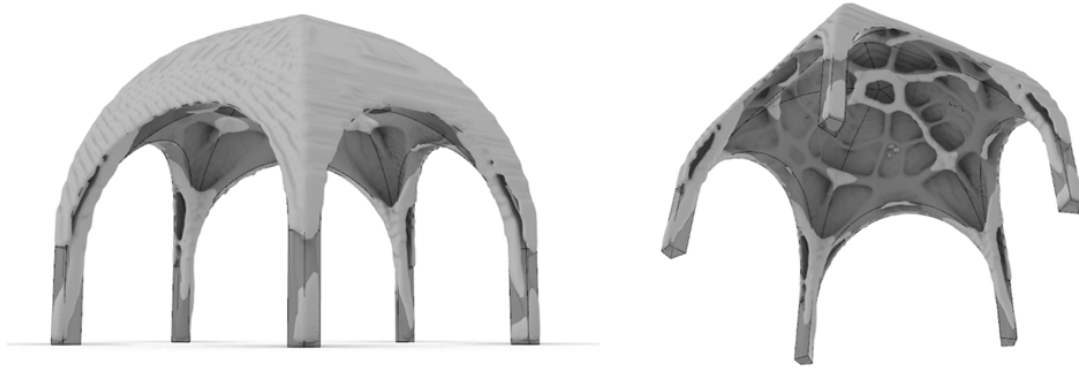


Fig. 10. Initial geometry and final optimized design shown together, illustrating the material reduction that occurred from topology optimization (created by the authors)

optimized model, highlighting the extent of material reduction resulting from the process of topology optimization. The design's aesthetic draws inspiration from natural elements and is characterized by an abundance of organic forms. Fig. 11 illustrates the comprehensive script used in the tOpos plugin within the Grasshopper environment. In the context of this study, it can be observed that each phase is associated with a specific color. The color beige is assigned to the model definition phase, blue is designated for the application of the topology optimization method, and gray is utilized to represent the post-modification phase.

Fabrication Process

The fabrication process has four distinct phases, including the selection of an appropriate digital manufacturing technique, the preparation and testing of materials, the design of fabrication and joints, and the final assembly phase. The choice of digital manufacturing technology is a crucial aspect of the fabrication process. Next, the appropriate material is selected for this specific approach. In some cases, it becomes crucial to prioritize material selection over fabrication techniques, or alternatively, the choice of technique is contingent upon the designated material. Therefore, in such scenarios, the selection of materials takes precedence over the selection of fabrication techniques. The material preparation and testing process involves three distinct steps: material comparison, anisotropy testing, and material and printing refinement. During the fabrication and joint design phase, it is necessary to divide the model into components that can fit inside the working area of the printing machine. It is also important to establish a comprehensive system for joints, encompassing various forms of connections. During the assembly process, it is imperative to develop a tectonic system that effectively partitions the structure into

smaller components, known as pre-assembled clusters. It is also crucial to establish a well-defined assembly sequence for these clusters in order to successfully install the entire structure, as can be seen in Fig. 12.

The optimized output model for the case study was printed using a small-scale desktop 3D printer (Ender-3 V2) and PLA+ filament material. Fig. 13 shows the printing process, and Fig. 14 shows the final printed optimized model.

The following content presents a comprehensive framework for implementing topology optimization in the design of lightweight structures.

Conclusion

This study used analytical and deductive methodologies. The analytical approach involved conducting a comparative analysis of six case studies on lightweight structures. These structures were optimized using a specific topology optimization method at different stages. The analysis considered such factors as the structural type (continuum or discrete), form-finding techniques, the specific topology optimization method employed (ranging from SIMP to BESO), the materials used, the software utilized, the fabrication techniques employed, and the overall workflow for designing and fabricating each case study. The deductive approach was used to develop a framework for applying topology optimization in lightweight structures, as demonstrated by this analytical comparison. This framework consists of two fundamental processes, namely the form-finding process and the fabrication process (Fig. 15). Additionally, it is crucial to thoroughly analyze and comprehensively examine every step involved in each individual procedure. Next, the above-mentioned framework was employed to conduct a case study on the pentagonal Roman vault and create an optimal structure in terms of topology.

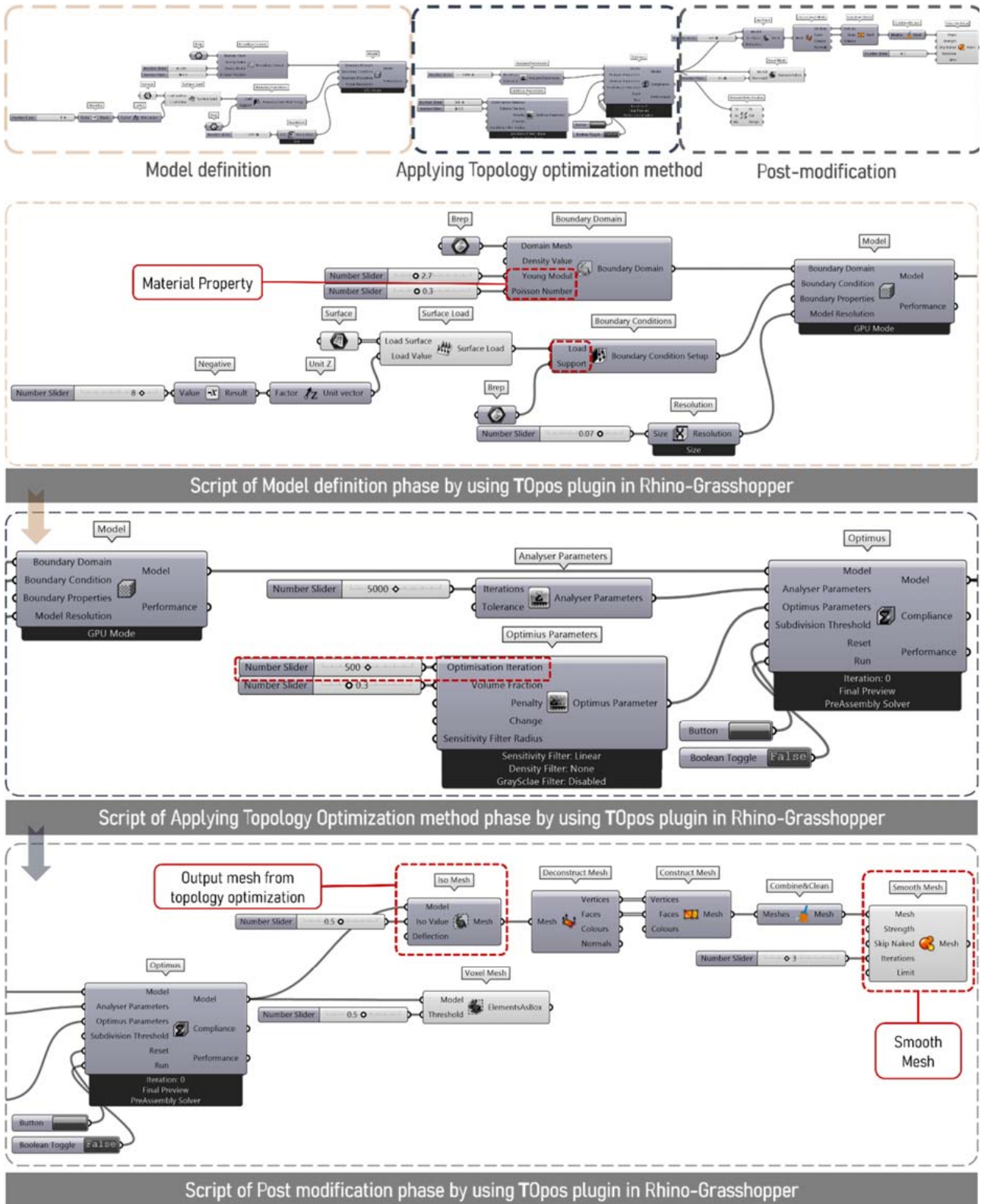


Fig. 11. Overall script for the form-finding process using the tOpos plugin in Rhino-Grasshopper (created by the authors)

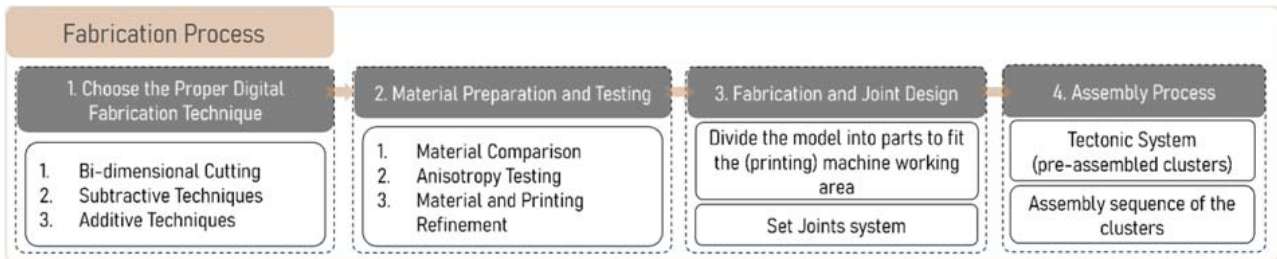


Fig. 12. Workflow of the fabrication process (created by the authors)



Fig. 13. Model printing process using a small-scale desktop 3D printer

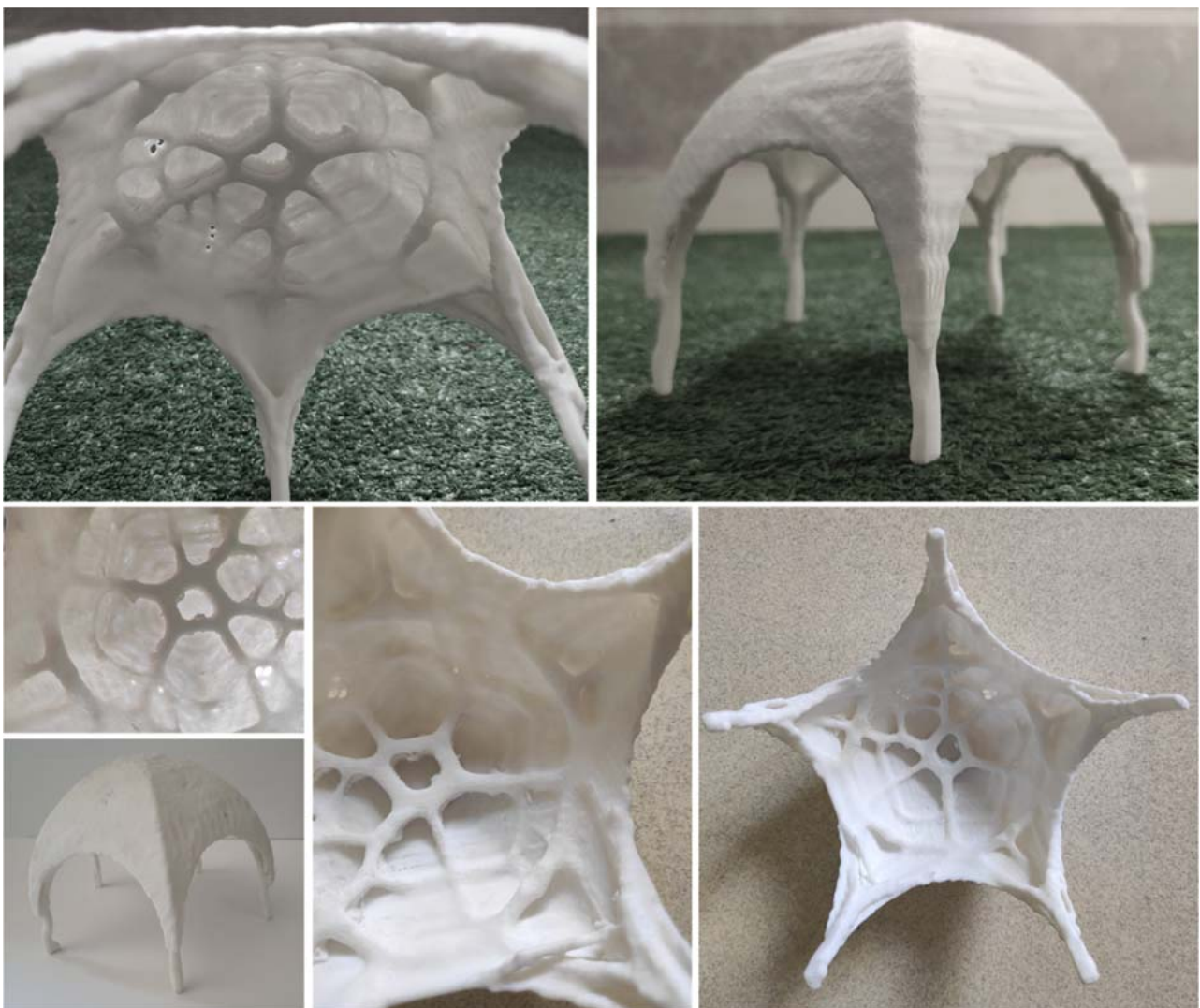


Fig. 14. Final printed optimized model

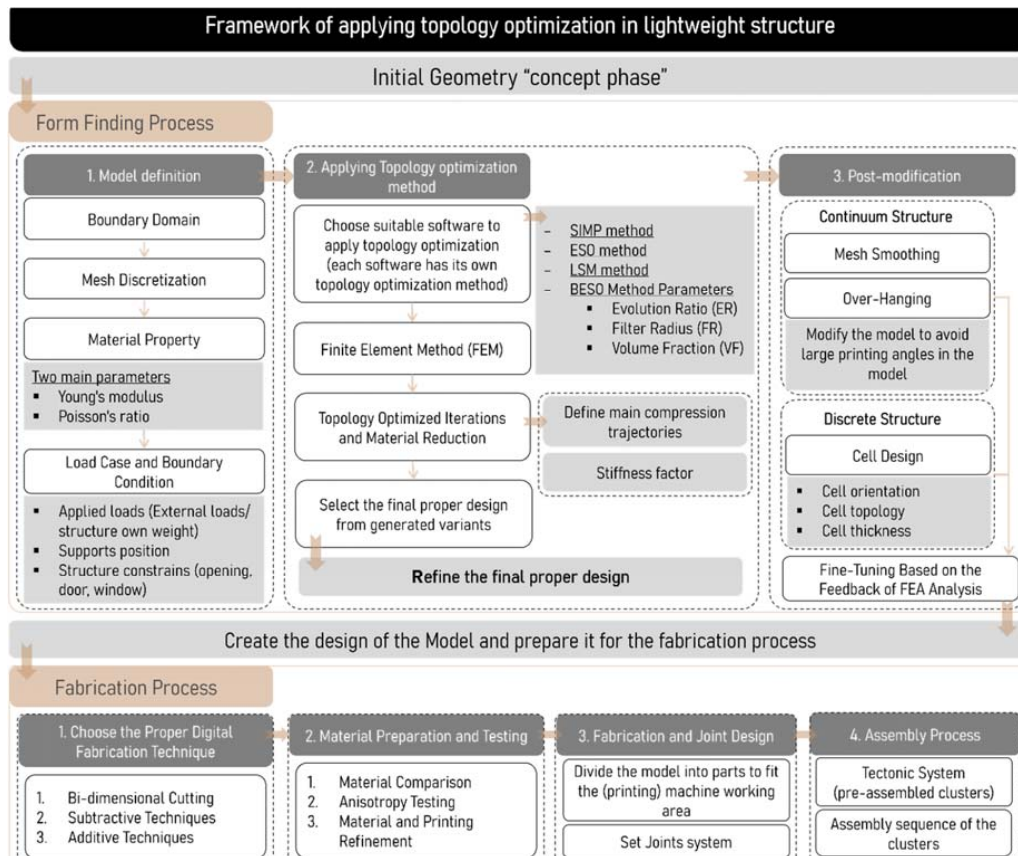


Fig. 15. Framework for applying topology optimization in lightweight structures (created by the authors)

References

- architizer.com (2023). *Mortuary Chapel for the Soriano Manzanet family*. [online] Available at: <https://architizer.com/projects/mortuary-chapel-for-the-soriano-manzanet-family-1/> [Date accessed September 25, 2023].
- Bao, D. W., Yan, X., Snooks, R., and Xie, Y. M. (2019). Design and construction of an innovative pavilion using topological optimization and robotic fabrication. In: *IASS Symposium 2019 - 60th Anniversary Symposium of the International Association for Shell and Spatial Structures; Structural Membranes 2019 - 9th International Conference on Textile Composites and Inflatable Structures, FORM and FORCE*, October 7–10, 2019, Barcelona, Spain, pp. 485–492.
- Bao, D. W., Yan, X., Snooks, R., and Xie, Y. M. (2020). Bioinspired generative architectural design form-finding and advanced robotic fabrication based on structural performance. In: Yuan, P. F., Xie, M., Leach, N., Yao, J., and Wang, X. (eds.). *Architectural Intelligence*. Singapore: Springer, pp. 147–170. DOI: 10.1007/978-981-15-6568-7_10.
- Bao, D. W., Yan, X., and Xie, Y. M. (2022). Fabricating topologically optimized tree-like pavilions using large-scale robotic 3D printing techniques. *Journal of the International Association for Shell and Spatial Structures*, Vol. 63, No. 2, pp. 122–131. DOI: 10.20898/j.iaass.2022.009.
- Bhooshan, S. (2017). Parametric design thinking: A case-study of practice-embedded architectural research. *Design Studies*, Vol. 52, pp. 115–143. DOI: 10.1016/j.destud.2017.05.003.
- Chen, Z., Zhang, L., and Yuan, P. F. (2019). Innovative design approach to optimized performance on large-scale robotic 3D-printed spatial structure. In: *Intelligent & Informed, Proceedings of the 24th International Conference of the Association for Computer-Aided Architectural Design Research in Asia (CAADRRIA) 2019*, Vol. 2. Hong Kong: Association for Computer-Aided Architectural Design Research in Asia (CAADRRIA), pp. 451–460.
- Dahy, H., Peters, J., and Baszynski, P. (2020). Biocomposites from annually renewable resources displaying vision of future sustainable architecture: design and fabrication of two 1:1 demonstrators. In: Burry, J., Sabin, J., Sheil, B., and Skavara, M. (eds.). *Fabricate 2020: Making Resilient Architecture*. London: UCL Press, pp. 66–73. DOI: 10.2307/j.ctv13xpsvw.13.
- Javadi Moghaddam, J., Momeni, D., and Zarei, G. (2023). Application of topology optimization method for the gothic greenhouse design. *World Journal of Engineering*, Vol. 20, Issue 3, pp. 496–509. DOI: 10.1108/WJE-03-2021-0191.
- Liu, K., Bai, Y., Yao, S., and Luan, S. (2022). Topology optimization of shell-infill structures for natural frequencies. *Engineering Computations*, Vol. 39, No. 8, pp. 3083–3107. DOI: 10.1108/EC-03-2022-0135.

- Liu, Y., Li, Z., Wei, P., and Chen, S. (2019). Generating support structures for additive manufacturing with continuum topology optimization methods. *Rapid Prototyping Journal*, Vol. 25, No. 2, pp. 232–246. DOI: 10.1108/RPJ-10-2017-0213.
- Louth, H., Reeves, D., Bhooshan, S., Schumacher, P., and Koren, B. (2017). A prefabricated dining pavilion: using structural skeletons, developable offset meshes and kerf-cut bent sheet materials. In: Menges, A., Sheil, B., Glynn, R., and Skavara, M. (eds.). *Fabricate 2017*. London: UCL Press, pp. 58–67. DOI: 10.2307/j.ctt1n7qkg7.12.
- Ma, J., Li, Z., Zhao, Z.-L., and Xie, Y. M. (2021). Creating novel furniture through topology optimization and advanced manufacturing. *Rapid Prototyping Journal*, Vol. 27, No. 9, pp. 1749–1758. DOI: 10.1108/RPJ-03-2021-0047.
- Martins, V. C., Cutajar, S., van der Hoven, C., Baszyński, P., and Dahy, H. (2020). FlexFlax stool: Validation of moldless fabrication of complex spatial forms of natural fiber-reinforced polymer (NFRP) structures through an integrative approach of tailored fiber placement and coreless filament winding techniques. *Applied Sciences*, Vol. 10, Issue 9, 3278. DOI: 10.3390/app10093278.
- Naboni, R., Breseghello, L., and Kunic, A. (2019). Multi-scale design and fabrication of the Trabeculae Pavilion. *Additive Manufacturing*, Vol. 27, pp. 305–317. DOI: 10.1016/j.addma.2019.03.005.
- Rihaczek, G., Klammer, M., Başnak, O., Petrš, J., Grisin, B., Dahy, H., Carosella, S., and Middendorf, P. (2020). Curved foldable tailored fiber reinforcements for moldless customized bio-composite structures. Proof of concept: biomimetic NFRP stools. *Polymers*, Vol. 12, Issue 9, 2000. DOI: 10.3390/polym12092000.
- Sigmund, O. and Maute, K. (2013). Topology optimization approaches: A comparative review. *Structural and Multidisciplinary Optimization*, Vol. 48, Issue 6, pp. 1031–1055. DOI: 10.1007/s00158-013-0978-6.
- Tedeschi, A. (2014). *AAD_algorithms-aided design: parametric strategies using Grasshopper*. Brienza: Le Penseur, 496 p.
- Woo, S. J. (2020). *An architectural implementation of topology optimization guided discrete structures with customized geometric constraints*. MSc Thesis in Architecture.
- Xie, Y. M. (2022). Generalized topology optimization for architectural design. *Architectural Intelligence*, Vol. 1, Issue 1, 2. DOI: 10.1007/s44223-022-00003-y.
- Yıldırım, E. (2022). Topology optimization in architecture practices. In: Biçer, Ö. P. and Gürani, F. Y. (eds.). *Research & Reviews in Architecture, Planning and Design*. Ankara: Gece, pp. 117–137.

ПРИНЦИПИАЛЬНО НОВАЯ СХЕМА ПРИМЕНЕНИЯ ТОПОЛОГИЧЕСКОЙ ОПТИМИЗАЦИИ В ОБЛЕГЧЕННЫХ КОНСТРУКЦИЯХ

Амани Санад Фуад, Мохамед Эззельдин, Айман Ассем*

Университет Айн-Шамс, Каир, Египет

*E-mail: ayman.assem@eng.asu.edu.eg

Аннотация

Введение: топологическая оптимизация широко используется в инженерных разработках и проектировании строительных конструкций. В области архитектуры, особенно в контексте облегченных конструкций, для полноценного использования этого метода необходимы серьезные навыки в программировании. **Цель исследования** — сформировать базовую схему, способствующую беспрепятственному применению топологической оптимизации при проектировании архитекторами облегченных конструкций. **Методы:** в данной работе для анализа шести примеров применения топологической оптимизации в различных облегченных конструкциях использовался дедуктивный метод. Анализ проводился на основе заранее определенного набора критериев. Кроме того, дедуктивный метод использовался для формирования схемы реализации топологической оптимизации при проектировании облегченных конструкций. Данная схема была использована для создания оптимизированной облегченной конструкции (пентагональный цилиндрический свод). **Выводы:** анализ примеров проводился с учетом двух процессов — процесса поиска формы и процесса изготовления. Исследование было направлено на определение методологической основы, задействованной в процессе проектирования и изготовления по каждому из примеров. Основопологающая схема была разработана на основе аналитического сравнения шести примеров. Данная схема позволяет создавать оптимизированные облегченные конструкции. **Новизна:** в данном исследовании представлены значимые результаты в области топологической оптимизации и ее использования в облегченных конструкциях, открывающие широкие возможности для архитекторов, стремящихся к созданию эстетически привлекательных и оригинальных архитектурных форм, в которых приоритетом является высокая жесткость и небольшой вес.

Ключевые слова: облегченные конструкции, топологическая оптимизация, аддитивные технологии.

Building Information Modeling

DOI: 10.23968/2500-0055-2024-9-3-15-26

BIM IMPLEMENTATION FOR HERITAGE RENOVATION THROUGHOUT PROJECT LIFECYCLE: CURRENT USE, BENEFITS, AND BARRIERS

Bani Feriel Brahmi*, Souad Sassi-Boudemagh

AVMF laboratory, University of Constantine 3 Salah Boubnider, Constantine, Algeria

*Corresponding author's email: feriel.brahmi@univ-constantine3.dz

Abstract

Introduction: Building Information Modeling (BIM) has garnered significant attention due to advancements in sophisticated technologies and methods. However, a comprehensive review of the existing literature indicates a lack of research exploring the application of BIM in managing the entire intervention design and renovation processes from a broader system perspective. The **purpose of the study** was to fill this gap by identifying and evaluating the current utilization, benefits, and barriers associated with implementing BIM in the lifecycle of renovation projects. The study **methodology** is based on conducting 31 structured interviews with experienced professionals who have employed BIM in their project deliveries. The **results** reveal that the primary benefits of BIM adoption, in descending order of importance, pertain to improved collective understanding of design intent, lower risk and better predictability of outcomes, better-designed and performing buildings, more accurate project documentation, and increased accuracy of the cost estimate. However, there are several prominent barriers: project budget, complexity of modeling historic structures, cost to hire BIM professionals, and the lack of BIM knowledge. The findings will advance BIM adoption for heritage renovation and enable project stakeholders to focus on realizing the benefits and potential uses of lifecycle BIM, while also addressing the critical challenges discussed in this study.

Keywords: BIM implementation; heritage renovation; BIM benefits; BIM barriers.

Introduction

The renovation of heritage buildings holds great potential for preserving a sense of identity and continuity for future generations in a rapidly changing world. Today, the renovation of heritage buildings serves as a revitalization avenue to promote sustainability and safeguard the buildings' significance and values (Fouseki and Cassar, 2014). Moreover, it brings about economic growth, as well as social, cultural, and environmental benefits to urban communities (Tweed and Sutherland, 2007).

Undertaking renovation projects involves managing significant complexity, which includes handling multiple stakeholders and addressing various renovation objectives and criteria, especially when the building remains in use (Buser and Carlsson, 2016; Kamari et al., 2019a). There is a need to explore and select among a large number of renovation alternatives and approaches available in the market, considering the attitudes and behavior of the building occupants (Kamari et al., 2019b; Lidelöw et al., 2019). Complexity increases during the early design phases, and significant changes may occur due to the unavailability of original structural information or unforeseen construction conditions identified late, resulting in project time and cost overruns (Roy and Kalidindi, 2017).

Information technology (IT) is widely discussed in the context of the emergence of large, ambitious, and complex projects in the architecture, engineering, construction, and operations (AECO) industry. This is driven by new sustainability requirements that necessitate regular and efficient information exchange among project participants and stakeholders throughout the project lifecycle (Oesterreich and Teuteberg, 2016). Currently, IT has become an increasingly vital tool across all industries, uncovering untapped value potential. The AECO sector is also experiencing transformation with the advent of the Fourth Industrial Revolution, known as Industry 4.0 (Lasi et al., 2014). The digitization and automation of construction, often referred to as Construction 4.0, are leading to changes in product and supply chain management (Dallasega et al., 2018). It is a major enabler of productivity improvements, along with sophisticated and integrated design and construction, through the adoption of innovative and disruptive technologies, including BIM (Oesterreich and Teuteberg, 2016).

BIM has emerged as a catalyst for paradigm change and has become an industry standard in the AECO sector by automating and manipulating data at different project lifecycle stages (Farnsworth et al., 2015; Kelly and Ilozor, 2019). In the context

of heritage renovation, BIM has garnered significant interest for its technological advancements and methodological developments, such as 3D laser scanning and photogrammetry. As a digital delivery method, BIM revolutionizes the information management of the renovation process by storing interrelated semantic information, which facilitates the dissemination of intangible values of a building throughout its lifecycle (Angelini et al., 2017).

While existing literature has extensively explored the potential benefits of BIM in digital building documentation (Pocobelli et al., 2018), there is a notable lack of research focusing on the use of BIM for managing entire intervention design and renovation processes, including the generation and evaluation of various design alternatives. Furthermore, most studies have relied on single-case analyses, with few adopting a broader systemic perspective. Therefore, this study aims to fill this gap by identifying and assessing the current utilization of BIM in renovation projects' lifecycle, examining the benefits gained, and identifying the barriers encountered.

Background

The BIM adoption process may differ between new and existing buildings due to variations in information availability, the quality of building information, and functionality requirements. The majority of research has focused on exploring the potential benefits of employing BIM for digital building documentation (Pocobelli et al., 2018). BIM generates a digital model for the preservation process because of its ability to store interrelated semantic information, promoting the dissemination of a building's intangible values during its lifecycle (Angelini et al., 2017). BIM offers efficient and accurate remote presentation, analysis, and documentation of the structure, surpassing previous survey techniques (Gigliarelli et al., 2017). However, the effectiveness of BIM is subject to broader discussions due to the challenges related to the high effort required for modeling/converting captured building data into semantic BIM objects (López et al., 2018). The variety and complexity of heritage building components may not be represented in current typical BIM software libraries, and also depend on the level of detail required to perform engineering and design analyses (López et al., 2018; Pocobelli et al., 2018). Brahmi et al. (2022) suggested integrating other emerging technologies within BIM and seeking innovative solutions to overcome this issue. They also recommended developing, upgrading, and adjusting BIM simulation software to accurately represent the conditions of heritage buildings and enable accurate environmental simulations within BIM modeling (Brahmi et al., 2022).

Simeone et al. (2014) investigated the potential impact of BIM in heritage renovations to

improve specialists' collaboration and knowledge management. The authors concluded that BIM models, like those used in new construction projects, ensure the availability, accessibility, consistency, and coordination of all knowledge related to a historical artifact and shared by different actors involved in investigation/conservation processes. This promotes decision-making on the development of relevant interventions (Simeone et al., 2014). However, only a few research studies have investigated the generation and evaluation of various design alternatives in heritage renovation using BIM.

Heritage buildings have a very high energy demand, as well as a very low indoor climate standard (Tomšič et al., 2017). For example, 35 % of buildings in the European Union are more than 50 years old, and nearly 75 % of the building stock (including heritage buildings) are energy inefficient (European Commission, 2019). The same statistics demonstrate that renovating existing buildings can lead to significant energy savings, as it could reduce total EU energy consumption by 5–6 % and CO₂ emissions by around 5 %. Conversely, only about 1 % of the building stock is renovated each year. In this regard, the design team must address the increasing energy demand and indoor environmental requirements while also considering architectural aspects and qualities in developing appropriate renovation scenarios (design options).

Brahmi et al. (2022) revealed that BIM enables design teams to conduct faster, complex analyses and rapid assessments of energy simulations through BIM coordination with energy models, to produce a full virtual construction model. In their research, Žurić et al. (2022) focused on the "historical value" when integrating HBIM into GBC historic building certification. The implementation process focuses on interoperability and data preservation, using the open standard (IFC). However, there is limited research effort to integrate Life Cycle Assessment (LCA) with BIM and manage the environmental performance of renovation projects, along with the lack of a "cradle-to-grave" comprehensive BIM-based environmental sustainability simulation tool (Wong and Zhou, 2015). Similarly, current cloud computing technology and Big Data management are not sufficiently addressed within the green BIM tool (Wong and Zhou, 2015).

Recent studies propose methodologies for linking Heritage BIM with various technologies and digital simulations, such as Building Performance Simulation (BPS) and computational design (Gigliarelli et al., 2017). However, these studies also highlight the lack of open-source platforms for Heritage BIM, limited interoperability between different software environments (such as gbXML files or IFC files) (Cheng et al., 2015; Gigliarelli et al., 2017), and the need for integration with facilities management

technologies (Kassem et al., 2015). Furthermore, only a few published prototypes with limited usage demonstrate markedly different BIM requirements in these projects (Angelini et al., 2017; Edwards, 2017). Despite the rapid developments and dissemination of standards, further research is necessary to automate processes and adapt BIM to the specific requirements of existing buildings (Volk et al., 2014).

Methods

To achieve the research objectives, a series of structured online interviews were conducted between January 2, 2022, and March 15, 2022. A total of 31 experienced professionals involved in heritage renovation projects that utilized BIM participated in the interviews. The inclusion criteria ensured that all interviewees had more than 10 years of professional experience and possessed the necessary knowledge of BIM within the heritage sector. The majority of interviewees, primarily from Canada and the United States, had diverse organizational backgrounds. This included architectural firms (54.84 %), followed by construction firms (16.13 %), engineering firms (12.9 %), academic staff (6.45 %), and three respondents from owners, facility managers, and construction management. The sample size of 31 interviewees, while not exhaustive, was chosen to provide a variety of perspectives within the constraints of the study. The selection was made purposefully to capture a representative sample and effectively address the research questions, reflecting the actual perceptions, complexities, and widespread use of BIM practices in heritage renovations.

Within their respective organizations, the respondents reported having such roles as BIM specialists (32.26 %), historic preservation consultants (25.81 %), project managers (22.58 %), and directors (19.35 %). Additionally, 67.74 % of the participants stated that they were members of various local or international organizations committed to heritage preservation.

The interview questionnaire consisted of 20 structured questions divided into two major parts: I) Current use and benefits of BIM in heritage renovation throughout the project lifecycle, and II) Barriers to using BIM in heritage renovation throughout the project lifecycle. The interview questions were initially based on a study conducted by Feng et al. (2014) and were later modified and adapted to specifically investigate BIM implementation in the context of heritage renovation. The interviewees were asked to select and rank the identified benefits and barriers of BIM implementation using a five-point Likert-type scale. The responses were then used to measure the significance of each item using the statistical method of mean score (M).

Results and Discussion

This section presents the findings obtained from the interviews conducted during the study

and provides a comprehensive discussion of the results. The results are organized into two main parts: I) Current use and benefits of BIM in heritage renovation throughout the project lifecycle, and II) Barriers to BIM implementation in heritage renovation throughout the project lifecycle.

1. Current use and benefits of BIM in heritage renovation throughout the project lifecycle

The results of the interviews indicate that a significant majority of the respondents (75 %) have recent experience with BIM, specifically within the past five years, as BIM was utilized in the completion of their renovation projects. This suggests that the respondents possess relevant and up-to-date knowledge and expertise, making their responses representative and reliable.

As shown in Fig. 1, Autodesk Revit is the most commonly used BIM software in heritage renovation, with up to two-thirds of respondents (21 responses) reporting its use in their projects. This finding aligns with previous research in the literature, supporting the prevalence of Autodesk Revit in the field of heritage renovation (Logothetis et al., 2015; López et al., 2018). The popularity of Autodesk Revit can be attributed to its robust capabilities and widespread adoption within the industry. The respondents mentioned other BIM software platforms in addition to Autodesk Revit. Navisworks™ was mentioned by 11 respondents, indicating its usage for tasks such as clash detection and project coordination. Graphisoft ArchiCAD was mentioned by 5 respondents, followed by Tekla Structures with 2 mentions, and Bentley Systems Architecture and VICO Constructor with 1 mention each. These software platforms provide specialized features and functionalities that cater to specific project requirements or user preferences.

Fig. 2 highlights the leadership role of architects in the BIM coordination process for completed renovation projects. In the majority of cases (58 %), architects took the lead in BIM coordination. This finding aligns with the common practice in which architects assume the role of lead designers in construction projects, overseeing the overall design and coordination of various disciplines. The architect's involvement in BIM coordination reflects their crucial role in managing collaborative efforts and ensuring effective communication among project stakeholders.

During the interviews, the respondents were asked to indicate the BIM applications utilized in their renovation projects from a list of 15 identified applications (Fig. 3). Subsequently, they were asked to rank the benefits of these BIM applications on a 5-point Likert scale (1 — not beneficial at all, 2 — slightly beneficial, 3 — moderately beneficial, 4 — very beneficial, and 5 — extremely beneficial) (Fig. 4).

As anticipated and consistent with previous research findings (Gigliarelli et al., 2017;

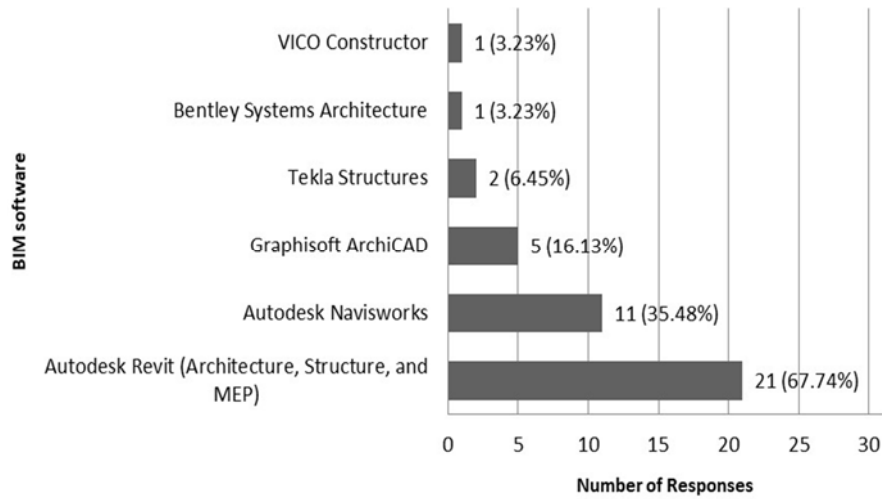


Fig. 1. BIM software packages used in heritage renovation projects

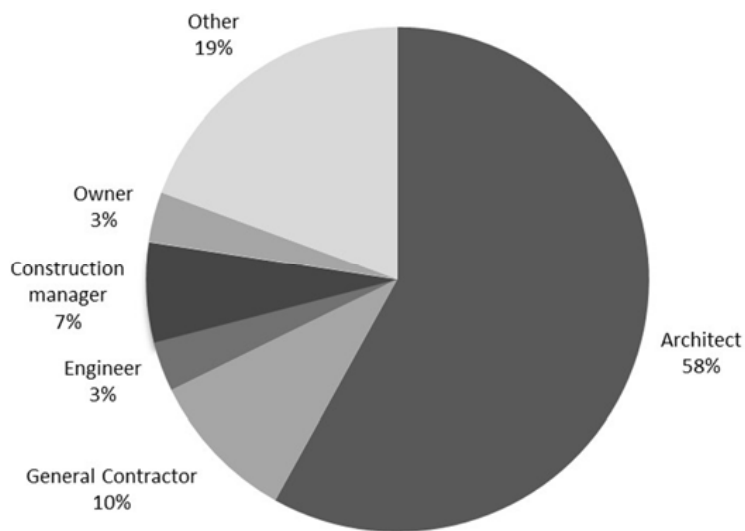


Fig. 2. BIM leadership

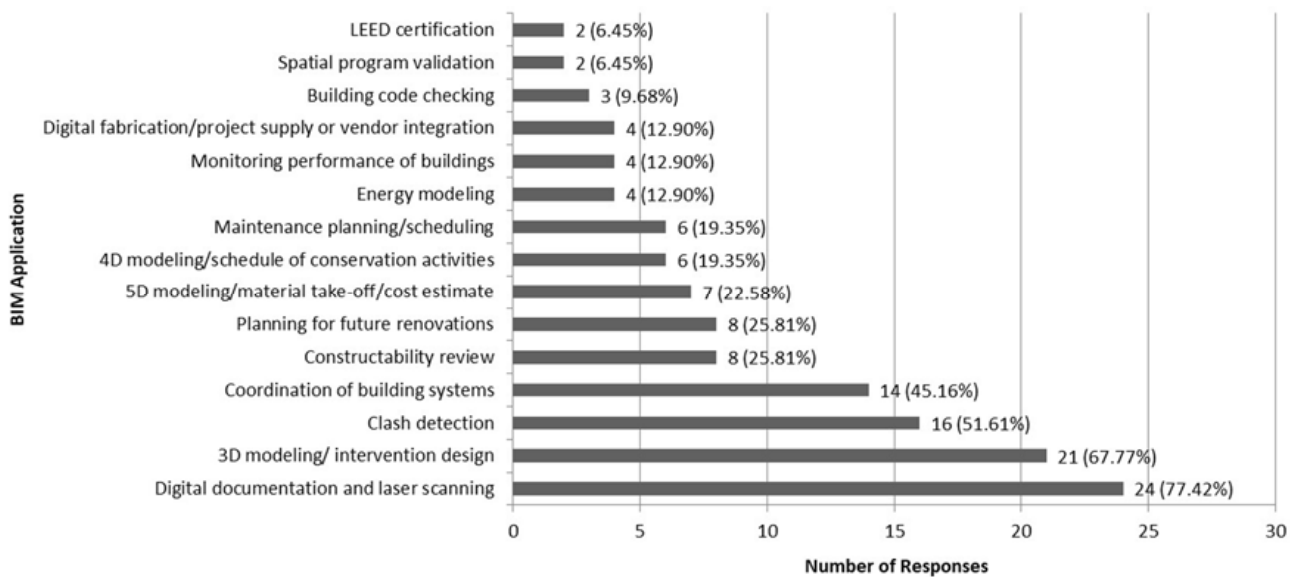


Fig. 3. Extent of current usage of various BIM applications in heritage renovation projects

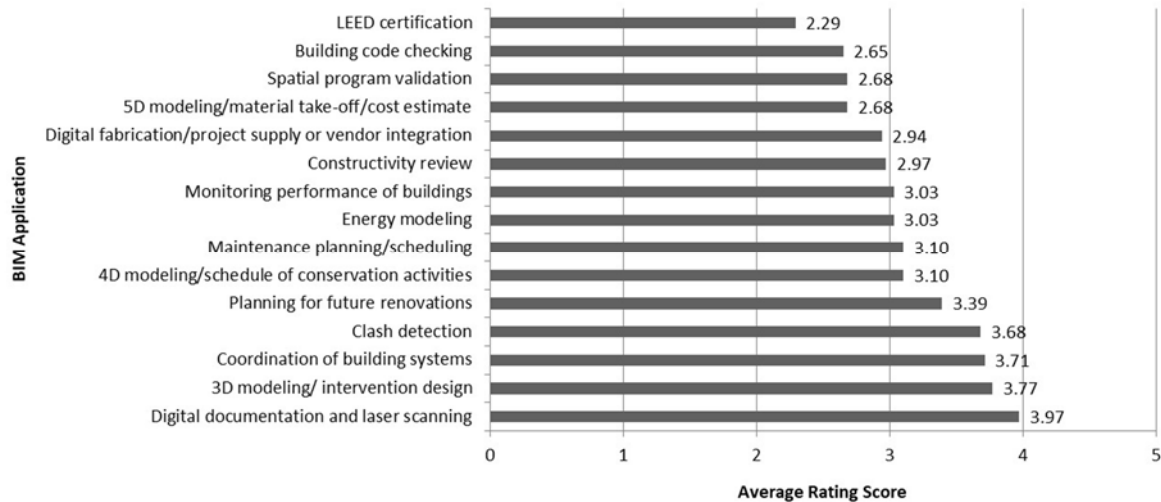


Fig. 4. Benefits of using BIM applications in heritage renovation projects

Pocobelli et al., 2018), the most commonly used BIM application in renovation projects is digital documentation and laser scanning, with 24 respondents reporting its use. Furthermore, this application is considered the most beneficial for renovation projects, with an average score of 3.97. These findings are supported by several studies (Angelini et al., 2017; Gigliarelli et al., 2017; López et al., 2018; Pocobelli et al., 2018).

Surprisingly, the results indicate significant developments and changes in BIM practices in recent years, which vary from project to project. The use of BIM has expanded to encompass more diverse and multifaceted applications, notably 3D modeling and intervention design (21 responses), clash detection (16 responses), and building systems coordination (14 responses). These applications were highly ranked for their perceived benefits in renovation projects, following digital documentation and laser scanning. The respondents recognized the value of 3D modeling and intervention design (average score: 3.77), as it allows for enhanced visualization and understanding of design intent. Building systems coordination (average score: 3.77) emerged as another crucial aspect, facilitating the effective integration and collaboration between different subsystems within the project. Clash detection (average score: 3.68), on the other hand, helps identify and resolve conflicts or clashes between various building elements or systems, enhancing efficiency and reducing rework.

The findings emphasize BIM's ability to foster teamwork and support collaborative, multilevel, and iterative processes. It provides a platform for evaluating alternative design options and value engineering, enabling stakeholders to explore different possibilities and negotiate connections and interfaces between subsystems. This collaborative approach can lead to optimized designs, improved

performance, and enhanced decision-making throughout the project lifecycle.

The results highlight the growing recognition and utilization of BIM's capabilities beyond traditional applications, such as documentation and scanning. The expanding use of BIM in areas such as 3D modeling, clash detection, and building systems coordination highlights its potential to enhance efficiency, coordination, and collaboration in renovation projects. This finding aligns with the idea that BIM supports a more integrated and collaborative approach to design and construction, enabling stakeholders to leverage its benefits and overcome project complexities (Migilinskas et al., 2013).

In contrast, certain BIM applications remain largely unexplored in the context of heritage renovation, including energy modeling (4 responses), building code checking (3 responses), spatial program validation (2 responses), and LEED certification (2 responses). Additionally, the last BIM applications, along with 5D modeling/cost estimation, ranked as the least beneficial, likely due to their limited usage in renovations. Pocobelli et al. (2018) argued for the inclusion of tools such as rule-based code checking within BIM platforms. This inclusion would facilitate coordination and standardization of policies and controls related to environmental/energy performance and historic preservation codes, as well as the automation of the Leadership in Energy and Environmental Design (LEED) process for green building certification (Pocobelli et al., 2018).

Overall, the findings indicate that there is room for further exploration and utilization of specific BIM applications in the context of heritage renovation. By incorporating them, stakeholders in heritage renovation projects can potentially enhance project outcomes, improve environmental performance, and ensure compliance with relevant regulations and certifications.

The results of the interview questionnaire, which assessed the rating of a list of 21 identified benefits achieved through BIM utilization in renovation projects, are presented in Fig. 5. The mean (M) values range from the lowest mean score of M = 2.58 for “Individual participant productivity” to the highest mean value of M = 3.90 for “Improved collective understanding of design intent”. To determine the significance of each factor, the study adopted a scale interval grading similar to the approach utilized by Olawumi et al. (2018). The grading scale is as follows: “not important” (M < 1.50), “somewhat important” (1.51 ≤ M ≤ 2.50), “important” (2.51 ≤ M ≤ 3.50), “very important” (3.51 ≤ M ≤ 4.50), and “extremely important” (M ≥ 4.51). This scale helps categorize the level of importance attributed to each benefit (Fig. 5).

Heritage renovation is a complex and sensitive approach, characterized by a high level of risk and uncertainty (Roy and Kalidindi, 2017). The results of this study demonstrate that shifting to BIM offers an effective approach to address this challenge. The five most significant benefits of BIM implementation are: improved collective understanding of design intent, lower risk and better predictability of outcomes, better-designed and performing buildings, more accurate project documentation, and increased accuracy of the cost estimate (with mean values of 3.90, 3.71, 3.61, 3.58, and 3.52, respectively). It is important to note that none of the identified benefits scored higher than 4.50, nor 2.50 or lower (Fig. 5). Therefore, these 21 benefits can be categorized as significant advantages that demonstrate the usefulness of BIM in improving the effectiveness and efficiency of heritage renovation projects, while also

highlighting opportunities to further maximize BIM benefits in such projects.

Fig. 6 illustrates the contribution of BIM to improved performance across different project phases. The reviewees reported that BIM is most likely to contribute to improved performance during the construction document phase (20 responses) and the design development phase (19 responses). In contrast, the use of BIM is perceived to have a lesser contribution during the post-construction operation phase (Fig. 6), which aligns with existing literature indicating that BIM adoption in this phase is not yet well-established (Kassem et al., 2015).

El-adaway et al. (2017) suggested that improving the performance of the construction industry should start with the contract and organizational aspects. In line with this perspective, the respondents in this study were asked to rate the frequency and benefits achieved through the use of different project delivery methods within BIM, using a five-point Likert-type scale (Fig. 7). The results indicate that BIM is most often used in the design-bid-build delivery method, which is likely the most widely employed approach. The construction management and design-build methods follow it. Nevertheless, the respondents perceived that BIM implementation is highly beneficial for projects delivered using the construction management method (with an average score of M = 3.55), more so than for design-bid-build (M = 3.48). This perception is likely due to the collaborative requirements between parties in the construction management method, as this approach typically involves more collaboration and coordination among the project stakeholders. The shift towards BIM in construction necessitates

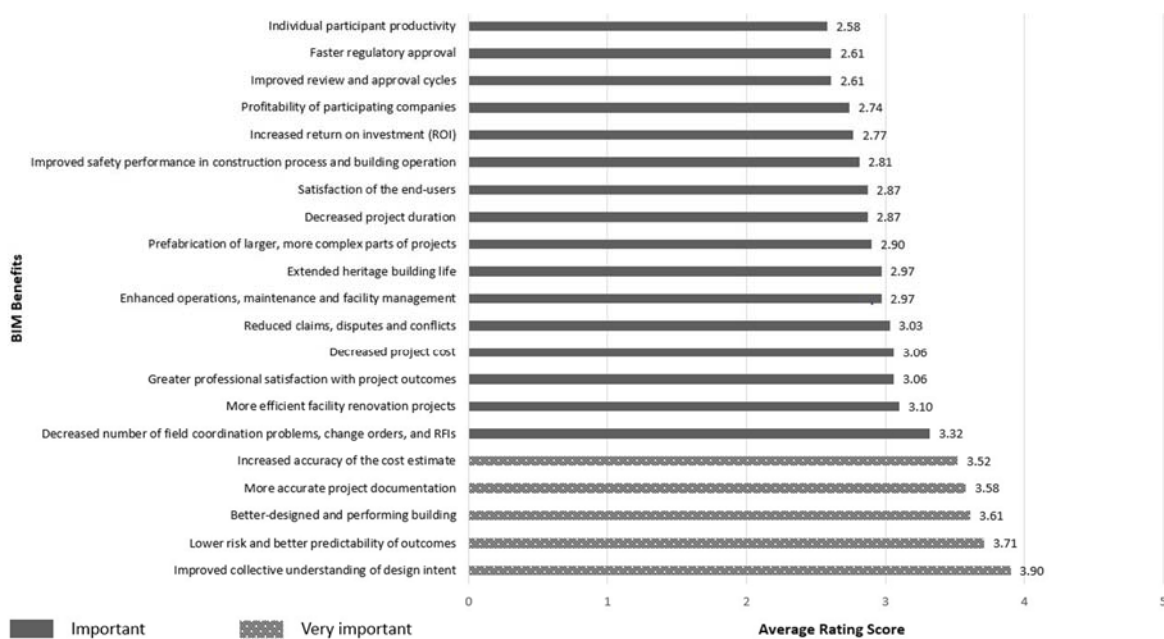


Fig. 5. Summary of BIM benefits

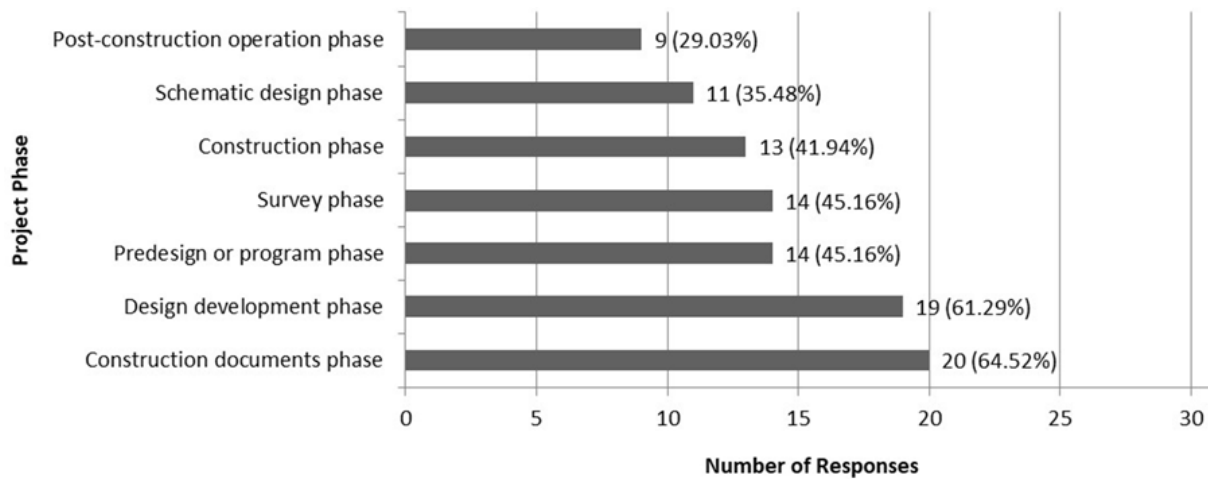


Fig. 6. BIM's contribution to improved performance in different project phases

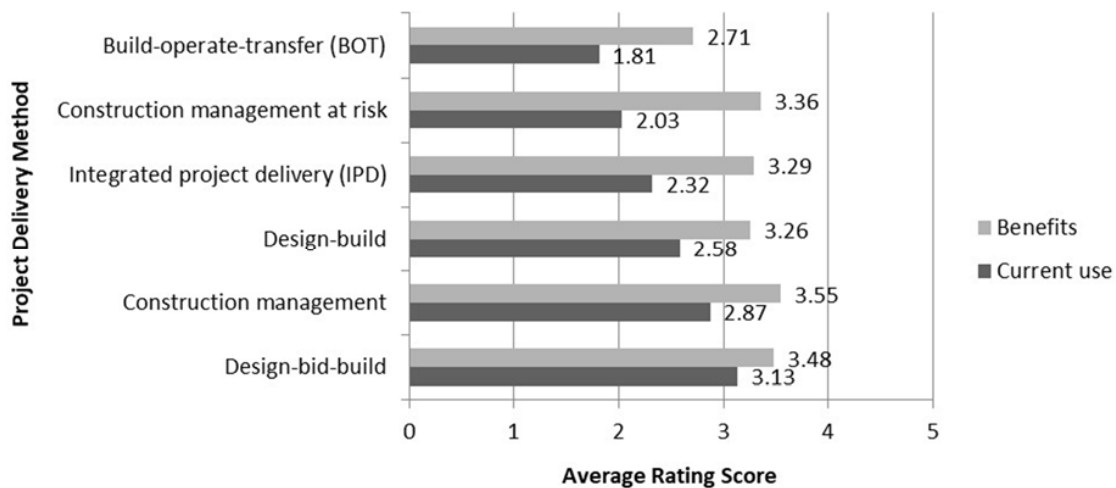


Fig. 7. Current use and benefits of BIM within different project delivery methods

a change in contractual arrangements, as the fragmentation of traditional approaches and fights for individual benefits contradict the collaborative atmosphere required for successful BIM implementation (Migilinskas et al., 2013).

2. Barriers to BIM implementation in heritage renovation throughout the project lifecycle

To identify and prioritize the barriers that hinder BIM implementation in renovation projects, the respondents were asked to rank a list of 17 identified barriers using a five-point Likert-type scale (Fig. 8). The same scale interval grading utilized in the previous section (for BIM benefits) was applied to determine the significance of each barrier: “not important” ($M < 1.50$), “somewhat important” ($1.51 \leq M \leq 2.50$), “important” ($2.51 \leq M \leq 3.50$), “very important” ($3.51 \leq M \leq 4.50$), and “extremely important” ($M \geq 4.51$).

The mean values (M) for the barriers range from the lowest mean score of $M = 2.74$ for “Project is too complex” to the highest mean value of $M = 3.71$ for “Project budget”. Similar to the benefits analysis,

the scale interval grading was used to determine the significance of each barrier. Notably, all 17 factors fall within the categories of “important” and “very important” barriers that require the attention and consideration of project stakeholders to ensure the full implementation of BIM in heritage renovation. The most significant barriers pertained to the project budget, complexity of modeling historic structures, cost of hiring BIM professionals, and lack of (H)BIM knowledge, with mean values of 3.71, 3.61, 3.58 and 3.55, respectively.

The respondents highlighted project budget and financial constraints as major barriers to BIM implementation. This suggests that the cost of incorporating BIM technologies and processes in heritage renovation projects may exceed the allocated budget or may not be adequately considered during project planning. As mentioned in the literature, the results highlight that the respondents recognize the complexity involved in modeling historic structures using BIM. Heritage buildings often possess unique architectural features, intricate designs, and

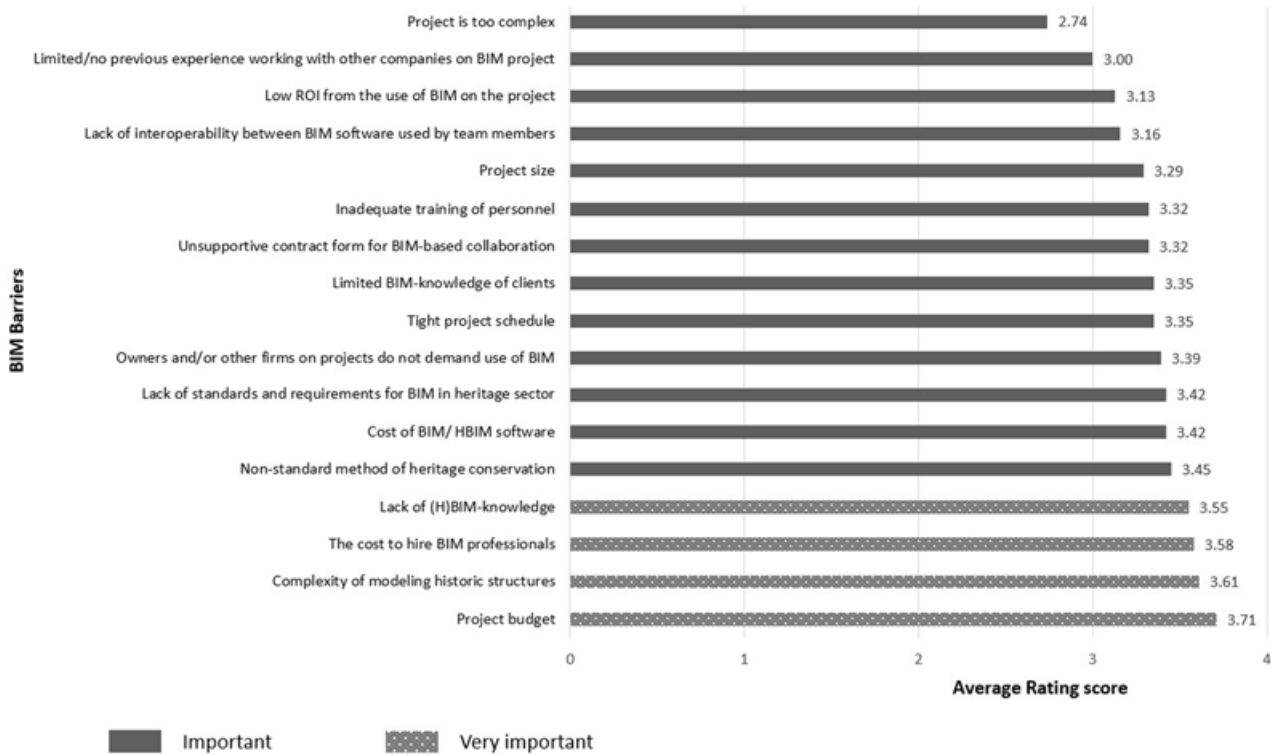


Fig. 8. Summary of BIM barriers in descending order of significance

unconventional construction techniques, which can pose challenges when developing accurate and detailed digital models. Furthermore, the respondents perceive a lack of knowledge and understanding of BIM and heritage-specific BIM (HBIM) as barriers to successful implementation. This implies that stakeholders involved in heritage renovation projects may not have sufficient knowledge of BIM processes, methodologies, or the specific considerations required for managing heritage projects.

Recommendations for future improvements

To overcome these barriers and maximize the potential of BIM in heritage renovation, the following practical recommendations and strategies are suggested:

- Mandate BIM adoption in contracts: Owners and developers of heritage projects should include clauses mandating the use of BIM in contracts. In this regard, almost all respondents (90 %) confirm the importance of property owners’ mandating of the use of BIM to encourage its implementation on heritage sites. Here, the client plays a complex role as a change agent, using their power and influence to drive change among project participants (Lindblad, 2019).
- Combining methodologies, techniques, and software: Explore the integration of different methodologies, techniques, and software to open up new possibilities for enhancing BIM applications to attain sustainability and high-performance outcomes. The advancement of digitalization in the construction industry, including the adoption of Industry 4.0 practices,

provides a foundation for benchmarking the effects of digital technologies.

- Financial support and incentives: Seek financial support from federal governments and encourage clients to provide incentives for interdisciplinary cooperation, especially for experts from construction companies. This could involve setting up venture capital funds to support the growth of innovative startups and facilitate their collaboration with developers and contractors in implementing BIM for heritage projects.
- Involvement of heritage governmental bodies: Involve heritage governmental bodies during the design phase to ensure that their expertise and perspectives are incorporated into the BIM implementation process.
- Education and training opportunities: Launching more education and training opportunities, especially for the heritage preservation community and project managers, to help them become digitally adept.
- Encourage academic research: Encourage further academic research on the subject of BIM in heritage renovation and support the publication of papers in this field to advance knowledge and understanding.
- Adapt organizational and business structures: Select organizational and business structures that align with the characteristics of sustainable renovation and are best suited to the capabilities and needs of project participants for the efficient implementation of heritage projects.

- Develop new contracts and legal frameworks: Create and develop new contracts and legal frameworks that foster collaboration and enable the full realization of benefits from BIM utilization.

By implementing these recommendations, stakeholders can overcome barriers and enhance the effective implementation of BIM in heritage renovation projects.

Conclusions

This research aims to identify and assess the current use, benefits gained, and barriers encountered in implementing BIM for heritage renovation. To achieve this objective, 31 structured online interviews were conducted with experienced professionals in the field. The study makes a new contribution by investigating BIM implementation throughout the entire lifecycle of heritage projects.

The results reveal that the primary benefits of BIM adoption, in descending order of importance, pertain to improved collective understanding of design intent, lower risk and better predictability of outcomes, better-designed and performing buildings, more accurate project documentation, and increased accuracy of the cost estimate. Conversely, the most significant barriers are project budget limitations, the complexity of modeling historic structures, the cost of hiring BIM professionals, and the lack of (H)BIM knowledge.

The results also indicate a significant and unexpected shift in BIM practices in recent years,

revealing varied usage patterns across different projects. The usage of BIM has expanded to encompass more multifaceted applications, such as clash detection and building system coordination. However, there is untapped potential for BIM use in areas such as energy modeling, LEED certification, building code checking, 5D modeling/cost estimation, and spatial program validation. These areas need to be explored to address multiple criteria, project complexity, and values. In doing so, experiences from new and existing buildings can serve as a benchmark for evaluating the effects of BIM in sustainable heritage renovation.

A significant limitation of this study is the data collection process, which relied on the willingness of participants. The sample size of interviews was limited, which may restrict the comprehensive investigation of BIM implementation regarding its complexity and widespread use. However, the findings contribute to advancing BIM adoption in heritage renovation and provide guidance to project stakeholders on maximizing the benefits of BIM throughout the project lifecycle while addressing critical challenges. Future research efforts could involve conducting quantitative studies with a larger pool of participants to explore and compare BIM experiences from different stakeholders' perspectives, in order to further validate and generalize the results.

References

- Angelini, M. G., Baiocchi, V., Costantino, D., and Garzia, F. (2017). *Scan to BIM for 3D reconstruction of the Papal Basilica of Saint Francis in Assisi in Italy*. [online] Available at: <https://www.sanfrancescoassisi.org/fondazione/ita/pdf/2017-Scan-to-BIM.pdf> [Date accessed January 13, 2022].
- Brahmi, B. F., Sassi Boudemagh, S., Kitouni, I., and Kamari, A. (2022). IPD and BIM-focussed methodology in renovation of heritage buildings. *Construction Management and Economics*, Vol. 40, Issue 3, pp. 186–206. DOI: 10.1080/01446193.2021.1933557.
- Buser, M. and Carlsson, V. (2016). What you see is not what you get: single-family house renovation and energy retrofit seen through the lens of sociomateriality. *Construction Management and Economics*, Vol. 35, Issue 5, pp. 276–287. DOI: 10.1080/01446193.2016.1250929.
- Cheng, H.M, Yang W.B, & Yen, Y.N. (2015). BIM applied in historical building documentation and refurbishing. *The International Archives of the Photogrammetry, Remote Sensing and Spatial Information Sciences*, XL-5/W7, 85–90.
- Dallasega, P., Rauch, E., and Linder, C. (2018). Industry 4.0 as an enabler of proximity for construction supply chains: A systematic literature review. *Computers in Industry*, Vol. 99, pp. 205–225. DOI: 10.1016/j.compind.2018.03.039.
- Edwards, J. (2017). It's BIM – but not as we know it! In: Arayici, Y., Counsell, J., Mahdjoubi, L., Nagy, G., Hawas, S., and Dweidar, K. (eds.) (2017). *Heritage building information modeling*. New York: Routledge, pp. 6–14.
- El-adaway, I., Abotaleb, I., and Eteifa, S. (2017). Framework for multiparty relational contracting. *Journal of Legal Affairs and Dispute Resolution in Engineering and Construction*, Vol. 9, Issue 3, 04517018-1–04517018-19. DOI: 10.1061/(ASCE)LA.1943-4170.0000238.
- European Commission. (2019). Energy performance of buildings directive. [online] Available at: https://ec.europa.eu/energy/topics/energy-efficiency/energy-efficient-buildings/energy-performance-buildings-directive_en [Date accessed December 09, 2020].
- Farnsworth, C. B., Beveridge, S., Miller, K. R., and Christofferson, J. P. (2015). Application, advantages, and methods associated with using BIM in commercial construction. *International Journal of Construction Education and Research*, Vol. 11, Issue 3, pp. 218–236. DOI: 10.1080/15578771.2013.865683.
- Feng, L. Olbina, S., and Issa, R. (2014). Implementation of Building Information Modeling (BIM) on K-12 educational facility projects in Florida. In: Sulbaran, T. (ed.). *50th ASC Annual International Conference Proceedings*. March 26–28, 2014, Virginia Tech, Virginia.
- Fouseki, K. and Cassar, M. (2014). Energy efficiency in heritage buildings — future challenges and research needs. *The Historic Environment: Policy & Practice*, Vol. 5, Issue 2, pp. 95–100. DOI: 10.1179/1756750514Z.00000000058.
- Gigliarelli, E., Calcerano, F., and Cessari, L. (2017). Heritage BIM, numerical simulation and decision support systems: an integrated approach for historical buildings retrofit. *Energy Procedia*, Vol. 133, pp. 135–144. DOI: 10.1016/j.egypro.2017.09.379.
- Kamari, A., Jensen, S. R., Corrao, R., and Kirkegaard, P. H. (2019a). A holistic multi-methodology for sustainable renovation. *International Journal of Strategic Property Management*, Vol. 23, No. 1, pp. 50–64. DOI: 10.3846/ijspm.2019.6375.
- Kamari, A., Schultz, C. P. L., and Kirkegaard, P. H. (2019b). Constraint-based renovation design support through the renovation domain model. *Automation in Construction*, Vol. 104, pp. 265–280. DOI: 10.1016/j.autcon.2019.04.023.
- Kassem, M., Kelly, G., Dawood, N., Serginson, M., and Lockley, S. (2015). BIM in facilities management applications: a case study of a large university complex. *Built Environment Project and Asset Management*, Vol. 5, No. 3, pp. 261–277. DOI: 10.1108/BEPAM-02-2014-0011.
- Kelly, D. and Ilozor, B. (2019). A quantitative study of the relationship between project performance and BIM use on commercial construction projects in the USA. *International Journal of Construction Education and Research*, Vol. 15, Issue 1, pp. 3–18. DOI: 10.1080/15578771.2016.1202355.
- Lasi, H., Kemper, H.-G., Fettke, P., Feld, T., and Hoffmann, M. (2014). Industry 4.0. *Business & Information Systems Engineering*, Vol. 6, Issue 4, pp. 239–242. DOI: 10.1007/s12599-014-0334-4.
- Lidelöw, S., Örn, T., Luciani, A., and Rizzo, A. (2019). Energy-efficiency measures for heritage buildings: A literature review. *Sustainable Cities and Society*, Vol. 45, pp. 231–242. DOI: 10.1016/j.scs.2018.09.029.
- Lindblad, H. (2019). Black boxing BIM: the public client's strategy in BIM implementation. *Construction Management and Economics*, Vol. 37, Issue 1, pp. 1–12. DOI: 10.1080/01446193.2018.1472385.
- Logothetis, S., Delinasiou, A., and Stylianidis, E. (2015). Building Information Modelling for cultural heritage: a review. In: Yen, Y.-N., Weng, K.-H., and Cheng, H.-M. (eds.). *ISPRS Annals of the Photogrammetry, Remote Sensing and Spatial Information Sciences*, Vol. II-5/W3. 25th International CIPA Symposium 2015, 31 August – 04 September 2015, Taipei, Taiwan, pp. 177–183. DOI: 10.5194/isprsannals-II-5-W3-177-2015.

- López, F. J., Lerones, P. M., Llamas, J., Gómez-García-Bermejo, J., and Zalama, E. (2018). A review of heritage building information modeling (H-BIM). *Multimodal Technologies and Interaction*, Vol. 2, No. 2, 21. DOI: 10.3390/mti2020021.
- Migilinskas, D., Popov, V., Juocevicius, V., and Ustinovichius, L. (2013). The benefits, obstacles and problems of practical BIM implementation. *Procedia Engineering*, Vol. 57, pp. 767–774. DOI: 10.1016/j.proeng.2013.04.097.
- Oesterreich, T. D. and Teuteberg, F. (2016). Understanding the implications of digitisation and automation in the context of Industry 4.0: A triangulation approach and elements of a research agenda for the construction industry. *Computers in Industry*, Vol. 83, pp. 121–39. DOI: 10.1016/j.compind.2016.09.006.
- Olawumi, T. O., Chan, D. W. M., Wong, J. K. W., and Chan, A. P. C. (2018). Barriers to the integration of BIM and sustainability practices in construction projects: A Delphi survey of international experts. *Journal of Building Engineering*, Vol. 20, pp. 60–71. DOI: 10.1016/j.jobbe.2018.06.017.
- Pocobelli, D. P., Boehm, J., Bryan, P., Still, J., and Grau-Bové, J. (2018). BIM for heritage science: a review. *Heritage Science*, Vol. 6, 30. DOI: 10.1186/s40494-018-0191-4.
- Roy, D., and Kalidindi, S. N. (2017). Critical challenges in management of heritage conservation projects in India. *Journal of Cultural Heritage Management and Sustainable Development*, Vol. 7, No. 3, pp. 290–307. DOI: 10.1108/JCHMSD-03-2017-0012.
- Simeone, D., Cursi, S., Toldo, I., and Carrara, G. (2014). BIM and knowledge management for building heritage. In: *Proceedings of ACADIA 14*, October 23–25, 2014, Los Angeles, California, USA, pp. 681–690.
- Tomšič, M., Mirtič, M., Šijanec Zavrl, M., and Rakušček, A. (2017). Energy renovation of cultural heritage buildings “by the book”. *Procedia Environmental Sciences*, Vol. 38, pp. 212–219. DOI: 10.1016/j.proenv.2017.03.108.
- Tweed, C. and Sutherland, M. (2007). Built cultural heritage and sustainable urban development. *Landscape and Urban Planning*, Vol. 83, Issue 1, pp. 62–69. DOI: 10.1016/j.landurbplan.2007.05.008.
- Volk, R., Stengel, J., and Schultmann, F. (2014). Building Information Modeling (BIM) for existing buildings — literature review and future needs. *Automation in Construction*, Vol. 38, pp. 109–127. DOI: 10.1016/j.autcon.2013.10.023.
- Wong, J. K. W. and Zhou, J. (2015). Enhancing environmental sustainability over building life cycles through green BIM: a review. *Automation in Construction*, Vol. 57, pp. 156–165. DOI: 10.1016/j.autcon.2015.06.003.
- Žurić, J., Zichi, A., and Azenha, M. (2022). Integrating HBIM and sustainability certification: A pilot study using GBC historic building certification. *International Journal of Architectural Heritage*, Vol. 17, Issue 9, pp. 1464–1483. DOI: 10.1080/15583058.2022.2042623.

ВНЕДРЕНИЕ BIM ПРИ РЕКОНСТРУКЦИИ ОБЪЕКТОВ КУЛЬТУРНОГО НАСЛЕДИЯ НА ПРОТЯЖЕНИИ ВСЕГО ЖИЗНЕННОГО ЦИКЛА ПРОЕКТА: ТЕКУЩЕЕ ИСПОЛЬЗОВАНИЕ, ПРЕИМУЩЕСТВА И ПРЕПЯТСТВИЯ

Бани Феризель Брахми*, Суад Сасси-Будемах

Лаборатория AVMF, Университет Константины 3 Салах Бубнидер, Константина, Алжир

*E-mail: feriel.brahmi@univ-constantine3.dz

Аннотация

Введение: информационное моделирование зданий (BIM) привлекает значительное внимание благодаря развитию сложных технологий и методик. Однако всесторонний обзор имеющихся литературных источников свидетельствует об отсутствии исследований в области применения BIM в управлении процессами проектирования и реконструкции с более широкой системной точки зрения. **Цель исследования** — восполнить этот пробел путем выявления и оценки текущего использования, преимуществ и препятствий, связанных с внедрением BIM на протяжении всего жизненного цикла проектов реконструкции. **Методология** исследования основана на проведении 31 структурированного интервью с опытными специалистами, использовавшими BIM в своих проектах. **Результаты** показывают, что основными преимуществами внедрения BIM в порядке убывания важности являются улучшение коллективного понимания проектного замысла, снижение рисков и повышение прогнозируемости результатов, более качественное проектирование и улучшенные эксплуатационные характеристики зданий, более точная проектная документация и повышение точности смет. Однако существует и ряд существенных препятствий: бюджет проекта, сложность моделирования исторических сооружений, стоимость найма BIM-специалистов и отсутствие знаний в области BIM. Полученные результаты могут способствовать внедрению BIM при реконструкции объектов культурного наследия и позволят участникам проекта сосредоточиться на реализации преимуществ и потенциальных возможностей использования BIM на протяжении всего жизненного цикла проекта, а также на решении важнейших задач, рассмотренных в данном исследовании.

Ключевые слова: внедрение BIM; реконструкция объектов культурного наследия; преимущества BIM; препятствия в BIM.

RESEARCH ON THE STANDARDIZATION AND VISUALIZATION PLATFORM FOR MONITORING AND TESTING DATA OF METRO CIVIL FACILITIES BASED ON BIG DATA

Qiaofeng Shen^{1*}, Chen Shen¹, Xun Liu¹, Yuan Jia², Jia Qian³

¹ Beijing Subway Construction Facilities Maintenance Co., Ltd., Beijing, China

² Beijing Jiutongqu Testing Technology Co., Ltd., Beijing, China

³ School of Transportation, Southeast University, Nanjing, China

*Corresponding author's email: 18813094515@163.com

Abstract

Introduction: With consideration for extensive standardized detection and monitoring data, multi-source data fusion analysis and comparison were implemented at cross-project and inter-regional levels to provide robust data support for the full life-cycle management of metro civil facilities. The **purpose of the study** was to integrate detection and monitoring data on metro bridges and tunnel structures and address the significant data isolation issue in existing systems and various units. Based on big data and Internet of Things technology, this paper investigates the standardized format of uploading, storage, processing, sharing, and other types of managing detection and monitoring data on metro bridges and tunnel structures. Additionally, a third-party data standardization and visualization platform for bridges and tunnel structures was developed, ensuring integration of detection and monitoring data fusion. In the course of the study, the following **methods** were used: theoretical analysis and software system development. As a **result**, the practicability and feasibility of the platform were verified through practical applications.

Keywords: metro civil facilities, big data platform, detection and monitoring, data standardization, integrated analysis.

Introduction

With the rapid development of urban rail transit, the number of such civil facilities as bridges and tunnels increases. As the years of operation increase and the external environment constantly changes, the structure of civil facilities has undergone subtle changes, including shifts in existing diseases and the emergence of new ones. The monitoring and testing of bridges and tunnels have generated a large volume of paper records, charts, images, etc. (Fig. 1), encompassing various types of data from different sources, lacking unified data format standards, and leading to significant data fragmentation (Fig. 2). There is also a lack of an integrated management platform that would combine engineering structure overview, historical monitoring data, metro safety assessment, and structural maintenance history for the comprehensive application of civil engineering facilities. As a result, it is quite difficult to achieve the auxiliary management functions of visual querying, intelligent analysis, and comprehensive judgment of metro civil engineering structure operation and maintenance data.

The operation and maintenance management of urban rail transit civil engineering facilities has significant social benefits and broad application prospects. Many metro operators, manufacturers of information systems, and universities in China have started to dedicate more research and development

efforts to the informationization of the operation and maintenance management of urban rail transit. For instance, Agrawal et al. (2011), Assunção et al. (2015), Beyer and Laney (2012), Chen and Zhang (2014), Mayer-Schönberger and Cukier (2013) introduced the definition, potential applications, and development trends of big data and cloud computing. Li (2020) proposed the fundamental concept of creating a cloud platform for managing urban rail transit detection data, focusing on system architecture and system function design. Tao et al. (2019, 2021) implemented a railway infrastructure testing and monitoring data management and integrated analysis service platform based on big data technology. Chen et al. (2012), Demirkan and Delen (2013), Ding and Guo (2015), Guo et al. (2016), Khribi et al. (2009), Lv et al. (2015), Peng et al. (2017) investigated the application of big data in various fields. Luo et al. (2019) and Yang (2021) analyzed the application and prospects of BIM technology in intelligent operation and maintenance in the railway infrastructure and urban rail transit industry. Vitri and Herman (2019) studied the basic infrastructure maintenance system for improving the quality of infrastructure services. Jamshidi et al. (2017) investigated the method of big data analysis for rail failure risk assessment. Wu et al. (2010) and Zach and Reiser (2015) studied the application of cloud storage.



Fig. 1. Paper ledgers (charts)



Fig. 2. Standards for different data formats

However, most of the above-mentioned systems (GB 50911-2013 (Standardization Administration of the People's Republic of China, 2013), DB11/T 1167-2015 (Beijing Bureau of Quality and Technical Supervision, 2015), DB11/T 718-2016 (Beijing Bureau of Quality and Technical Supervision, 2016), GB/T 39559.2-2020 (Standardization Administration of the People's Republic of China, 2020)) only implement the related data collection and display functions and have shortcomings in data standardization, intelligent collection, and data fusion. These systems are unable to perform deep data analysis and safety control value deduction from the vast amount of operation and maintenance data, including monitoring, detection, and evaluation data.

Research on combined detection technology

In terms of data analysis and utilization, the data formats across different monitoring and testing units are quite diverse and independent of each other. As a result, the standardized data uploading interface, analysis algorithm, data visualization, and fusion analysis result display functions need to be redeveloped. Besides, data uploading standards vary for different sources, and the absence of batch processing functions for unstructured data leads to low data utilization.

This paper aims to achieve the fusion of monitoring and testing data for metro bridges and tunnel structures, addressing the significant data isolation issue between existing systems and various units. It will collect data sources and types, develop third-party monitoring and testing data uploading standards, and establish third-party data standardization and visualization to achieve modularization, standardization, platformization, and visualization. The platform includes a data layer, a service layer, and an application layer. The technical architecture of the platform is shown in Fig. 3, and the platform's functional modules are shown in Fig. 4.

The data layer connects data from various sources, with the fundamental information coming from the infrastructure ledger of the management

unit. The test data comprises special test data from the third-party testing unit, with the primary data sources being the test reports and original records from previous years. The monitoring data includes all manual monitoring data from third-party monitoring units, with the primary data sources being the monitoring reports and original records from previous years. Data from various sources is classified and stored to achieve the integration of multi-channel data information. The data layer manages the storage of structured data, unstructured image data, report files, as well as monitoring, detection, and safety assessment. It also imports basic account information for civil engineering facilities such as bridges and tunnels, providing a data information basis for data fusion analysis. The service layer offers such services as data standardization processing, batch import, fusion analysis, and data visualization for each application layer. This fully supports the statistical analysis of monitoring and testing data for metro civil engineering facilities, disease type information description, state evaluation, treatment suggestions, and more.

Key technology

The system platform utilizes stable and advanced information technology for data classification storage, big data component integration, data utilization and deployment, efficient retrieval, and platform interface optimization. Additionally, it establishes a third-party monitoring and testing data platform for civil engineering facilities and reserves interfaces for future system upgrades.

The system platform utilizes big data technology based on the Hadoop ecosystem to achieve efficient storage and processing of massive data. This includes data cleaning, deduplication, aggregation, and correlation analysis processes. Through the MapReduce model for parallel computing, it is possible to accelerate the processing of large-scale datasets, quickly extract useful information and patterns, and achieve intelligent analysis and processing of stored data, to provide more

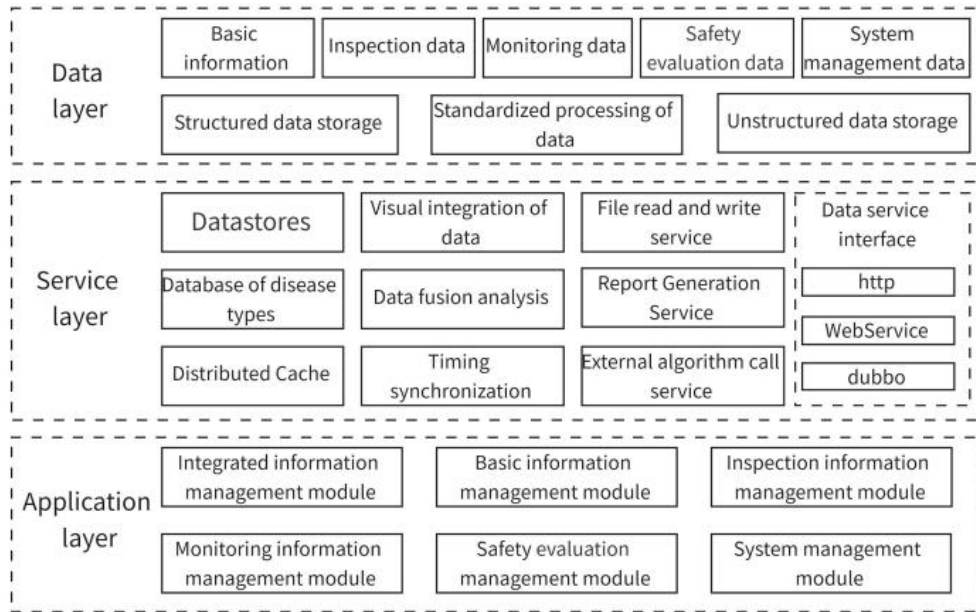


Fig. 3. Platform technology architecture

comprehensive and accurate support for the technical evaluation and subsequent management decisions regarding bridges and tunnels.

1. Data Classification Storage Technology

The platform comprehensively processes basic information data on bridges, health monitoring data, test management data, etc. The data organization

forms vary in different scenarios. To meet the processing requirements of this type of multi-source heterogeneous data, the platform comprehensively utilizes multiple storage technologies to ensure efficient and secure data storage.

Data such as basic bridge information and test management information can be considered

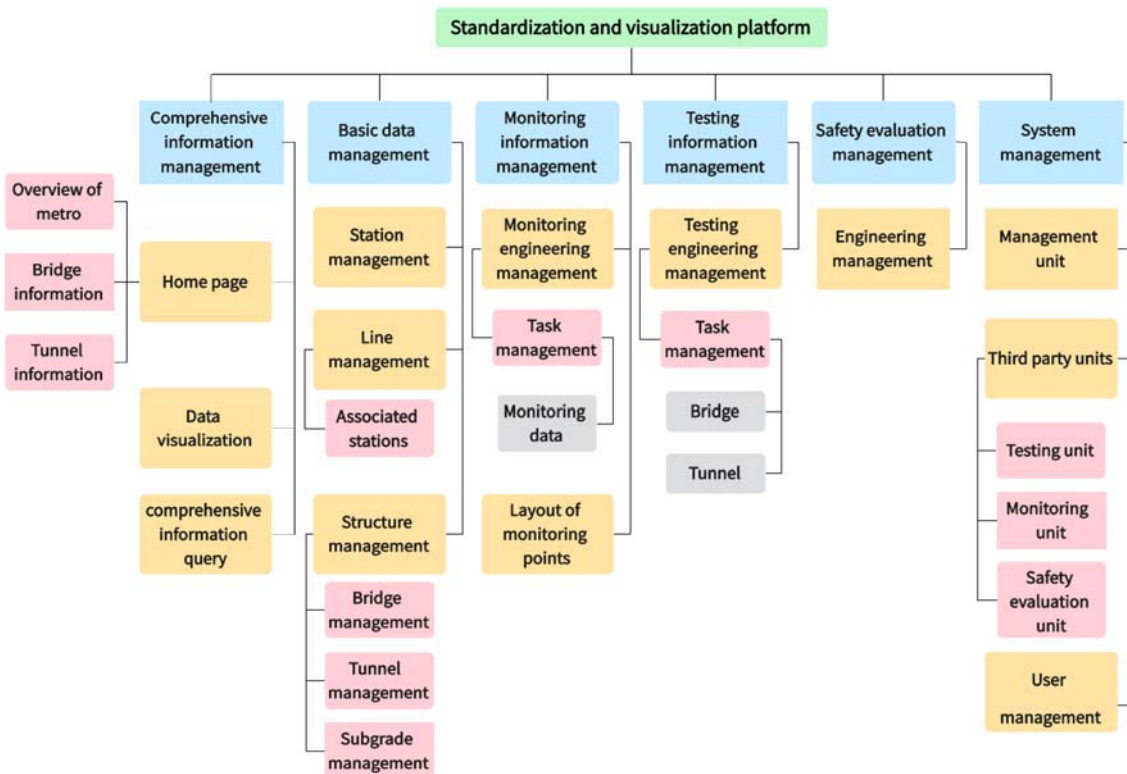


Fig. 4. Platform's functional modules

structured data, with high integrity and consistency, and a strict correlation between the data. The system uses the MySQL structured database to process this part of the business data and utilizes the SQL language for querying and managing the data.

Bridge health monitoring data can be considered time series data, which is arranged in a time sequence and has the characteristics of a large amount of data, more writing and less reading, and more statistical indicators. The system uses the TDengine time series database to store and query monitoring data, thereby improving monitoring data processing capabilities and reducing disk space occupancy.

Such information as test reports and images of diseases generally exists in the form of pictures and files. A single file has a small size, but there are many files. Therefore, the system uses the FastDFS distributed file system to store attachment files, which can effectively expand the storage capacity and meet the later operation and maintenance requirements.

2. Integration Technology for Big Data Components

The system uses the Spring Cloud framework to effectively integrate the big data-related components used in the platform development process, thereby achieving high service availability and improving the stability and scalability of the platform. A microservice is a software architecture style that divides applications into smaller components known as services, each of which runs, expands independently, and interacts through a lightweight communication mechanism. Based on the business requirements, the system divides the functional level and designs several microservices, including basic information management service, monitoring information management service, detection information management service, safety assessment management service, and comprehensive information management service.

Spring Cloud is an open-source microservice framework that provides out-of-the-box components such as service discovery, configuration management, intelligent routing, control bus, cluster state management, and more. By using the Spring Cloud framework in platform development, developers can focus on business-related functional logic and improve development efficiency. According to the microservice framework, function expansion only targets a specific service, without affecting other services, and enhances the overall availability and scalability of the system.

3. Data Utilization and Deployment Technology

In this study, containerized deployment is used for platform deployment, which is a technology that encapsulates applications and their dependencies in containers and allows them to run consistently

across different environments. The use of container deployment can simplify the process of deploying applications, allowing developers to deploy applications to the production environment faster. Additionally, it can improve the portability of the application program, enabling it to run on different operating systems and hardware platforms.

When it comes to selecting a container deployment technology, the platform utilizes the Podman container engine, which can be used to create, run, and manage containers. Compared to other container engines, Podman does not need to run daemons, so it can be better integrated with the security policy of the system. Podman uses the Linux namespace to isolate the container from the host operating system, making the container more secure. By using the Podman container engine for system container deployment, the system's development and deployment process is simplified, its hardware compatibility is improved, and its migration and maintenance are facilitated.

4. Efficient Data Retrieval Technology

When searching for unstructured text content such as disease descriptions and disposal operations, the traditional SQL LIKE operation is inefficient because it is not suitable for large-scale data and only supports basic pattern matching, so it cannot perform advanced text analysis. The system utilizes Elasticsearch as a search engine, enabling the search, analysis, and exploration of a large volume of detection and monitoring data. This facilitates the comprehensive life-cycle management of platform detection and monitoring data, as well as efficient full-text search. Elasticsearch uses reverse indexing technology, and its basic idea is to take each word in a text record as a keyword and associate the keyword with the text record containing it. During the system's operation, Elasticsearch synchronizes the data from the database, utilizes the word segmentation controller to segment the relevant sentences, and then stores the weights and word segmentation results in the database. Later, when the user searches for data, the results are ranked and scored according to their weight, and finally, the returned results are presented to the user.

5. System Platform Interface Optimization Technology

The platform utilizes the React framework to optimize the display of the user interface and enhance the user experience. React is an open-source JavaScript front-end framework for building web-based user interfaces. Compared to other front-end frameworks, React uses a virtual DOM mechanism to make page rendering more efficient. It also applies a component-based development mode to page development, making the code more modular and easier to maintain. Meanwhile, React uses the architecture design of one-way data flow to reduce

code coupling. In addition, the React community offers numerous open-source components, making it easy to learn and use the developed user interface.

In the bridge visualization display, WebGL is used to connect the multi-dimensional bridge data with the three-dimensional model. WebGL is a technology for rendering 3D graphics in a web browser that can be used with HTML5 through the JavaScript API. The system uses WebGL technology to display BIM visual models of bridges and tunnels. Based on this, users can interact with the visual models in various ways, such as rotation, scaling, translation, and clicking, thereby comprehensively viewing the multi-dimensional information of bridges and improving the system's usability.

Main functions

The platform supports batch import, timing synchronization, visual display, and long-term storage of structured and unstructured data from different sources, as well as statistical analysis of data across time and structural dimensions. It provides platform support for predicting disease trends and evaluating the state of metro civil engineering facilities. The functional architecture of the platform is illustrated in Fig. 5.

1. Data Import

Based on the standard data files of various types, the platform supports batch import of different data types. The collected data includes a basic information ledger, monitoring and testing data, safety assessment reports, and more. Based on the data sources, the monitoring data can be categorized as fixed online monitoring data, on-site small-scale

instrument inspection or manual inspection data, and mobile large-scale equipment inspection data.

2. Data Storage

The relational database MySQL is used for storing structural data such as metro civil engineering facility tests and basic ledgers. Health monitoring data can be considered time series data, which is arranged in a time sequence and has the characteristics of a large amount of data, more writing and less reading, and more statistical indicators. The system uses the TDengine time series database to store monitoring data. Besides, the system utilizes the FastDFS distributed file system to store attachment files, such as test reports, disease pictures, and other unstructured data.

3. Data Management

Based on the confirmed monitoring items, including settlement observation, convergence (horizontal and vertical), horizontal displacement, mid-span deflection, layered settlement of soil, groundwater level, and combined with the calculation methods for various monitoring data, an automatic calculation module for monitoring data is constructed to automatically calculate the change, previous cumulative change, current cumulative change, deformation rate, and early warning level.

The rules for division and naming of the structure, fields, and methods for third-party testing and monitoring data entry are clarified. This standardizes the operational procedures for third-party testing and monitoring projects at the data level and forms data standard documents to provide operational guidelines for future projects. Additionally, the

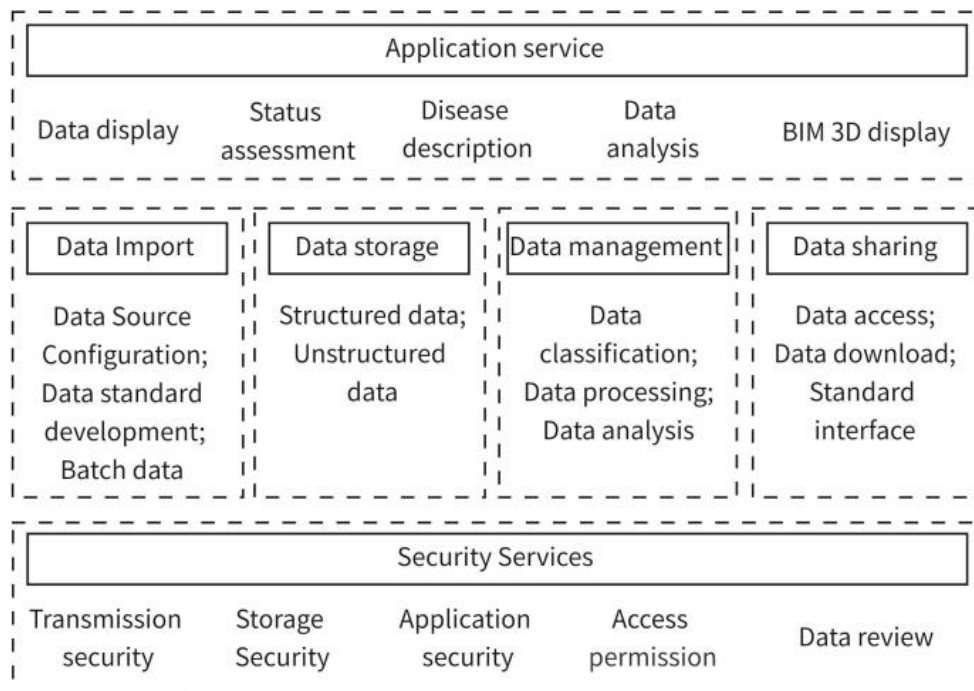


Fig. 5. Platform's functional architecture

standardized data structure lays the foundation for the subsequent construction of the standardization and visualization platform.

The collected data is classified, and different modules of the system platform are created to realize the corresponding functions. The system platform mainly includes six modules: comprehensive information management, basic information management, monitoring information management, detection information management, safety assessment management, and system management. The comprehensive information management module is used to display data comprehensively. The basic management module is responsible for maintaining metro structure information. The module for monitoring and detection information management as well as safety assessment is used to maintain all monitoring information, detection information, and safety assessment information under the condition of perfect basic information. The system management module is responsible for maintaining the information of each unit and user.

4. Data Sharing

Different management rights are assigned based on different roles to achieve visibility differentiation for modules and pages across various units and departments. The construction of the system platform meets the needs of management units and achieves the standardized integration and visual display of basic information, detection information, monitoring information, safety assessment, and other information about the bridge and tunnel structure. This provides a collaborative operation platform based on industry standards for management units and third-party units, improving the data management quality of management units and enhancing operation and maintenance efficiency.

5. Security Services

The server side of the system deployment is a private cloud server, which ensures that the information stored, used, and transmitted will not be leaked to unauthorized users or entities, and

will not be tampered with by unauthorized users. It also prevents authorized users from improperly tampering with the system and information. With sufficient backup data storage space and a standardized backup control interface, the system platform achieves standardized management of system backups, supports backup requirements for different types of data, and does not affect the system’s application during backup. Based on this, the system platform not only meets the basic requirements of data storage and backup, but also supports data recovery. Data can be recovered under different faults and unexpected situations.

6. Application Service

In the entire data management process of “import-storage-management-display”, various functions such as data display, disease treatment suggestions, trend analysis, state evaluation, and comprehensive display are realized. This provides platform support for efficiently utilizing detection and monitoring data. The complete process management of data is illustrated in Fig. 6.

Using the historical detection data of a specific bridge as an example, both structured and unstructured data, such as photos, will be processed according to established data standards to transform non-standard data into standardized data. Subsequently, the data will be imported into the system platform mentioned in this paper. This has enabled the digital storage and retrieval of historical detection data, as well as the ability to conduct queries and analyses using various dimensional filtering criteria. Based on this, 2D and 3D data visualization can be achieved by integrating with maps, BIM, and other hosting platforms (Table 1).

Application case

Based on the research results of data standardization, a component-level database for metro bridges and a pile number-level database for metro tunnels have been built, providing a unified structural database for the analysis and application of subsequent detection and monitoring data.

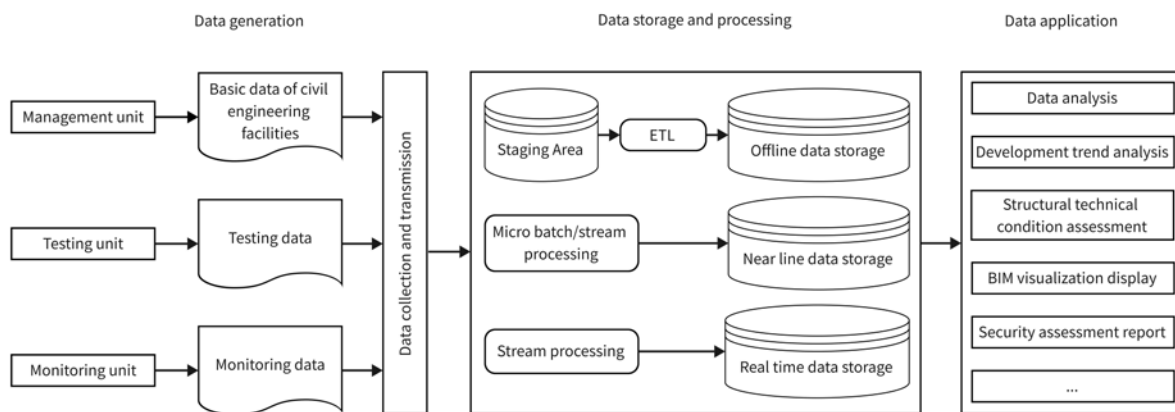




Fig. 6. Complete process management of data

Table 1. Schematic diagram of data processing and display

1. Inspection report	 <p style="text-align: center; font-size: small;">Fig. 1 MI6 Aging cracks on the surface</p>  <p style="text-align: center; font-size: small;">Fig. 2 MI7 Aging cracks on the surface</p>	<table border="1" style="width: 100%; border-collapse: collapse; font-size: x-small;"> <thead> <tr> <th>No.</th> <th>Stay cables</th> <th>Disease type</th> <th>Disease description</th> </tr> </thead> <tbody> <tr> <td>9</td> <td rowspan="4" style="text-align: center;">MI6</td> <td>Aging cracks on the surface</td> <td>Long surface aging cracks on the PE sheath</td> </tr> <tr> <td>10</td> <td>Scratch</td> <td>One point like scratch appeared at 41.25m from the bottom</td> </tr> <tr> <td>11</td> <td>Scratch</td> <td>One scratch appeared at 44.5m from the bottom, about 4cm in length</td> </tr> <tr> <td>12</td> <td>Scratch</td> <td>One scratch appeared at 37.5m from the bottom, about 3cm in length</td> </tr> <tr> <td>13</td> <td rowspan="3" style="text-align: center;">MI7</td> <td>Aging cracks on the surface</td> <td>Long surface aging cracks</td> </tr> <tr> <td>14</td> <td>Scratch</td> <td>One scratch appeared at 24m from the bottom, about 4cm in length</td> </tr> <tr> <td>15</td> <td>Scratch</td> <td>One scratch appeared at 32.75m from the bottom, about 6cm in length</td> </tr> </tbody> </table>	No.	Stay cables	Disease type	Disease description	9	MI6	Aging cracks on the surface	Long surface aging cracks on the PE sheath	10	Scratch	One point like scratch appeared at 41.25m from the bottom	11	Scratch	One scratch appeared at 44.5m from the bottom, about 4cm in length	12	Scratch	One scratch appeared at 37.5m from the bottom, about 3cm in length	13	MI7	Aging cracks on the surface	Long surface aging cracks	14	Scratch	One scratch appeared at 24m from the bottom, about 4cm in length	15	Scratch	One scratch appeared at 32.75m from the bottom, about 6cm in length																																																																																																									
No.	Stay cables	Disease type	Disease description																																																																																																																																			
9	MI6	Aging cracks on the surface	Long surface aging cracks on the PE sheath																																																																																																																																			
10		Scratch	One point like scratch appeared at 41.25m from the bottom																																																																																																																																			
11		Scratch	One scratch appeared at 44.5m from the bottom, about 4cm in length																																																																																																																																			
12		Scratch	One scratch appeared at 37.5m from the bottom, about 3cm in length																																																																																																																																			
13	MI7	Aging cracks on the surface	Long surface aging cracks																																																																																																																																			
14		Scratch	One scratch appeared at 24m from the bottom, about 4cm in length																																																																																																																																			
15		Scratch	One scratch appeared at 32.75m from the bottom, about 6cm in length																																																																																																																																			
2. Data standardization processing	<div style="font-size: x-small;"> Daxuecheng - North Daxuecheng Line Fangshan Inspection results Deterioration level Assessment Results Conclusion and suggestions </div> <div style="font-size: x-small; margin-top: 5px;"> concrete cracks Component: <input type="text"/> Disease types: <input type="text"/> Accompanying diseases: <input type="text"/> Repair condition: <input type="text"/> </div> <div style="font-size: x-small; margin-top: 5px;"> + Add Batch Delete Search Reset Batch Import </div> <table border="1" style="width: 100%; border-collapse: collapse; font-size: x-small;"> <thead> <tr> <th><input type="checkbox"/></th> <th>Component</th> <th>Disease type</th> <th>Derived disease</th> <th>Crack location</th> <th>Quantity</th> <th>Width (mm)</th> <th>Depth (mm)</th> <th>Length (mm)</th> <th>Deduction value</th> <th>Repair condition</th> <th>Operate</th> </tr> </thead> <tbody> <tr> <td><input type="checkbox"/></td> <td>17 # beam bottom plate</td> <td>longitudinal crack</td> <td>leakage</td> <td></td> <td>1</td> <td>1</td> <td></td> <td>2.5</td> <td>0</td> <td><input type="checkbox"/></td> <td>Edit Delete</td> </tr> <tr> <td><input type="checkbox"/></td> <td>13 # beam bottom plate</td> <td>longitudinal crack</td> <td>leakage</td> <td></td> <td>1</td> <td>1</td> <td></td> <td>0.6</td> <td>0</td> <td><input type="checkbox"/></td> <td>Edit Delete</td> </tr> <tr> <td><input type="checkbox"/></td> <td>11 # beam bottom plate</td> <td>transverse crack</td> <td>leakage</td> <td></td> <td>1</td> <td>1</td> <td></td> <td>1.2</td> <td>0</td> <td><input type="checkbox"/></td> <td>Edit Delete</td> </tr> <tr> <td><input type="checkbox"/></td> <td>29 # beam left web plate</td> <td>longitudinal crack</td> <td>leakage</td> <td></td> <td>1</td> <td>0.03</td> <td></td> <td>0.4</td> <td>0</td> <td><input type="checkbox"/></td> <td>Edit Delete</td> </tr> <tr> <td><input type="checkbox"/></td> <td>24 # beam bottom plate</td> <td>longitudinal crack</td> <td>leakage</td> <td></td> <td>1</td> <td>0.03</td> <td></td> <td>1</td> <td>0</td> <td><input type="checkbox"/></td> <td>Edit Delete</td> </tr> <tr> <td><input type="checkbox"/></td> <td>21 # beam bottom plate</td> <td>transverse crack</td> <td>-</td> <td></td> <td>28</td> <td>0.2</td> <td></td> <td>1.8</td> <td>0</td> <td><input type="checkbox"/></td> <td>Edit Delete</td> </tr> <tr> <td><input type="checkbox"/></td> <td>21 # beam left web plate</td> <td>vertical crack</td> <td>-</td> <td></td> <td>1</td> <td>0.22</td> <td></td> <td>1.4</td> <td>0</td> <td><input type="checkbox"/></td> <td>Edit Delete</td> </tr> <tr> <td><input type="checkbox"/></td> <td>21 # beam left web plate</td> <td>vertical crack</td> <td>-</td> <td></td> <td>1</td> <td>0.24</td> <td></td> <td>1.4</td> <td>0</td> <td><input type="checkbox"/></td> <td>Edit Delete</td> </tr> <tr> <td><input type="checkbox"/></td> <td>21 # beam left web plate</td> <td>vertical crack</td> <td>-</td> <td></td> <td>1</td> <td>0.22</td> <td></td> <td>1.5</td> <td>0</td> <td><input type="checkbox"/></td> <td>Edit Delete</td> </tr> <tr> <td><input type="checkbox"/></td> <td>21 # beam left web plate</td> <td>vertical crack</td> <td>-</td> <td></td> <td>1</td> <td>0.3</td> <td></td> <td>1.3</td> <td>0</td> <td><input type="checkbox"/></td> <td>Edit Delete</td> </tr> </tbody> </table>		<input type="checkbox"/>	Component	Disease type	Derived disease	Crack location	Quantity	Width (mm)	Depth (mm)	Length (mm)	Deduction value	Repair condition	Operate	<input type="checkbox"/>	17 # beam bottom plate	longitudinal crack	leakage		1	1		2.5	0	<input type="checkbox"/>	Edit Delete	<input type="checkbox"/>	13 # beam bottom plate	longitudinal crack	leakage		1	1		0.6	0	<input type="checkbox"/>	Edit Delete	<input type="checkbox"/>	11 # beam bottom plate	transverse crack	leakage		1	1		1.2	0	<input type="checkbox"/>	Edit Delete	<input type="checkbox"/>	29 # beam left web plate	longitudinal crack	leakage		1	0.03		0.4	0	<input type="checkbox"/>	Edit Delete	<input type="checkbox"/>	24 # beam bottom plate	longitudinal crack	leakage		1	0.03		1	0	<input type="checkbox"/>	Edit Delete	<input type="checkbox"/>	21 # beam bottom plate	transverse crack	-		28	0.2		1.8	0	<input type="checkbox"/>	Edit Delete	<input type="checkbox"/>	21 # beam left web plate	vertical crack	-		1	0.22		1.4	0	<input type="checkbox"/>	Edit Delete	<input type="checkbox"/>	21 # beam left web plate	vertical crack	-		1	0.24		1.4	0	<input type="checkbox"/>	Edit Delete	<input type="checkbox"/>	21 # beam left web plate	vertical crack	-		1	0.22		1.5	0	<input type="checkbox"/>	Edit Delete	<input type="checkbox"/>	21 # beam left web plate	vertical crack	-		1	0.3		1.3	0	<input type="checkbox"/>	Edit Delete
<input type="checkbox"/>	Component	Disease type	Derived disease	Crack location	Quantity	Width (mm)	Depth (mm)	Length (mm)	Deduction value	Repair condition	Operate																																																																																																																											
<input type="checkbox"/>	17 # beam bottom plate	longitudinal crack	leakage		1	1		2.5	0	<input type="checkbox"/>	Edit Delete																																																																																																																											
<input type="checkbox"/>	13 # beam bottom plate	longitudinal crack	leakage		1	1		0.6	0	<input type="checkbox"/>	Edit Delete																																																																																																																											
<input type="checkbox"/>	11 # beam bottom plate	transverse crack	leakage		1	1		1.2	0	<input type="checkbox"/>	Edit Delete																																																																																																																											
<input type="checkbox"/>	29 # beam left web plate	longitudinal crack	leakage		1	0.03		0.4	0	<input type="checkbox"/>	Edit Delete																																																																																																																											
<input type="checkbox"/>	24 # beam bottom plate	longitudinal crack	leakage		1	0.03		1	0	<input type="checkbox"/>	Edit Delete																																																																																																																											
<input type="checkbox"/>	21 # beam bottom plate	transverse crack	-		28	0.2		1.8	0	<input type="checkbox"/>	Edit Delete																																																																																																																											
<input type="checkbox"/>	21 # beam left web plate	vertical crack	-		1	0.22		1.4	0	<input type="checkbox"/>	Edit Delete																																																																																																																											
<input type="checkbox"/>	21 # beam left web plate	vertical crack	-		1	0.24		1.4	0	<input type="checkbox"/>	Edit Delete																																																																																																																											
<input type="checkbox"/>	21 # beam left web plate	vertical crack	-		1	0.22		1.5	0	<input type="checkbox"/>	Edit Delete																																																																																																																											
<input type="checkbox"/>	21 # beam left web plate	vertical crack	-		1	0.3		1.3	0	<input type="checkbox"/>	Edit Delete																																																																																																																											
3. Data display	<div style="font-size: x-small;"> Statistics of overall technical condition 2022 </div> <div style="font-size: x-small; margin-top: 5px;"> Metro line: All S1 line 1 line 2 line 5 udfold > Bridge type: All Concrete Box Girder Bridge Steel and Concrete Composite Box Girder Bridge udfold > Bridge age: All ≤10 10-20 20-30 ≥30 Bridge parts: All Bridge Decking Superstructure Substructure </div> <div style="font-size: x-small; margin-top: 10px;"> <table border="1" style="width: 100%; border-collapse: collapse; text-align: center;"> <tr> <th>Level</th> <th>Count</th> </tr> <tr> <td>First level</td> <td>35</td> </tr> <tr> <td>Second level</td> <td>25</td> </tr> <tr> <td>Third level</td> <td>10</td> </tr> <tr> <td>Fourth level</td> <td>5</td> </tr> <tr> <td>Fifth level</td> <td>5</td> </tr> </table> </div> <div style="font-size: x-small; margin-top: 10px;"> <table border="1" style="width: 100%; border-collapse: collapse; text-align: center;"> <tr> <th>Category</th> <th>Percentage</th> </tr> <tr> <td>Erosion by water</td> <td>35.9%</td> </tr> <tr> <td>Substructure</td> <td>6.8%</td> </tr> <tr> <td>Crack</td> <td>5.9%</td> </tr> <tr> <td>Breakage</td> <td>11.6%</td> </tr> <tr> <td>Spalling</td> <td>6.6%</td> </tr> <tr> <td>Reticular crack</td> <td>5.9%</td> </tr> <tr> <td>Superstructure</td> <td>93%</td> </tr> </table> </div> <div style="font-size: x-small; margin-top: 10px;"> Trend chart of overall assessment 2020-2021 All bridges > All line > </div> <div style="font-size: x-small; margin-top: 10px;"> <table border="1" style="width: 100%; border-collapse: collapse; text-align: center;"> <tr> <th>Year</th> <th>First</th> <th>Second</th> <th>Three</th> <th>Fourth</th> <th>Fifth</th> </tr> <tr> <td>2020</td> <td>5</td> <td>10</td> <td>15</td> <td>20</td> <td>25</td> </tr> <tr> <td>2021</td> <td>10</td> <td>20</td> <td>30</td> <td>35</td> <td>40</td> </tr> </table> </div> <div style="font-size: x-small; margin-top: 10px;"> Recent situation of bridges All line > </div> <table border="1" style="width: 100%; border-collapse: collapse; font-size: x-small;"> <thead> <tr> <th>Name</th> <th>Line</th> <th>Last inspection time</th> <th>Quantity of diseases</th> <th>BCI value</th> <th>Level</th> <th>Operate</th> </tr> </thead> <tbody> <tr> <td></td> <td>Line 5</td> <td>November 2022</td> <td>7</td> <td>80</td> <td>Second</td> <td>Details</td> </tr> <tr> <td></td> <td>Line 5</td> <td>November 2022</td> <td>20</td> <td>80</td> <td>Second</td> <td>Details</td> </tr> <tr> <td></td> <td>Line 5</td> <td>November 2022</td> <td>7</td> <td>80</td> <td>Second</td> <td>Details</td> </tr> <tr> <td></td> <td>Line 5</td> <td>November 2022</td> <td>7</td> <td>80</td> <td>Second</td> <td>Details</td> </tr> <tr> <td></td> <td>Line 5</td> <td>November 2022</td> <td>7</td> <td>80</td> <td>Second</td> <td>Details</td> </tr> </tbody> </table>		Level	Count	First level	35	Second level	25	Third level	10	Fourth level	5	Fifth level	5	Category	Percentage	Erosion by water	35.9%	Substructure	6.8%	Crack	5.9%	Breakage	11.6%	Spalling	6.6%	Reticular crack	5.9%	Superstructure	93%	Year	First	Second	Three	Fourth	Fifth	2020	5	10	15	20	25	2021	10	20	30	35	40	Name	Line	Last inspection time	Quantity of diseases	BCI value	Level	Operate		Line 5	November 2022	7	80	Second	Details		Line 5	November 2022	20	80	Second	Details		Line 5	November 2022	7	80	Second	Details		Line 5	November 2022	7	80	Second	Details		Line 5	November 2022	7	80	Second	Details																																												
Level	Count																																																																																																																																					
First level	35																																																																																																																																					
Second level	25																																																																																																																																					
Third level	10																																																																																																																																					
Fourth level	5																																																																																																																																					
Fifth level	5																																																																																																																																					
Category	Percentage																																																																																																																																					
Erosion by water	35.9%																																																																																																																																					
Substructure	6.8%																																																																																																																																					
Crack	5.9%																																																																																																																																					
Breakage	11.6%																																																																																																																																					
Spalling	6.6%																																																																																																																																					
Reticular crack	5.9%																																																																																																																																					
Superstructure	93%																																																																																																																																					
Year	First	Second	Three	Fourth	Fifth																																																																																																																																	
2020	5	10	15	20	25																																																																																																																																	
2021	10	20	30	35	40																																																																																																																																	
Name	Line	Last inspection time	Quantity of diseases	BCI value	Level	Operate																																																																																																																																
	Line 5	November 2022	7	80	Second	Details																																																																																																																																
	Line 5	November 2022	20	80	Second	Details																																																																																																																																
	Line 5	November 2022	7	80	Second	Details																																																																																																																																
	Line 5	November 2022	7	80	Second	Details																																																																																																																																
	Line 5	November 2022	7	80	Second	Details																																																																																																																																

The bridge structure defines the component information of a specific bridge based on standardized splitting and naming rules, and all component information of a specific bridge can be quickly entered through an Excel spreadsheet. The tunnel structure is defined according to the pile number, and the detection and monitoring data is associated with the pile number of the tunnel structure.

The data types for all detection and monitoring items in the system platform are classified. Data types such as “text”, “number”, “option”, “option + text”, and “image” are sorted and configured

according to field requirements. Let us consider the “concrete crack” detection item in the tunnel as an example. According to standard documents, the “crack location” field is composed of “part + pile number + pile mileage range + specific location”. The data type for the part and specific location is “option + text”, the data type for the pile number is “option”, and the data type for the pile mileage range is “number”. During the development process of the system platform, corresponding functional modules are designed based on the data types of each component, achieving convenient operation and

standardized management during the input process (Fig. 7).

A standardized data import template has been designed for each detection and monitoring item in the system platform. It organizes the components of each field under a specific detection item and monitoring item in a table format in batches. It parses each column of the list using Python scripts and matches the components of each field with specific rules to achieve batch import of data standardization templates (Figs. 8 and 9).

Fig. 10 demonstrates the metro overview interface displayed on the home page of the system's comprehensive information management module. This interface provides an intuitive display of the distribution of metro lines, as well as basic information such as the number of metro lines, the total mileage of lines, and the number of stations. Furthermore, it allows querying the number, length, and corresponding proportions of bridges, tunnels, and roadways. The system features a user-friendly

interface and practical functions, enabling the electronic management of metro line information.

Fig. 11 illustrates the data visualization interface of the system's comprehensive information management module. The visualization page displays the geographical location of a single bridge or tunnel, the BIM model, bridge components, detection data over the years, various data statistics, and more. By clicking the model, you can view the disease status of individual components.

Fig. 12 presents the interface for data chain analysis. The data chain analysis interface enables statistical analysis of both the temporal dimension and the structural dimension. Analyses can be conducted by selecting the structure type, data type, disease type, and line. Meanwhile, this interface supports the export function for both images and data.

In addition to the functional interface shown in the figure, the system platform also provides functional interfaces such as bridge evaluation, tunnel evaluation, comprehensive information

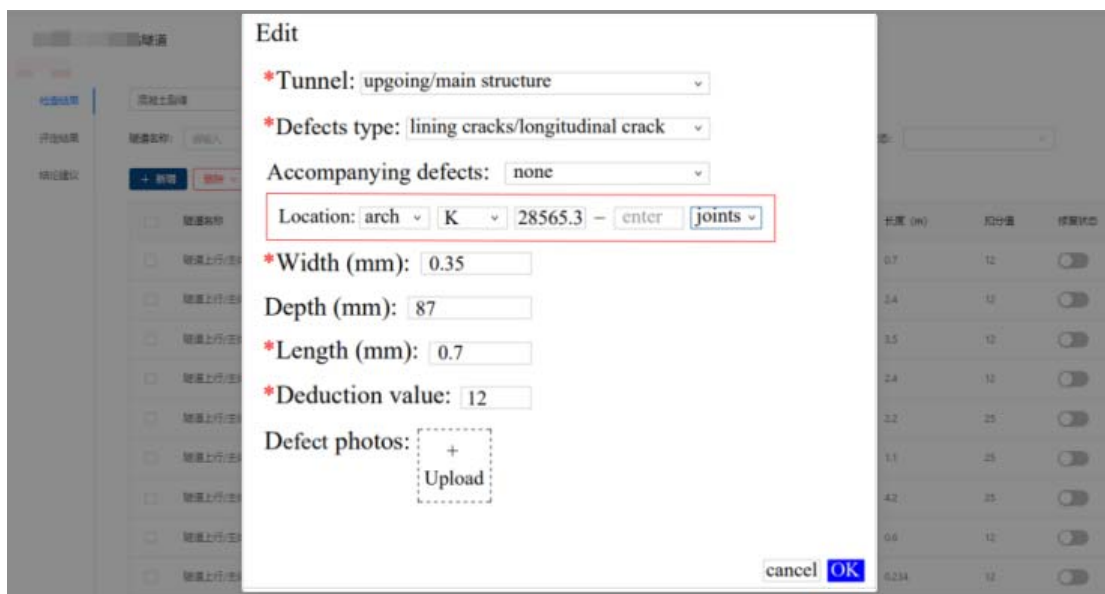


Fig. 7. Editing of tunnel detection result information

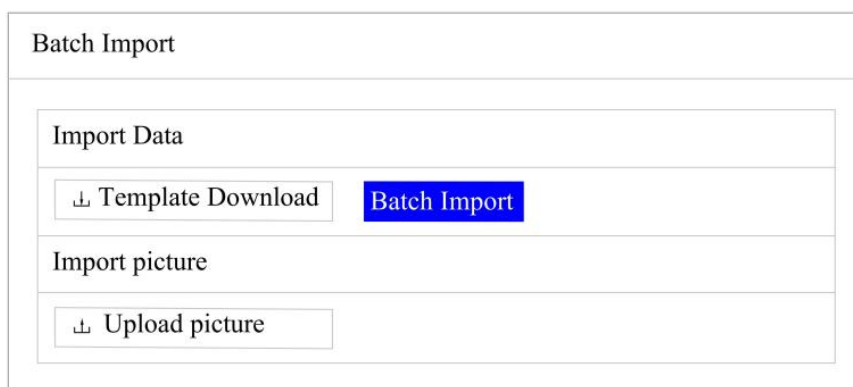


Fig. 8. Entry fields for batch data import

1	Tunnel direction	Structure type	Defects type	Accompanying defects	Defect location	Defect location/K	Defect location/Pile A	Defect location/Pile B	Specific location	Width/mm	Depth/mm	Length/m	Deduction value	Picture number
2	down	Main structure	Lining cracks/longitudinal cracks		left sidewall	K	1638.6		0.5m from the bottom	0.25	63	1.2		Picture1
3	down	Main structure	Lining cracks/longitudinal cracks		left sidewall	K	1639		0.4m from the bottom	0.23	84	2.1		Picture2
4	down	Main structure	Lining cracks/longitudinal cracks		left sidewall	K	1731.6		0.6m from the bottom	0.28	64	2.1		Picture3
5	down	Main structure	Lining cracks/longitudinal cracks		left sidewall	K	1753		0.5m from the bottom	0.25	60	2.1		Picture4
6	down	Main structure	Lining cracks/longitudinal cracks		left sidewall	K	1755		0.3m from the bottom	0.26	74	2		Picture5
7	down	Main structure	Lining cracks/longitudinal cracks		left sidewall	K	1758.2		0.7m from the bottom	0.27	63	2.4		Picture6
8	down	Main structure	Lining cracks/longitudinal cracks		left sidewall	K	1867.5		0.4m from the bottom	0.21	84	1.9		Picture7
9	down	Main structure	Lining cracks/longitudinal cracks		left sidewall	K	1871		1.2m from the bottom	0.31	98	1.5		Picture8
10	down	Main structure	Lining cracks/longitudinal cracks		left sidewall	K	1928		0.6m from the bottom	0.28	73	2.4		Picture9
11	down	Main structure	Lining cracks/longitudinal cracks		left sidewall	K	1930.2		0.3m from the bottom	0.31	67	3.2		Picture10
12	down	Main structure	Lining cracks/longitudinal cracks		left sidewall	K	1931.5		0.8m from the bottom	0.25	72	1.5		Picture11
13	down	Main structure	Lining cracks/longitudinal cracks		left sidewall	K	1932.4		0.5m from the bottom	0.23	83	1.7		Picture12
14	down	Main structure	Lining cracks/longitudinal cracks		left sidewall	K	1935		0.0m from the bottom	0.3	71	2.8		Picture13
15	down	Main structure	Lining cracks/longitudinal cracks		left sidewall	K	1945		1.0m from the bottom	0.25	63	2.2		Picture14
16	down	Main structure	Lining cracks/longitudinal cracks		left sidewall	K	1945.5		2.0m from the bottom	0.23	68	2		Picture15
17	down	Main structure	Lining cracks/longitudinal cracks		left sidewall	K	1953.1		0.5m from the bottom	0.32	52	2.2		Picture16
18	down	Main structure	Lining cracks/longitudinal cracks		left sidewall	K	1958		0.5m from the bottom	0.35	100	4.2		Picture17
19	down	Main structure	Lining cracks/longitudinal cracks		left sidewall	K	1979.5		0.2m from the bottom	0.23	79	4.3		Picture18
20	down	Main structure	Lining cracks/longitudinal cracks		left sidewall	K	1981.2		0.7m from the bottom	0.31	72	3.5		Picture19
21	down	Main structure	Lining cracks/longitudinal cracks		left sidewall	K	1980		0.5m from the bottom	0.35	102	6.5		Picture20
22	down	Main structure	Lining cracks/longitudinal cracks		left sidewall	K	2006		0.7m from the bottom	0.25	64	2.1		Picture21
23	down	Main structure	Lining cracks/longitudinal cracks		left sidewall	K	2086.5		1.2m from the bottom	0.31	75	0.3		Picture22
24	down	Main structure	Lining cracks/longitudinal cracks		left sidewall	K	2178		0.7m from the bottom	0.43	82	2.6		Picture23
25	down	Main structure	Lining cracks/longitudinal cracks		left sidewall	K	2267		0.4m from the bottom	0.49	97	1.9		Picture24
26	down	Main structure	Lining cracks/longitudinal cracks		left sidewall	K	2276		0.0m from the bottom	0.3	88	3		Picture25
27	down	Main structure	Lining cracks/longitudinal cracks		left sidewall	K	2331.2		0.7m from the bottom	0.24	74	1.4		Picture26
28	upgoing	Main structure	Lining cracks/longitudinal cracks		right sidewall	K	1735.4		0.4m from the bottom	0.3	87	2.6		Picture27
29	upgoing	Main structure	Lining cracks/longitudinal cracks		right sidewall	K	1745		1.6m from the bottom	0.34	75	Reticulum cracks		Picture28
30	upgoing	Main structure	Lining cracks/longitudinal cracks		right sidewall	K	1791		1.0m from the bottom	0.26	84	1.9		Picture29
31	upgoing	Main structure	Lining cracks/longitudinal cracks		right sidewall	K	1792		1.2m from the bottom	0.34	75	1.7		Picture30
32	upgoing	Main structure	Lining cracks/longitudinal cracks		right sidewall	K	1861.4		0.7m from the bottom	0.3	86	2		Picture31
33	upgoing	Main structure	Lining cracks/longitudinal cracks		right sidewall	K	1928		1.4m from the bottom	0.37	79	2.2		Picture32
34	upgoing	Main structure	Lining cracks/longitudinal cracks		right sidewall	K	1931.6		0.5m from the bottom	0.34	90	2.3		Picture33
35	upgoing	Main structure	Lining cracks/longitudinal cracks		right sidewall	K	1946.5		0.4m from the bottom	0.23	45	3.5		Picture34

Fig. 9. Batch import template

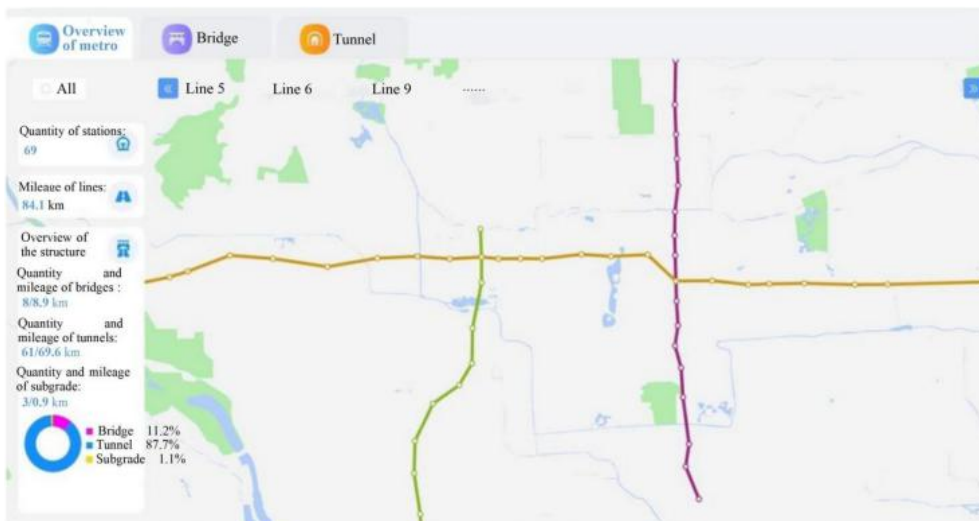


Fig. 10. Home page display



Fig. 11. Data visualization display

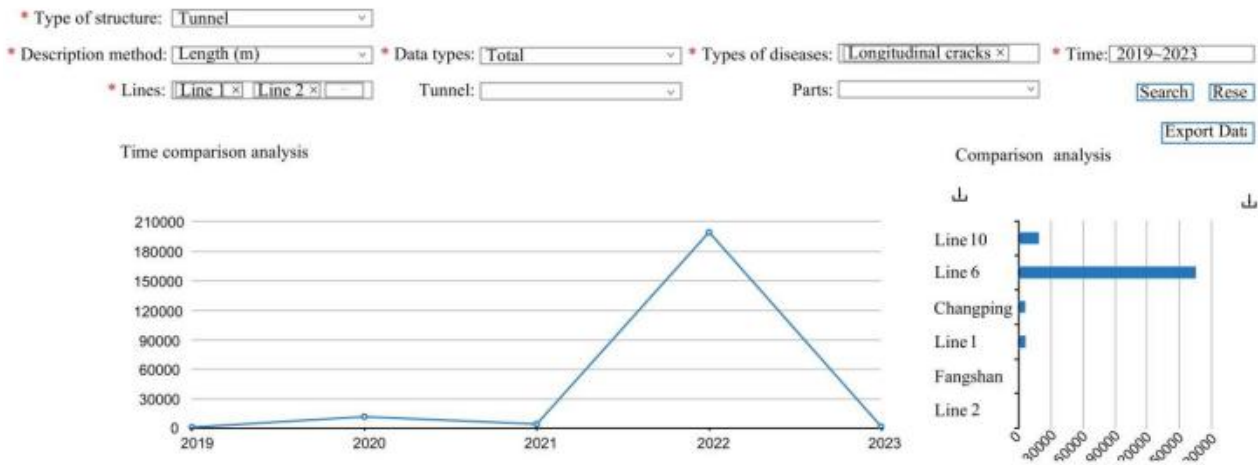


Fig. 12. Data chain analysis

query, site management, line management, structural management, monitoring engineering management, testing engineering management, safety assessment engineering management, and system management.

In summary, the platform for standardizing and visualizing monitoring and testing data for metro civil engineering facilities, addressed in this paper, has successfully implemented batch uploading, comprehensive management, and integrated analysis of multi-source data. By dividing system role permissions, it is possible to effectively satisfy the requirements of various roles, scenarios, and functions.

Conclusions

In order to meet the requirements for monitoring, testing, data asset management, automatic access, and intelligent analysis of metro civil engineering facilities, this paper designs and implements a third-party testing and monitoring data standardization and visualization platform for metro civil engineering facilities. The platform provides standardized batch data import, data classification storage, and data management and sharing functions. On this platform, standards for uploading third-party detection, monitoring data, and test data are established. This helps to solve the serious issue of data isolation between existing systems, establish a structured database, and effectively utilize multi-system data for comprehensive analysis.

The integration of detection and monitoring data has been achieved. Meanwhile, multi-source data fusion analysis and comparison across projects and intervals are realized in combination with massive standardized detection and monitoring data. This provides powerful data support for the whole life-cycle management of later facilities.

The platform has been in operation since 2022, and such information as testing and monitoring data, as well as basic information ledger from 2019 to 2022, has been imported. This confirms the feasibility of the platform.

Further research directions

- 1) Expand the scope of standardized data management and strengthen the processes for data standardization management, particularly focusing on data collection to ensure the integrity and effectiveness of the collected data.
- 2) Create a diversified and comprehensive data display page to enable such functions as structural detection cycle warning, auxiliary analysis of detection cost, disease tracking, and key information warning. Assist management personnel in visually viewing and quickly analyzing the health status of civil engineering facilities.
- 3) Study conventional-style parameterized modeling techniques for bridges and tunnels, and complete BIM modeling for the entire lines of bridges and tunnels, thereby providing a model foundation for the rich and comprehensive application of BIM visualization.

References

- Agrawal, D., Das, S., and Abbad, A. E. (2011). Big Data and cloud computing: current state and future opportunities. In: Ailamaki, A., Amer-Yahia, S., Pate, J., Risch, T., Senellart, P., and Stoyanovich, J. (eds.). *EDBT/ICDT '11: Proceedings of the 14th International Conference on Extending Database Technology*. New York: Association for Computing Machinery, pp. 530–533. DOI: 10.1145/1951365.1951432.
- Assunção, M. D., Calheiros, R. N., Bianchi, S., Netto, M. A. S., and Buyya, R. (2015). Big Data computing and clouds: trends and future direction. *Journal of Parallel and Distributed Computing*, Vols. 79–80, pp. 3–15. DOI: 10.1016/j.jpdc.2014.08.003.
- Beijing Bureau of Quality and Technical Supervision (2015). *State Standard of China. DB11/T 1167-2015. Technical regulations for structural inspection of urban rail transit facilities*. Beijing: Beijing Bureau of Quality and Technology Supervision, pp. 69.
- Beijing Bureau of Quality and Technical Supervision (2016). *State Standard of China. DB11/T 718-2016. Technical Specifications for Maintenance and Repair of Urban Rail Transit Facilities*. Beijing: Beijing Bureau of Quality and Technical Supervision, pp. 123.
- Beyer, M. A. and Laney, D. (2012). *The importance of 'Big Data': a definition*. Gartner Report G00235055. [online] Available at: <https://www.gartner.com/en/documents/2057415> [Date accessed April 01, 2024].
- Chen, Y., Alspaugh, S., and Katz, R. (2012). Interactive analytical processing in Big Data systems: a cross-industry study of MapReduce workloads. *Proceedings of the VLDB Endowment*, Vol. 5, Issue 12, pp. 1802–1813. DOI: 10.14778/2367502.2367519.
- Chen, C. L. P. and Zhang, C.-Y. (2014). Data-intensive applications, challenges, techniques and technologies: a survey on Big Data. *Information Sciences*, Vol. 275, pp. 314–347. DOI: 10.1016/j.ins.2014.01.015.
- Demirkan, H. and Delen, D. (2013). Leveraging the capabilities of service-oriented decision support systems: Putting analytics and big data in cloud. *Decision Support Systems*, Vol. 55, Issue 1, pp. 412–421. DOI: 10.1016/j.dss.2012.05.048.
- Ding, L.-Y. and Guo, S.-Y. (2015). Study on Big Data-based behavior modification in metro construction. *Frontiers of Engineering Management*, Vol. 2, Issue 2, pp. 131–136. DOI: 10.15302/J-FEM-2015037.
- Guo, S. Y., Ding, L. Y., Luo, H. B., and Jiang, X. Y. (2016). A Big-Data-based platform of workers' behavior: observations from the field. *Accident Analysis & Prevention*, Vol. 93, pp. 299–309. DOI: 10.1016/j.aap.2015.09.024.
- Jamshidi, A., Faghieh-Roohi, S., Hajizadeh, S., Nunez, A., Babuska, R., Dollevoet, R., Li, Z., and De Schutter, B. (2017). A Big Data analysis approach for rail failure risk assessment. *Risk Analysis*, Vol. 37, No. 8, pp. 1495–1507. DOI: 10.1111/risa.12836.
- Khribi, M. K., Jemni, M., and Nasraoui, O. (2009). Automatic recommendations for e-learning personalization based on web usage mining techniques and information retrieval. *Journal of Educational Technology & Society*, Vol. 12, No. 4, pp. 30–42.
- Li, Q. (2020). Research and application of urban rail transit inspection data system based on cloud platform. *Modern Urban Transit*, Vol. 2, pp. 78–83.
- Luo, Q., Shui, B., and Ouyang Y.-P. (2019). Application of BIM technology in urban rail transit. *Modern Urban Transit*, Vol. 12, pp. 83–86.
- Lv, Y., Duan, Y., Kang, W., Li, Z., and Wang, F.-Y. (2015). Traffic flow prediction with Big Data: a deep learning approach. *IEEE Transactions on Intelligent Transportation Systems*, Vol. 16, Issue 2, pp. 865–873. DOI: 10.1109/TITS.2014.2345663.
- Mayer-Schönberger, V. and Cukier, K. (2013). *Big Data: a revolution that will transform how we live, work, and think*. New York: Houghton Mifflin Harcourt, 242 p.
- Peng, K., Yuan, C., and Xu, W. (2017). Perspectives of Big Data analysis in urban railway planning: Shenzhen metro case study. In: Gao, X., Du, H., Han, M. (eds.). *Combinatorial Optimization and Applications. COCOA 2017. Lecture Notes in Computer Science*, Vol. 10627. Cham: Springer, pp. 386–400. DOI: 10.1007/978-3-319-71150-8_32.
- Standardization Administration of the People's Republic of China (2013). *National Standard of the People's Republic of China. GB 50911-2013. Code for monitoring measurement of urban rail transit engineering*. Beijing: Standardization Administration of the People's Republic of China, pp. 179.
- Standardization Administration of the People's Republic of China (2020). *National Standard of the People's Republic of China. GB/T 39559.2-2020. Specifications for operational monitoring of urban rail transit facilities - Part 2: Bridge*. Beijing: Standardization Administration of the People's Republic of China, pp. 42.
- Tao, K., Guo, Q., and Dai, C.-P. (2021). Design and implementation of railway infrastructure inspection and monitoring data management and analysis service platform based on Big Data. *Railway Engineering*, Vol. 61, Issue 9, pp. 147–150. DOI: 10.3969/j.issn.1003-1995.2021.09.31.
- Tao, K., Yang, W., Du, Z., and Liu, G. (2019). Integrated storage for track inspection data and data quality evaluation. *Railway Engineering*, Vol. 59, Issue 9, pp. 116–120. DOI: 10.3969/j.issn.1003-1995.2019.09.28.

Vitri, G. and Herman, H. (2019). Infrastructure maintenance system for community development projects to improve the quality of infrastructure services in West Sumatra Province. *IOP Conference Series: Materials Science and Engineering*, Vol. 602, 012101. DOI: 10.1088/1757-899X/602/1/012101.

Wu, J.-Y., Ping, L.-D., Ge, X.-P., Wang, Y., and Fu, J.-Q. (2010). Cloud storage as the infrastructure of cloud computing. In: *Proceedings of the 2010 International Conference on Intelligent Computing and Cognitive Informatics*. Washington: IEEE Computer Society, pp. 380–383. DOI: 10.1109/ICICCI.2010.119.

Yang, L.-L. (2021). Analysis on application and prospect of BIM technology in intelligent operation and maintenance of railway infrastructure. *Modern Urban Transit*, Vol. 6, pp. 96–102.

Zach, J. and Reiser, H. P. (2015). Live Cloud Inspector: towards integrated IaaS forensics in the cloud. In: Bessani, A. and Bouchenak, S. (eds.). *Distributed Applications and Interoperable Systems. DAIS 2015. Lecture Notes in Computer Science*, Vol. 9038. Cham: Springer, pp. 207–220. DOI: 10.1007/978-3-319-19129-4_17.

ИССЛЕДОВАНИЕ ПЛАТФОРМЫ СТАНДАРТИЗАЦИИ И ВИЗУАЛИЗАЦИИ ДАННЫХ МОНИТОРИНГА И ИСПЫТАНИЙ ГРАЖДАНСКИХ ОБЪЕКТОВ МЕТРОПОЛИТЕНА НА ОСНОВЕ БОЛЬШИХ ДАННЫХ

Цяофэн Шэнь^{1*}, Чэнь Шэнь¹, Сюнь Лю¹, Юань Цзя², Цзя Цянь³

¹ Beijing Subway Construction Facilities Maintenance Co., Ltd., Пекин, Китай

² Beijing Jiutongqu Testing Technology Co., Ltd., Пекин, Китай

³ Школа транспорта, Юго-восточный университет, Нанкин, Китай

*E-mail: 18813094515@163.com

Аннотация

Введение: на межпроектном и межрегиональном уровнях с целью получения надежных данных для управления гражданскими объектами метрополитена на протяжении всего жизненного цикла проведены анализ и сравнение данных из нескольких источников с учетом обширных стандартизированных данных обнаружения и мониторинга.

Цель исследования — интегрировать данные обнаружения и мониторинга в отношении мостов и тоннелей метрополитена и решить проблему значительной изоляции данных в существующих системах и различных блоках. На основе больших данных и технологии Интернета вещей в данной работе исследуется стандартизированный формат загрузки, хранения, обработки, обмена и других видов управления данными обнаружения и мониторинга в отношении мостов и тоннелей метрополитена. Кроме того, разработана платформа стандартизации и визуализации сторонних данных для мостов и тоннелей, обеспечивающая интеграцию данных обнаружения и мониторинга. В ходе исследования использовались следующие **методы:** теоретический анализ и разработка системы ПО. **Результаты:** практическая и реализуемость платформы были проверены на практике.

Ключевые слова: гражданские объекты метрополитена, платформа больших данных, обнаружение и мониторинг, стандартизация данных, комплексный анализ.

EXPERIMENTAL INVESTIGATION ON THE SHEAR RESISTANCE OF I-SHAPED PERFORATED CONNECTORS IN COMPOSITE BEAMS

Farid Boursas*, Rafik Boufarh, Abderrahmani Sifeddine

Laboratory of Applied Civil Engineering (LGCA), Department of Civil Engineering, Echahid Cheikh Larbi Tebessi University, Algeria

*Corresponding author's email: farid.boursas@univ-tebessa.dz

Abstract

Introduction: Steel-concrete composite girders have been widely used in bridges, with the stability of the interface being crucial. Shear connectors and reinforced concrete slabs play a key role as interfaces. Understanding the interaction between the composite beam and slab is essential for predicting the overall system response. It is necessary to optimize the connection between steel beams and reinforced concrete slabs in steel-concrete composite girders and facilitate their assembly and installation on-site, emphasizing their pivotal role in upholding the structural integrity of composite systems. The **purpose of the study** was to conduct an experimental investigation and a numerical simulation using the finite element method. During the study, the following **methods** were used: examining the behavior of IPE and IPN perforated shear connectors using push-out tests. The main objective was to analyze how the I-shaped perforated connector, concrete slab, steel beam, and rebar affect the measured slip between the steel beam and concrete slab. To achieve that, specimens with IPE80 or IPN80 shear connectors having circular or long cut holes containing 8 mm or 6 mm diameter steel bars were used to enhance the connector's resistance against uplift forces. The test setup follows Eurocode 4 guidelines, focusing on hole shape and anti-lift rebar diameter parameters. The predominant failure modes were mainly dictated by the crushing of the concrete slab. As a **result**, it was found that the hole geometry of IPE and IPN perforated shear connectors significantly impacts shear load capacity and ductility. The long cut hole shape in IPE and IPN perforated shear connectors exhibits superior ultimate load capacity but less interfacial slip compared to the circular hole. The IPE and IPN perforated shear connectors demonstrated satisfactory ductility for all tested hole shapes, and the 3D finite element models are consistent with the test results.

Keywords: composite beams, I-shaped perforated connectors, load-slip behavior, push-out test, ductility, finite element method.

Introduction

In the pursuit of practical solutions for steel-concrete connection challenges in composite constructions, various types of connectors have been explored to optimize connector quantity, strength, cost effectiveness, and ease of on-site assembly. While only a handful of types of connectors have been endorsed by Eurocode due to their reliability and ease of implementation for most structures (Maquoi et al., 2010), limitations in shear strength and fatigue under cyclic loads in composite bridges have led to the exploration of alternative connectors.

Several alternatives, such as welded angles with anti-lift rebars and perforated plates, have been proposed to address these concerns (Bujnak, 2007). Perforated plates were developed in Germany for the construction of the composite bridge of Caroni in Venezuela (Jarek, 2004). U- and I-shaped connectors were developed by Viest et al. (1951). In a previous work by Farid and Boutagougga (2021), I-shaped connectors showed promise in their ability to withstand shear forces and prevent vertical

separation, as illustrated in Fig. 1. When oriented optimally, the I-shape demonstrated significantly higher shear strength than other orientations but exhibited minimal resistance to vertical separation.

This paper focuses on using perforated I-connectors with anti-lift rebars to enhance vertical separation resistance, improve the connector's ability to withstand shear forces, and prevent vertical separation between the steel beam and concrete slab. Unlike the U-connector, the perforated I-connector displays consistent behavior in both directions. It offers manufacturing ease through transverse cutting of IPN and IPE profiles, similar to the welding process for U-connectors.

Perforated shear connectors, known for their high bearing capacity and ductility, are increasingly favored in composite steel-concrete structures, especially when other connectors lack sufficient strength (Liu et al., 2021). Vianna et al. (2008) conducted an in-depth examination of perforated T-connectors, analyzing their performance in relation to concrete slab thickness, compressive



Fig. 1. IPE shear connectors studied in different orientations (Farid and Boutagouga, 2021)

strength, connector geometry, placement, and hole configuration. They also compared the outcomes of push-out tests with an analytical model proposed by different researchers in a comparative study between perforated plates and perforated T-connectors (Vianna et al., 2009). Another parametric study on perforated connectors demonstrated that increasing the number of holes in the connector increases its resistance. For each additional hole, there was an average increase in resistance of approximately 5 %. It was deduced that the concrete cylinders formed through the holes do not play a dominant role in strength compared to other factors such as plate bearing or slab reinforcement.

However, it is important to note that having at least one hole is crucial to ensure proper behavior and prevent undesired uplift. The study also revealed that the uplift remained controlled and consistent in magnitude for all perforated connectors (Cândido-Martins et al., 2010). Ahn et al. (2010) introduced a modified shear strength equation, considering perforated plates and rebar spacing based on push-out tests. Costa-Neves et al. (2013) explored eight new specimens featuring innovative geometries such as the I-Perfobond and the 2T-Perfobond, alongside an analytical model that accounted for connector geometry and reinforcing bars through holes. This included a comparison of experimental results with analytical models for perforated I- and T-shaped shear connectors.

A model developed by Su et al. (2014) overlooked the effects of specimen size and friction on the structural performance of the connector with a perforated plate. An analysis of the failure mechanism of perfobond rib shear connectors revealed a consistent occurrence of brittle failure

in these connectors. Zheng et al. (2016) conducted a study with 21 push-out tests using circular and oblique hole perforated connectors, comparing these results against 10 shear resistance equations from the literature. Allahyari et al. (2018) used 90 literature records to develop a Bayesian neural network model that expresses the shear strength of perforated connectors with bars. Kim et al. (2018) examined the behavior of perforated Y-shaped shear connectors with double-row bars using push-out tests. Their investigation focused on exploring connector spacing, quantity, and three variations of single and double-row specimens. Zhao et al. (2018) conducted an experimental study involving 18 deeply anchored PBL shear connectors within reinforced concrete slabs. The findings highlighted that the hole diameter in the perforated steel plate, the diameter of reinforcing bars, and the transverse reinforcement ratio significantly influenced the bearing capacity. To address the challenges of installing reinforcements within circularly perforated connectors, Wang et al. (2018) proposed creating vertical sections in perforated plates to facilitate implementation and further study the behavior of this connector.

Methods

Composite constructions with steel and concrete have proven to outperform any other type of construction, particularly for main structures such as commercial buildings, residential buildings, and many bridges. They offer greater stiffness and strength to steel, as well as improved ductility.

This study explores the behavior of IPE and IPN perforated steel shear connectors, specifically those perforated with either circular or long cut holes, as depicted in Fig. 2. Experimental tests were conducted to analyze and compare these connector

types with regard to their shear strength, ductility, and failure modes.

Specimen preparation

The composite beams under investigation consisted of a HEB160 steel beam connected to a reinforced concrete slab with dimensions of $36 \times 32 \times 12 \text{ cm}^3$. The slab was reinforced with $4\Phi 8$ reinforcements in two directions, as illustrated in Fig. 3. The connection between the steel beam and the concrete slab involves either IPE80 or IPN80 profile perforated shear connectors placed within circular and long cut holes with diameters of 6 and 8 mm, respectively, passing through the perforations.

All selected specimens adhered to the standard dimensions outlined in Eurocode 4 (2006) specifications (Fig. 4). This study used conventional concrete for the concrete slab material.

Material properties

Steel

Steel coupons were cut from the IPE80 and IPN80 webs and underwent standard coupon tensile testing to establish the stress-strain curve of the connectors. The specimen dimensions aligned with those typical for tensile tests on metallic materials (Aegerter et al., 2011). From these tests, crucial material properties such as yield strength and ultimate tensile stress of the connectors were determined and are detailed in Table 1.

Table 1. Mechanical properties of the connector

Type	f_y (MPa)	f_u (MPa)
IPE80	238	358
IPN80	247	385



Fig. 2. IPE and IPN perforated shear connectors under study



Fig. 3. Push-out specimen preparation

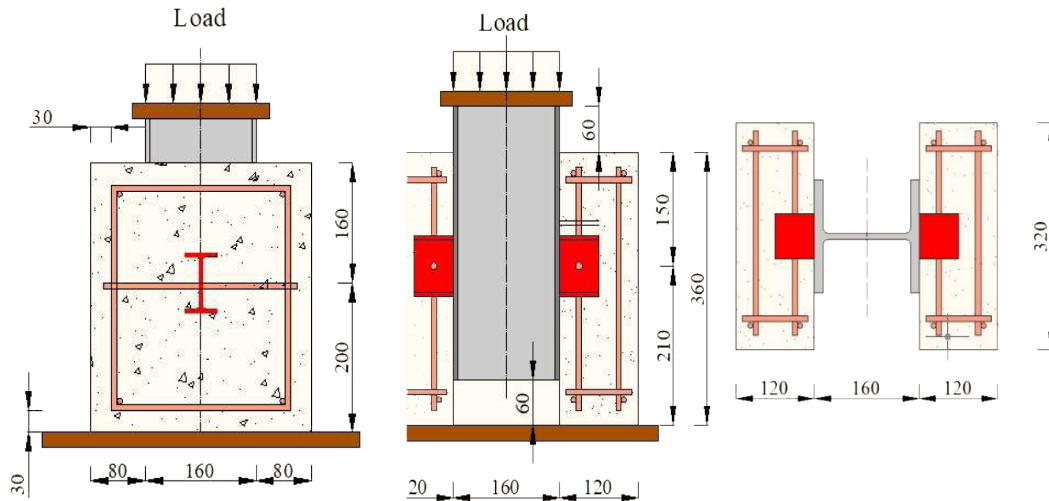


Fig. 4. Specimen dimensions (mm)

Concrete

The concrete mixture proportions for the slab were determined using the Dreux-Gorisse method (Dreux and Festa, 2007). All push-out specimen slabs were horizontally cast following Eurocode 4 standards, ensuring the elimination of friction at the steel-concrete interface by oiling the HEB flanges before casting the slab.

During the concrete casting process, three cylinders of concrete measuring 160 mm in diameter and 320 mm in length were formed from the same concrete mixture. These cylinders underwent compressive strength testing on the same day as the push-out tests were performed. The results of the tests are detailed in Table 2.

Table 2. Compressive strength of concrete

F_{c28} (MPa)	Average F_{c28} (MPa)
30.453	30.454
30.289	
29.866	
31.208	

Test setup and loading procedure

A concentrated monotonic load was applied to the top section of the HEB160 in the push-out specimens, as illustrated in Fig. 5. This load was applied using a calibrated hydraulic jack connected to an electric pump with a capacity of 500 kN. To measure the relative displacement between the HEB160 and the concrete slab, a linear variable differential transformer (LVDT) linked to a data acquisition system was placed at the top center of the HEB160. Two rigid steel plates, each 20 mm thick, were used to distribute the load uniformly. One was placed between the HEB160 and the hydraulic jack to spread the load across the entire HEB160 cross-section, while the other was positioned beneath

the concrete slabs to provide a firm base. The test procedure adhered to Eurocode 4 (2006) standards. The load was initially applied incrementally in steps of 10 kN, ranging from 0 to 80 kN (equivalent to 40 % of the expected failure load), and then reduced to 10 kN (5 % of the expected failure load). Following this, a loading cycle between 10 and 80 kN was repeated 25 times to eliminate any inconsistencies in the test setup. The load was then continuously increased until failure occurred.

Results

The push-out tests investigated how IPE and IPN perforated shear connectors behave in composite girders. The main goal of this study was to analyze the load-slip behavior, ultimate shear capacity, and failure modes of the I-shaped perforated connectors.

I-shaped perforated connectors with a circular hole

The behavior of IPE and IPN perforated shear connectors with circular holes was examined during the initial experimental tests. The specimens under study were labeled as follows: IPE6C and IPN6C, denoting those with a 6 mm diameter of anti-lift rebar, while IPE8C and IPN8C represented specimens with an 8 mm diameter of anti-lift rebar (Fig. 5). Additionally, Fig. 6 illustrates the load-slip characteristics of these tested IPE and IPN perforated connectors featuring circular holes.

The findings indicate that IPE and IPN perforated connectors exhibit similar behavior, as illustrated in Figs. 6 and 7. Notably, IPE perforated connectors demonstrate marginally higher strength and ductility than their IPN counterparts. All specimens displayed remarkable ductility, meeting the 6 mm slip ductility limit. Failures occurred at slip measurements of 13.12 mm and 15.80 mm for IPE6C and IPE8C, and 12.98 mm and 12.58 mm for IPN6C and IPN8C, respectively. The diameter of the anti-lift rebar significantly impacts shear resistance, as evidenced



Fig. 5. Testing procedure

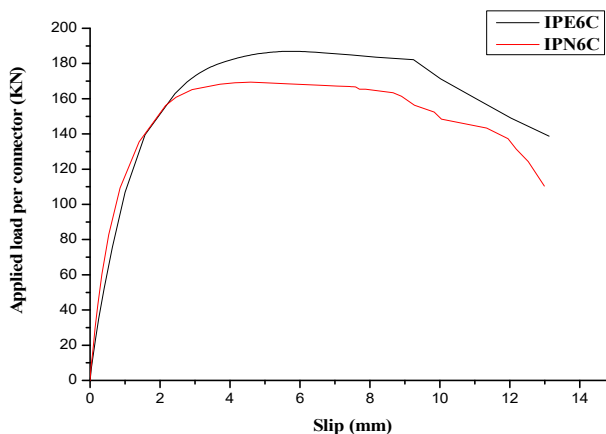


Fig. 6. Load-slip curves for IPE80 and IPN80 connectors with 6 mm rebar and a circular hole

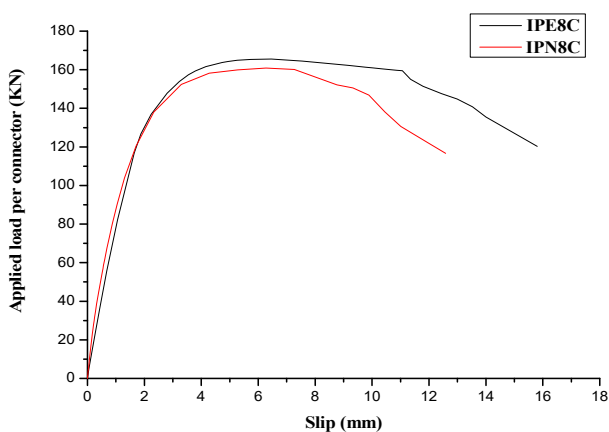


Fig. 7. Load-slip curves for IPE80 and IPN80 connectors with 8 mm rebar and a circular hole

by a decrease in load capacity with increasing rebar diameter in perforated connectors. Specifically, IPE6C and IPE8C failed at maximum loads of 186.92 kN and 165.52 kN per shear connector, while IPN6C and IPN8C failed at 169.39 kN and 160.90 kN per shear connector, respectively. Initial cracks appeared on the outer surfaces of the concrete slabs at a load of 115 kN per shear connector.

The initial cracks did not propagate deeply within the concrete slabs due to a 6 mm diameter anti-lift rebar. In IPE6C and IPN6C specimens, the anti-lift rebar effectively delayed the failure of the concrete slab. However, using an 8 mm diameter anti-lift rebar led to brittle concrete failure, accelerating crack propagation. In all cases of perforated connectors with a circular hole, the failure mode stemmed from concrete cracking and crushing, as seen in Fig. 8.

I-shaped perforated connectors with a long cut hole

Subsequent experimental tests examined the behavior of IPE and IPN perforated shear connectors featuring a long cut hole. This investigation explored how the hole shape impacts shear capacity, failure modes, and load-slip behavior. The specimens under scrutiny were labeled as follows: IPE6N and IPN6N, denoting those with a 6 mm diameter of anti-lift rebar, while IPE8N and IPN8N represented specimens with an 8 mm diameter of anti-lift rebar.

As shown in Figs. 9 and 10, IPE6N and IPE8N connectors exhibited ultimate shear capacities of 192.65 kN and 170.70 kN per connector, with ultimate slip capacities of 13.26 mm and 16.72 mm, respectively. Conversely, for IPN6N and IPN8N, the ultimate shear capacities were 172.30 kN and 168.89 kN per connector, with ultimate slip capacities of 12.68 mm and 10.81 mm, respectively. All the examined specimens notably exhibited reasonably robust ductile behavior.

The failure mode in all specimens of the perforated connectors with a long cut hole was due to concrete cracking and crushing. The early cracks observed on the surface of the concrete slabs started around the connector located in the middle of the slab at a load of approx. 155 kN per connector. The cracks are due to perforated rebar and the strength of the concrete slab, as shown in Fig. 11.

Analytical bearing capacity of I-shaped perforated connectors

Several analytical models have been proposed to estimate the bearing capacity of perforated connectors. Zheng et al. (2016) classified the equations proposed in the literature into three categories: the first is based on the resistance of the steel bar passed through the hole, the second is based on the strength of the reinforced concrete slab, and the third is based on the shape and distribution of the holes. Leonhardt et al. (1989) proposed the first analytical model with a simple



Fig. 8. Failure of IPE6C, IPE8C, IPN6C and IPN8C specimens

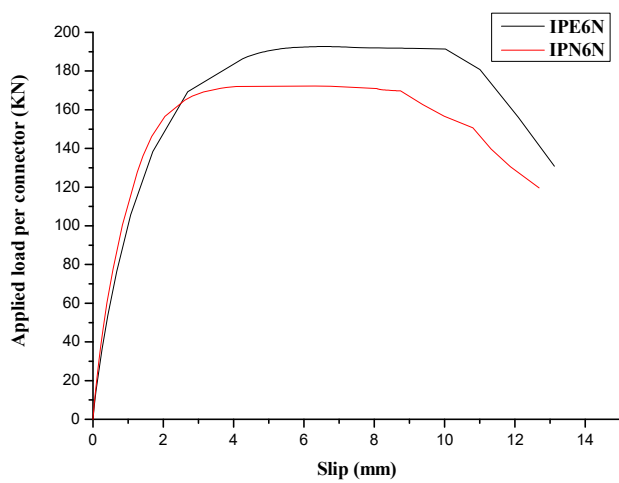


Fig. 9. Load-slip curves for IPE80 and IPN80 connectors with 6 mm rebar and a long cut hole

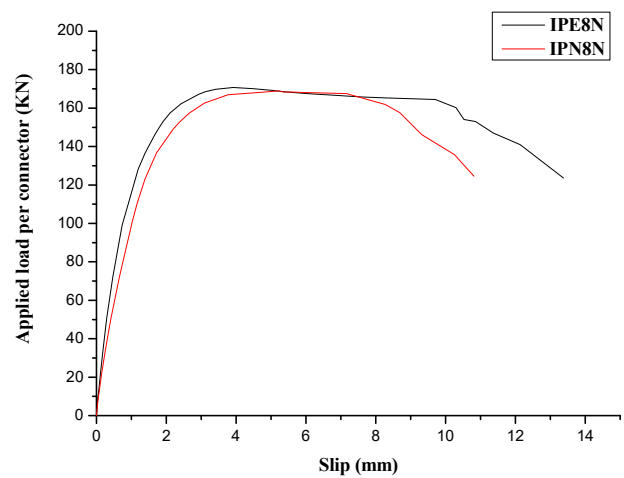


Fig. 10. Load-slip curves for IPE80 and IPN80 connectors with 8 mm rebar and a long cut hole



Fig. 11. Load-slip curve for IPE80 and IPN80 connectors with 8 mm rebar and a long cut hole

equation that only considers the resistance of the concrete slab, as shown in Table 3. Oguejiofor and Hosain (1994) proposed a more elaborate equation that considered the slab and connector resistances by considering the concrete strength and section, as well as the steel connector strength and section.

Medberry and Shahrooz (2002) adjusted the coefficients of the equation proposed by Oguejiofor and Hosain (1994). They considered the details of the geometry of the connector, such as the height and width of the perforated connectors. Verissimo et al. (2006) derived a modified equation to evaluate

the shear capacity of perforated connectors, based on the work of Oguejiofor and Hosain (1994). This modified equation was proposed based on the results of push-out tests and statistical analysis. Al-Darzi et al. (2007) proposed an analytical model that estimates the shear capacity of the perforated connector based on the results of a parametric study they conducted using a finite element-based model of push-out tests.

Additionally, the equation for estimating the bearing capacity must consider not only the steel bar passing through the cut hole, but also the shape of the push-out specimen, the geometry of the cut connector, and the properties of the materials used (Ahn et al., 2010). Zhao and Liu (2012) proposed an equation that considers the anchoring of the concrete in the hole, the contribution of the reinforcement passing through the hole, and the effect of the confinement on the strength of the concrete. Zheng et al. (2016) proposed a model to estimate the shear capacity of circular and long-cut hole perforated connectors. To adapt the model to different hole geometries, they proposed replacing the d^2 and d_s^2

variables in Eq. 7 with $4A/\pi$ and $4A_s/\pi$, respectively, as shown in Table 3.

An estimate of the load-bearing capacity of IPE80 and IPN80 perforated shear connectors was made based on the analytical models proposed in the literature. The obtained results are listed in Table 4.

As shown in Table 4, the shear capacity of perforated connectors obtained from the analytical models provided in the literature is very dispersed and cannot effectively predict the shear capacity of IPE and IPN perforated connectors. The closest models are those by Leonhardt and Verissimo, as shown in Table 5. Based on analytical equations analysis, none of the equations account for all parameters affecting shear strength simultaneously. New equations must be developed to consider the geometry and resistance of the concrete slab, as well as the transverse reinforcement. This should also include all dimensions of the perforated plate, such as length, height, and thickness, along with the mechanical characteristics of the material used. Finally, the area of the perforated section and the

Table 3. Analytical models for the bearing capacity of perforated connectors

Authors	Equations
Leonhardt et al. (1989)	$V_u = 2,23 A f_c$ (1)
Oguejiofor and Hosain (1994)	$V_u = 4,5 h_{sc} t_{sc} f_c + 0,91 A_{tr} f_y + 3,31 n d^2 \sqrt{f_c}$ (2)
Medberry and Shahrooz (2002)	$V_u = 1,66 n A \sqrt{f_c} + 0,9 A_{tr} f_y + 0,747 b h_{ecs} \sqrt{f_c} + 0,413 b_f L_c$ (3)
Verissimo et al. (2006)	$V_u = 31,85 \cdot 10^6 \left(\frac{A_{tr}}{A_{cc}} \right) + 0,16 A_{cc} \sqrt{f_c} + 4,04 \left(\frac{h}{b} \right) h t f_c + 2,37 n d^2 \sqrt{f_c}$ (4)
Al-Darzi et al. (2007)	$V_u = 2,53 \cdot 10^{-10} A \sqrt{f_c} - 7,59 \cdot 10^{-10} A_{tr} f_y + 7,62 \cdot 10^{-4} h t f_c + 255,310$ (5)
Ahn et al. (2010)	$V_u = 3,14 h t f_c + 1,21 A_{tr} f_y + 2,98 n d^2 \sqrt{f_c}$ (6)
Zhao and Liu (2012)	$V_u = 1,38 \left(d^2 - d_s^2 \right) f_c + 1,24 d_s^2 f_y$ (7)
Zheng et al. (2016)	$V_u = 1,76 \left(3,8 \left(\frac{A_s}{A} \right)^{\frac{2}{3}} (A - A_s) f_c + 1,58 A_s f_y \right)$ (8)

Table 4. Analytical models for the bearing capacity of perforated connectors

Hole shape	Specimens	Analytical shear load capacity (kN)							
		1	2	3	4	5	6	7	8
Circular	IPE6C	195.89	114.01	223.84	174.94	259.76	137.57	241.26	257.26
	IPN6C	166.54	114.57	223.74	178.32	259.85	137.96	241.26	257.26
	IPE8C	195.89	114.01	223.84	174.94	259.76	137.57	406.96	424.94
	IPN8C	166.54	114.57	223.74	178.32	259.85	137.96	406.96	424.94
Long cut	IPE6N	195.89	121.87	225.61	180.57	262.05	144.64	389.45	295.89
	IPN6N	166.54	122.42	225.51	183.94	262.14	145.03	389.45	295.89
	IPE8N	195.89	121.87	225.61	180.57	262.05	144.64	517.14	494.29
	IPN8N	166.54	122.42	225.51	183.94	262.14	145.03	517.14	494.29

Table 5. Comparison between the calculated shear resistance and experimental results of IPE and IPN perforated connectors

Hole shape	Specimens	Ultimate shear load using the equations (kN)				
		Leonhardt et al. (1987)	Exp/Eq	Verissimo et al. (2006)	Exp/Eq	Experimental ultimate shear load
Circular	IPE6C	195.89	0.95	174.94	1.07	186.92
	IPN6C	166.54	1.02	178.32	0.95	169.39
	IPE8C	195.89	0.84	174.94	0.95	165.52
	IPN8C	166.54	0.97	178.32	0.90	160.90
Long cut	IPE6N	195.89	0.98	180.57	1.07	192.65
	IPN6N	166.54	1.03	183.94	0.94	172.30
	IPE8N	195.89	0.87	180.57	0.95	170.70
	IPN8N	166.54	1.01	183.94	0.92	168.89

dimensions and resistance of the rebar passing through the holes should be considered.

Numerical modeling of push-out tests

To verify the experimental findings, a 3D finite element model for the IPE and IPN perforated shear connectors in push-out tests was developed using ABAQUS software (Fig. 12). Due to the symmetry, only half of the push-out test specimens was modeled. The three-dimensional C3D8R eight-node solid brick elements with reduced integration were used to mesh the concrete slab, the steel beam, the IPE80 and IPN80 perforated shear connectors, and the anti-lift rebar. The T3D2 two-node mesh element was used for rebar. The advantage of using a truss element is that the perfect bond can easily be defined by embedding the steel bars in a host region, such as a concrete slab in our case. The rigid base was modeled using the R3D4 discrete rigid element.

Figs. 13–14 depicts the non-linear stress-strain characteristics of concrete and I-connectors under compression and tension. The Concrete Damage Plasticity model from a material library (Barbero, 2023) was employed. The material dilation angle was set to 31, and an eccentricity value of 0.1 was used. Additionally, a ratio of 1.16 between biaxial compressive strength and uniaxial compressive strength was adopted, while the tensile-to-compressive meridian ratio was established as 0.667.

The contact pair method defines the “surface-to-surface” contact between the concrete slab, IPE80 and IPN80 perforated shear connectors, and rebar. In experimental push-out tests, the surface of the rigid base in contact with the concrete slab is generally greased to reduce friction. In our finite element model, frictionless contact interaction was

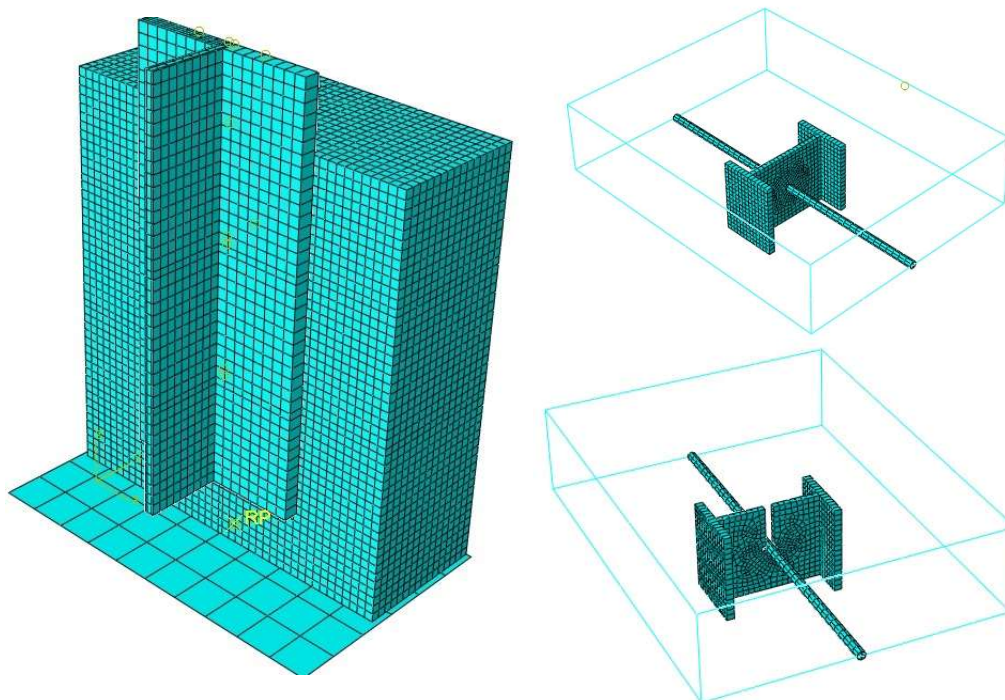


Fig. 12. Finite element mesh of the specimen

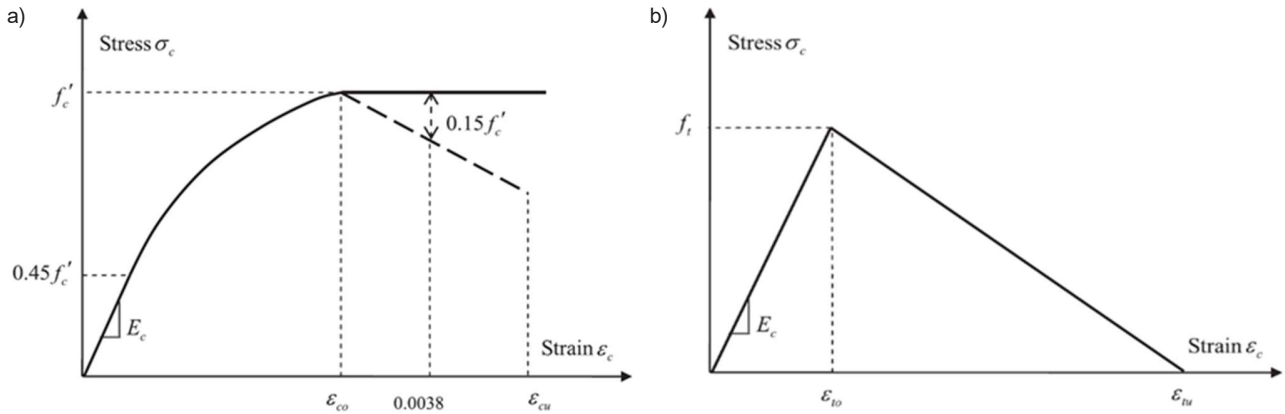


Fig. 13. Stress-strain relationship for concrete according to Eurocode 2 (1992): (a) compression, (b) tension

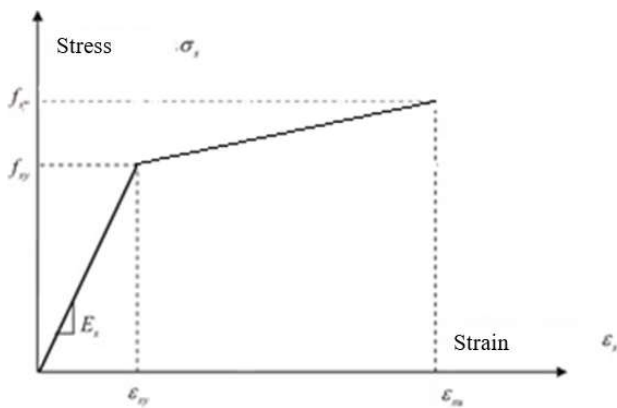


Fig. 14. Stress-strain relationship for I-connectors and reinforcement steel according to Eurocode 3 (1993)

applied to the surfaces of the rigid base and concrete slab. A tangential interaction was used for the interface between the I-shaped connector and the reinforced concrete slab, with a coefficient of friction set at 0.20. Reinforcing bars were located inside the concrete slab, as shown in Fig. 15. Integrated stress (embedded constraint) was applied to the rebar and slab.

The degrees of freedom of the rigid base reference node are all constrained. In this analysis, an imposed displacement is applied to the lower surface of the IPE80 and IPN80 perforated shear connectors, as shown in Fig. 16.

The numerical results obtained were compared with the results of the experimental tests.

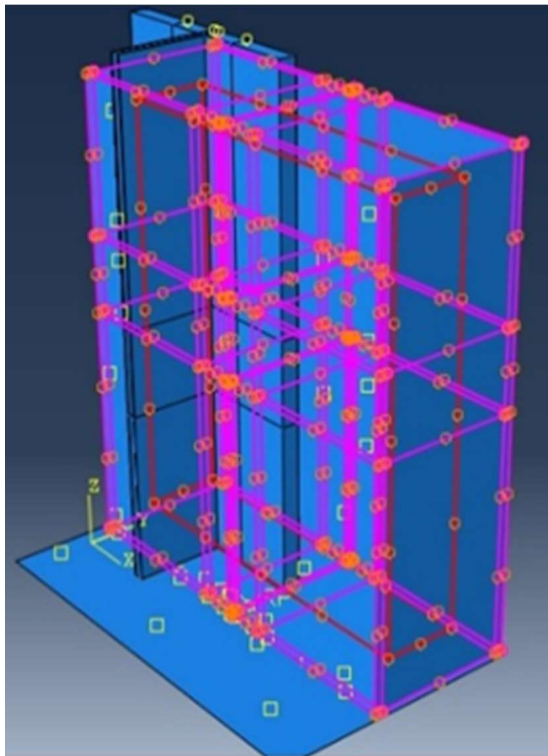


Fig. 15. Interaction and constraint conditions of the specimen

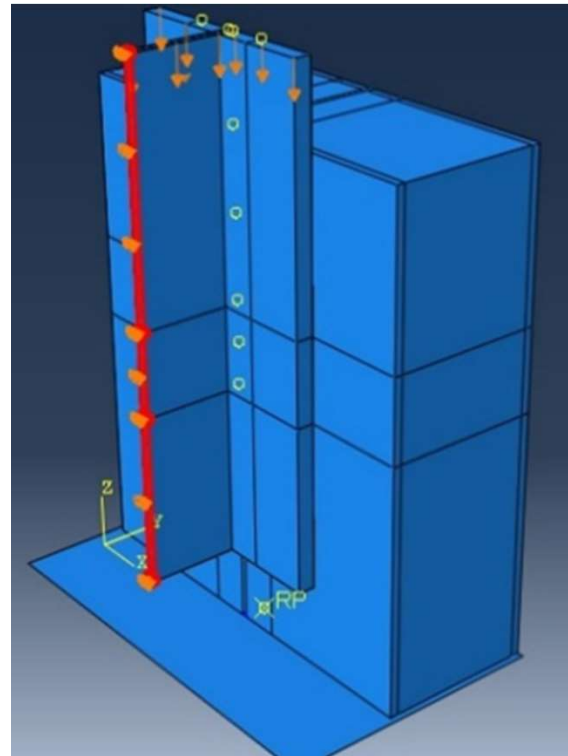


Fig. 16. Loading of the specimen

The comparison in the figures shows that the 3D finite element model established during this study can effectively predict the push-out strength and load-slip curve for push-out tests with perforated IPE80 and IPN80 connectors.

Figs. 17-20 compare the load-slip curves of the specimens with IPE and IPN perforated shear connectors obtained from the experiments with those

predicted by the proposed finite element analysis. The results show good agreement between the experimental data and the finite element analysis. However, after reaching the ultimate load, the numerical curves diverge from the experimental curves. This discrepancy is attributed to differences in concrete mix standards across countries and the concrete material modeling used in the finite element analysis.

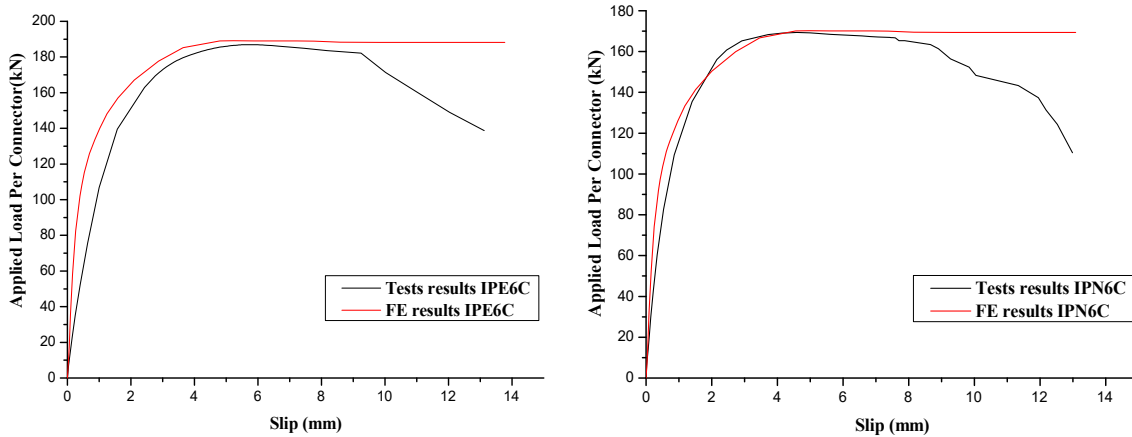


Fig. 17. Comparison of test and FE results for IPE80 and IPN80 connectors with 6 mm rebar and a circular hole

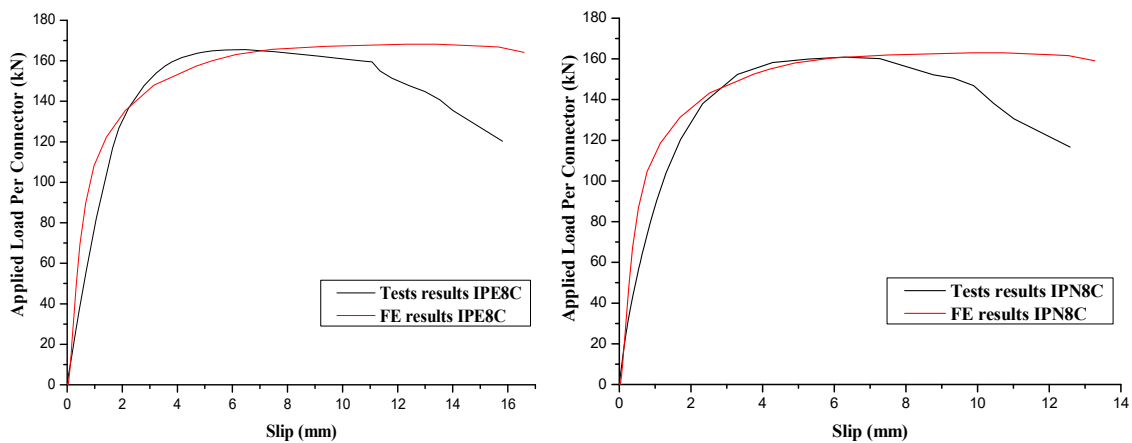


Fig. 18. Comparison of test and FE results for IPE80 and IPN80 connectors with 8 mm rebar and a circular hole

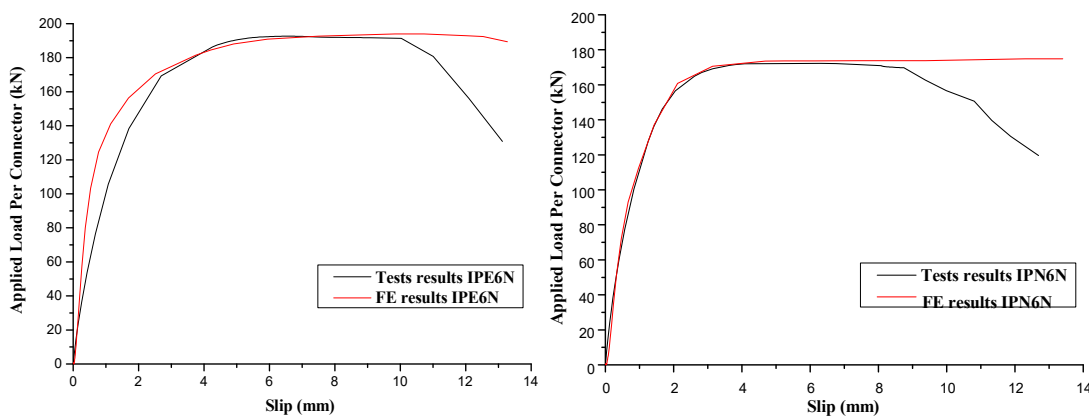


Fig. 19. Comparison of test and FE results for IPE80 and IPN80 connectors with 6 mm rebar and long cut hole

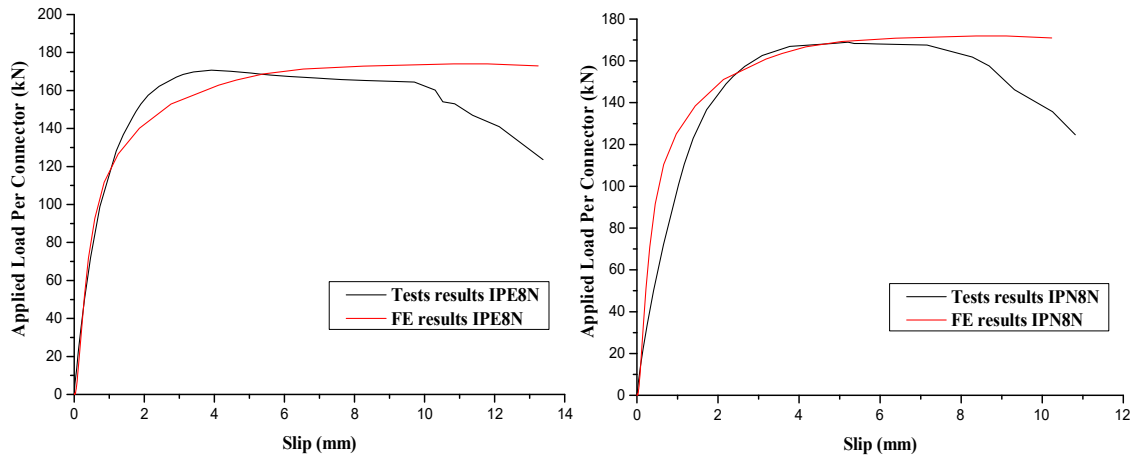


Fig. 20. Comparison of test and FE results for IPE80 and IPN80 connectors with 8 mm rebar and long cut hole

Conclusions

Eight push-out tests were conducted to examine the shear strength, ductility, and stiffness of IPE and IPN perforated shear connections in composite slabs. Based on the experimental results, several conclusions can be drawn:

- The geometry of the holes in IPE and IPN perforated shear connectors significantly impacts the shear load capacity and ductility.
- The long cut hole shape in IPE and IPN perforated shear connectors, which is more easily executed on-site, exhibits superior ultimate load capacity but less interfacial slip compared to the circular hole.
- The shear strength of IPE perforated connectors is comparable to that of IPN perforated connectors, with a slight advantage observed for IPE perforated connectors.
- IPE and IPN perforated shear connectors demonstrate satisfactory ductility across tested hole shapes.
- Increasing the diameter of the passing rebar from 6 mm to 8 mm for IPE connectors results in a 12 % decrease in load capacity but a 25 % gain in ductility. On the other hand, for IPN connectors, the load capacity decreases by approx. 5 % when the perforating rebar diameter increases from 6 mm to 8 mm for the hole types studied.

- The perforating rebar plays a crucial role, particularly in resisting uplift, meeting 10 % recommendation Eurocode 4, and contributing to shear resistance in the composite slab.

- The existing analytical equations for estimating the load capacity of perforated connectors do not consider all the parameters that simultaneously affect shear strength.
- The equations proposed by Leonhardt and Veríssimo are the closest to the experimental results for estimating the load capacity of IPE and IPN perforated shear connectors.
- The experimental results were compared with the outcomes of the finite element analysis, demonstrating good agreement for all push-out specimens. The mean difference in the ultimate shear resistance observed was 1.15 %.

Acknowledgments

This research was supported by Algeria's General Directorate for Scientific Research and Technological Development (DGRSDT). We would like to give special thanks to the University of Larbi Tébessi and the Laboratory of Applied Civil Engineering. Any opinions, findings, conclusions, or recommendations expressed in this publication are solely those of the authors.

References

1992. Eurocode 2: Design of concrete structures - Part 1-1: General rules and rules for buildings. BSI British Standards.
1993. Eurocode 3. Design of steel structures - Part 1-1: General rules and rules for buildings.. BSI British Standards.
1994. Eurocode 4: Design of composite steel and concrete structures - Part 1.1: General rules and rules for buildings. BSI British Standards.
- Aegerter, J., Kühn, H.-J., Frenz, H., and Weißmüller, C. (2011). EN ISO 6892-1:2009 Tensile testing: initial experience from the practical implementation of the new standard*. *Materials Testing*, Vol. 53, Issue 10, pp. 595–603. DOI: 10.3139/120.110269.
- Ahn, J.-H., Lee, C.-G., Won, J.-H., and Kim, S.-H. (2010). Shear resistance of the perfobond-rib shear connector depending on concrete strength and rib arrangement. *Journal of Constructional Steel Research*, Vol. 66, Issue 10, pp. 1295–1307. DOI: 10.1016/j.jcsr.2010.04.008.
- Al-Darzi, S. Y. K., Chen, A. R., and Liu, Y. Q. (2007). Finite element simulation and parametric studies of perfobond rib connector. *American Journal of Applied Sciences*, Vol. 4, No. 3, pp. 122–127. DOI: 10.3844/ajassp.2007.122.127.
- Allahyari, H., Nikbin, I. M., Saman Rahimi, R., and Heidarpour, A. (2018). A new approach to determine strength of Perfobond rib shear connector in steel-concrete composite structures by employing neural network. *Engineering Structures*, Vol. 157, pp. 235–249. DOI: 10.1016/j.engstruct.2017.12.007.
- Barbero, E. J. (2023). *Finite Element Analysis of composite materials using Abaqus*. Boca Raton: CRC Press, 406 p.
- Bujnak, J. (2007). *Analyse globale de poutres mixtes acier béton: approche analytique et modélisation non-linéaire*. DSc Thesis in Civil Engineering.
- Cândido-Martins, J. P. S., Costa-Neves, L. F., and Vellasco, P. C. G. d. S. (2010). Experimental evaluation of the structural response of Perfobond shear connectors. *Engineering Structures*, Vol. 32, Issue 8, pp. 1976–1985. DOI: 10.1016/j.engstruct.2010.02.031.
- Costa-Neves, L. F., Figueiredo, J. P., Vellasco, P. C. G. d. S., and Vianna, J. d. C. (2013). Perforated shear connectors on composite girders under monotonic loading: an experimental approach. *Engineering Structures*, Vol. 56, pp. 721–737. DOI: 10.1016/j.engstruct.2013.06.004.
- Dreux, G. and Festa, J. (2007). *Nouveau guide de béton et ses constituants*. 8th edition. Paris: Eyrolles, 416 p.
- Farid, B. and Boutagougua, D. (2021). Parametric study of I-shaped shear connectors with different orientations in push-out test. *Frattura Ed Integrità Strutturale*, Vol. 15, No. 57, pp. 24–39. DOI: 10.3221/igf-esis.57.03.
- Jarek, B. (2004). *Fissuration de la dalle dans les poutres mixtes acier béton*. DSc Thesis.
- Kim, S.-H., Han, O., Kim, K.-S., and Park, J.-S. (2018). Experimental behavior of double-row Y-type perfobond rib shear connectors. *Journal of Constructional Steel Research*, Vol. 150, pp. 221–229. DOI: 10.1016/j.jcsr.2018.08.012.
- Leonhardt, F., Andra, W., Andra, H.-P., and Harre, W. (1989). New improved bonding means for composite load-bearing structures with high fatigue strength. *International Journal of Fatigue*, Vol. 11, No. 6, pp. 449–449. DOI: 10.1016/0142-1123(89)90207-7.
- Liu, Y., Guo, L., Shi, J., and Wang, J. (2021). Push-out tests of shear connectors in U-shaped steel–concrete composite girder. *Structures*, Vol. 31, pp. 769–780. DOI: 10.1016/j.istruc.2021.02.018.
- Maquoi, R., Debruyckere, R., Demonceau, J.-F., and Pyl, L. (2010). *Construction mixte*. Bruxelles: Infosteel8. Number of Pages 208.
- Medberry, S. B. and Shahrooz, B. M. (2002). Perfobond shear connector for composite construction. *Engineering Journal*, Vol. 39, No. 1, pp. 2–12. DOI: 10.62913/engj.v39i1.771.
- Oguejiofor, E. C. and Hosain, M. U. (1994). A parametric study of perfobond rib shear connectors. *Canadian Journal of Civil Engineering*, Vol. 21, No. 4, pp. 614–625. DOI: 10.1139/l94-063.
- Su, Q.-T., Wang, W., Luan, H.-W., and Yang, G.-T. (2014). Experimental research on bearing mechanism of perfobond rib shear connectors. *Journal of Constructional Steel Research*, Vol. 95, pp. 22–31. DOI: 10.1016/j.jcsr.2013.11.020.
- Veríssimo, G. S., Paes, J. L. R., Valente, I., Cruz, P. J. S., and Fakury, R. H. (2006). Design and experimental analysis of a new shear connector for steel and concrete composite structures. In: da Sousa Cruz, P. J., Frangopol, D. M., and Canhoto Neves, L. C. (eds.). *Advances in Bridge Maintenance, Safety Management, and Life-Cycle Performance*. London: CRC Press, pp. 1313–1322.
- Vianna, J. d. C., Costa-Neves, L. F., Vellasco, P. C. G. d. S., and de Andrade, S. A. L. (2008). Structural behaviour of T-Perfobond shear connectors in composite girders: an experimental approach. *Engineering Structures*, Vol. 30, Issue 9, pp. 2381–2391. DOI: 10.1016/j.engstruct.2008.01.015.

Vianna, J. d. C., Costa-Neves, L. F., Vellasco, P. C. G. d. S., and de Andrade, S. A. L. (2009). Experimental assessment of Perfobond and T-Perfobond shear connectors' structural response. *Journal of Constructional Steel Research*, Vol. 65, Issue 2, pp. 408–421. DOI: 10.1016/j.jcsr.2008.02.011.

Viest, I. M., Siess, C. P., Appleton, J. H., and Newmark, N. M. (1951). Full-scale tests of channel shear connectors and composite t-beams. *University of Illinois Bulletin*, Vol. 50, No. 29, 155 p.

Wang, X., Liu, Y., and Liu, Y. (2018). Experimental study on shear behavior of notched long-hole perfobond connectors. *Advances in Structural Engineering*, Vol. 22, Issue 1, pp. 202–213. DOI: 10.1177/1369433218782991.

Zhao, C., Li, Z., Deng, K., and Wang, W. (2018). Experimental investigation on the bearing mechanism of Perfobond rib shear connectors. *Engineering Structures*, Vol. 159, pp. 172–184. DOI: 10.1016/j.engstruct.2017.12.047.

Zhao, C. and Liu, Y.-Q. (2012). Experimental study of shear capacity of perfobond connector. *Engineering Mechanics*, Vol. 29, No. 12, pp. 349–354. DOI: 10.6052/j.issn.1000-4750.2011.09.0604.

Zheng, S., Liu, Y., Yoda, T., and Lin, W. (2016). Parametric study on shear capacity of circular-hole and long-hole perfobond shear connector. *Journal of Constructional Steel Research*, Vol. 117, pp. 64–80. DOI: 10.1016/j.jcsr.2015.09.012.

ЭКСПЕРИМЕНТАЛЬНОЕ ИССЛЕДОВАНИЕ СОПРОТИВЛЕНИЯ СДВИГУ I-ОБРАЗНЫХ ПЕРФОРИРОВАННЫХ СОЕДИНИТЕЛЬНЫХ ЭЛЕМЕНТОВ В СОСТАВНЫХ БАЛКАХ

Фарид Бурса*, Рафик Буфар, Абдеррахмани Сифеддин

Университет Ларби Тебесси, Тебесса, Алжир

*E-mail: farid.boursas@univ-tebessa.dz

Аннотация

Введение: в сооружении мостов широко используются сталежелезобетонные составные балки, при этом решающее значение имеет стабильность стыка. Соединительные элементы, работающие на сдвиг, и железобетонные плиты играют ключевую роль в качестве соединителей. Для того чтобы спрогнозировать общую реакцию системы, необходимо понимание взаимодействия между составной балкой и плитой. Требуется оптимизировать соединение стальных балок и железобетонных плит в сталежелезобетонных составных балках и облегчить их сборку и установку на месте, акцентируя внимание на их ключевой роли в поддержании структурной целостности комбинированных систем. **Цель исследования** — выполнить экспериментальное исследование и численное моделирование с использованием метода конечных элементов. В ходе исследования использовались следующие **методы:** изучение поведения перфорированных соединительных элементов IPE и IPN, работающих на сдвиг, с помощью испытаний на выдавливание. Основной задачей было проанализировать, как I-образный перфорированный соединительный элемент, бетонная плита, стальная балка и арматура влияют на величину скольжения между стальной балкой и бетонной плитой. Для этого использовались образцы с соединительными элементами IPE80 или IPN80, работающими на сдвиг, с круглыми отверстиями и длинными отверстиями с прорезью, содержащими стальные стержни диаметром 6 и 8 мм, с тем чтобы повысить сопротивление соединительного элемента к воздействию сил отрыва. Испытательная установка соответствует рекомендациям Еврокода 4, при этом особое внимание уделяется форме отверстия и диаметру арматуры, работающей на сопротивление силам отрыва. Типы разрушения были главным образом обусловлены разрушением бетонной плиты. **Результаты:** было установлено, что геометрия отверстий в перфорированных соединительных элементах IPE и IPN, работающих на сдвиг, оказывает существенное влияние на пластичность и способность выдерживать сдвиговые нагрузки. Длинное отверстие с прорезью в перфорированных соединительных элементах IPE и IPN, работающих на сдвиг, обеспечивает более высокую предельную несущую способность, но меньшее скольжение между поверхностями по сравнению с круглым отверстием. Перфорированные соединительные элементы IPE и IPN, работающие на сдвиг, продемонстрировали удовлетворительную пластичность для всех рассмотренных форм отверстий, а трехмерные конечно-элементные модели согласуются с результатами испытаний.

Ключевые слова: составные балки, I-образные перфорированные соединительные элементы, сопротивление сдвигу в зависимости от нагрузки, испытание на выдавливание, пластичность, метод конечных элементов.

PHOTO-REACTIVE ACRYLIC-ALKYD COMPOSITION WITH BIOCIDES ADDITIVE FOR WOOD PROTECTION COATING DEVELOPMENT

Viktoria Il'ina¹, Valeria Strokova^{1*}, Vladimir Erofeev², Irina Stepina²

¹Shukhov Belgorod State Technological University, Belgorod, Russia

²National Research University "Moscow State University of Civil Engineering", Moscow, Russia

*Corresponding author's email: vvstrokova@gmail.com

Abstract

Introduction. The study of photo-reactive varnishes can serve as a basis for choosing alternatives in the restoration and preservation of historical and cultural heritage sites. **Purpose of the study:** The study aimed to explore the possibility of using photoreactive acrylic-alkyd composition with biocide additive as a paint and varnish material in construction as well as restoration and preservation. **Methods.** The possibility of obtaining protective thick-layer coatings from the proposed compositions with a thickness up to 80 μm without compromising polymerization efficiency in the layer was demonstrated by express Raman spectroscopy. **Results.** The coatings obtained by UV-curing from the composition with vinylated alkyd oligomers were tested to analyze vapor permeability, hardness, and hydrophobicity. The resistance of the specimens coated with the developed compounds against a mixture of mold fungi was studied. *Aspergillus*, *Chaetomium*, *Trichoderma* and *Penicillium* fungi were used as strains of micromycetes as those most infesting the open surfaces of timber. The effectiveness of biocide additive in the amount of 0.24 wt % is shown. The developed photo-reactive varnishes make it possible to form a finished wood coating within 1–2 minutes.

Keywords: photo-reactive varnishes, wood coatings, restoration, preservation and construction, alkyd oligomers.

Introduction

Photo-reactive compositions and materials on their basis are used in many fields, which is due to the invariance of their properties set at the stage of formulation and composition development (Babkin et al., 2022; Feng et al., 2023; Ge et al., 2021; Petrov et al. 2023; Ruskol et al., 2008).

The principle of formulation of such compositions is based on the polymerization theory provisions: the presence of compounds with unsaturated double bonds in the system determines the possibility of their reaction with the formation of a new high molecular weight compound, the properties of which will be determined by its molecular weight, structure and its regular pattern. The specifics of the material and its performance will be determined by the presence of functional additives in the formulation, the amount of which is not strictly regulated and is determined only by the composition development process conditions. Thanks to additives, it is possible to regulate the properties of the future material. For example, it is possible to develop protective or decorative coatings for any surface, considering its life cycle, operating conditions, and nature (Babkin et al., 2019; Kondrashov and Kozlova, 2022a).

In any case, the composition formulation will represent a complex system containing additives that a priori should not be antagonistic, nor should they discretely or integrally inhibit the polymerization process (Babkin et al., 2019; Kondrashov and Kozlova, 2022b; Susorov and Babkin, 2015).

Formulation always starts with the selection of film formers. Acrylic oligomers and monomers have traditionally been the most widely used. Oligomers are mainly represented by urethane acrylates, epoxy acrylates, and polyether acrylates. The range of monomers is wider, and their selection is based on the number of bonds capable of polymerization (functionality): isobornyl acrylate (IBOA), hexanediol diacrylate (HDDA), trimethylolpropane triacrylate (TMPTA), etc. (Babkin et al., 2019; Chisholm et al., 2006; Kondrashov and Kozlova, 2022a; Susorov and Babkin, 2015).

An important advantage of photo-reactive systems, compared to organic solvent systems, is the absence of aggressive solvents, which is especially important when handling wood, especially historical wood that has already undergone biocorrosion (Babkin et al., 2021; Il'ina and Strokova, 2023).

In the development of photo-reactive varnish compositions for wood surface coating, the issue of wood biological resistance is the most significant, especially if the life cycle of the object implies operation under extreme conditions (external climatic impact, impact of biological and soil factors, etc.) (Skorokhodov and Shestakova, 2004). This issue can be solved in two ways: by introducing a corresponding additive (antiseptic additive, biocide) into the formulation or by using a copolymerizing film former, which inherently has a bioprotective function. The first option represents a simpler solution, since the range of such additives is quite

large, and the main patterns of the growth of the coating biological resistance due to the introduction of such additives are easy to predict. However, there is a disadvantage: additives not chemically bonded to the polymer easily migrate within the layer to the surface, and further from the surface, and over time the protection weakens. It is obvious that the kinetics of this process will accelerate if the external conditions of the object operation promote the washing-out of additives from the thin coating layer. There is a solution, which is employed in production wood coatings using photo-reactive varnishes, when the surface is pre-prepared (grinding, surface priming or impregnation) and only after that covered with a thin layer of liquid photo-reactive varnish, almost instantly forming a preserving varnish film. This method is mainly suitable for construction and is not always adequate for restoration and preservation, especially when it comes to an object for which it was decided to perform scientific restoration using authentic materials and recreating the historical appearance of the object.

The second option is more complicated in terms of technology, and, although it is not difficult to select a copolymerizing film former due to the limited choice (among the available options, alkyds are suitable for this purpose), later the process becomes only relatively predictable, since alkyds (and their derivatives — vinylated alkyd oligomers (VAO)) are made from natural raw materials (Drinberg, 2014). Reproducibility of VAO properties in different batches does not always meet expectations — the main difficulty lies in the fact that VAO are characterized by wide and variable molecular-mass distribution with an average molecular mass of 2000–3000. Such variability of properties is determined in synthesis by the use of vegetable oil — a natural raw material, the quality of which depends on a set of unpredictable conditions, including climatic ones, and the amount of vinyl toluene used in resin modification. Therefore, when handling raw materials from different batches, every time it is required to adjust formulations, check curing kinetics, determine the properties of the coatings formed, and take other actions to match the properties set during the initial use of resin (Drinberg, 2014; Poth, 2009; Yakhontova, 1988).

In addition, the effectiveness of biological protection in this case is much lower than when using synthetic biocides. Thus, given the pros and cons of both methods, it is logical to use the third option, when in the formulations of photo-reactive varnishes, synthetic biocides, introduced prior to the application to the surface, are used simultaneously with the film former, which inherently has a bioprotective function.

Alkyd resins, which are traditionally used in the domestic paint and varnish industry, but mainly in siccative systems, can serve as such a film former (Drinberg, 2014; Yakhontova, 1988). Babkin et al.

(2014) proved the possibility of using modified alkyd resins — vinyl toluene alkylated alkyds — as film formers of photo-reactive compositions developed to produce coatings using UV-curing. UV-curable compositions can be used for operational object preservation and for restoration using the synthetic method, which involves a balanced combination of archaeological restoration and compilation stylization. They also can be used during restoration and preservation using anastylis and during renovation as a reasonable choice of preservation of severely destroyed objects not included in the World Heritage List.

Subject, tasks, and methods

The subject of the study was photo-reactive compositions based on two film formers: ethoxylated TMPTA (CAS 28961-43-5) and VAO with different vinyl-toluene content. A photo-initiating mixture of 1-hydroxycyclohexyl phenyl ketone (CAS 947-19-3) with benzophenone (TS 6-09-08-2006-89) in a ratio of 3.6:2 was used as a reaction activator, with a total initiator content in the formulation of 5.6 wt %.

The task of the study was to develop a highly reactive composition that would allow for the rapid formation of a ready-to-use coating comparable in hardness to an organic solvent-based varnish coating. The technical requirements for the coating also included hydrophobicity, optical transparency (to preserve the visual effect of the natural wood surface), and biological resistance.

The compositions were prepared in a laboratory vertical bead mill with glass beads in accordance with GOST R 50563.4-93, observing the following order of component introduction: first, ethoxylated TMPTA was loaded into the working vessel, then 1-hydroxycyclohexyl phenyl ketone and benzophenone photoinitiators were added to it; then grinding was carried out, with the process control regarding the degree of initiator dissolution. The degree of dissolution was determined visually by pouring the mixture onto glass. The homogeneity of the composition and the absence of inclusions on the glass were checked. Then process additives were introduced to ensure further process (dispersant Tego Dispers 670, defoamer Tego Airex 991), and mixing was carried out. The prepared homogeneous mass was filtered, introduced into a VAO solution (80 % solution in vinyl toluene), and mixed.

The Brookfield viscosity of the prepared compositions was determined using a Brookfield DV-E viscometer (530 mPa·s).

The prepared compositions were stored in containers protected against active UV radiation with tightly closed lids.

The criteria for the selection of biocide additive were as follows: minimum possible toxicity and aggressiveness to the surface to be protected + high biocidal protection + minimum particle size in case

of powder-type additive (limitations on the particle size of the solid phase were imposed due to the utilized coating formation technology). Polyphase biocide (trade name Polyphase R2085) was chosen as the optimal additive. It is recommended for protecting interior materials and exterior surfaces against fungal infestations. It is known for ensuring protection against mold fungi in coatings for interior and exterior applications: paint, plaster, pigment dispersions, pigmented wood stains. It is believed to be active against a wide variety of fungal microorganisms (mold, wood-staining fungi). The active biocide components are carbendazim (ISO) and 3-iodo-2-propynyl-butyl carbamate.

The choice of Polyphase biocide, among the existing range of active additives for wood protection, is due to the previously proven effectiveness of its use for alkyd systems, as the primary task of the study was to test the hypothesis of the possibility of use and effectiveness of the biocide in photo-reactive systems with the addition of VAO.

Additional advantages of this additive were its liquid form (free-flowing dispersion), low content of volatile organic substances, and previously demonstrated high efficiency in alkyd systems (Anikina, 2014), since in this study it is planned to use it in compositions containing VAO. The intrinsic viscosity of the additive (400 mPa·s at 25 °C) was comparable to that of the prepared composition (530 mPa·s at 25 °C); the biocide was introduced into the composition directly prior to its application on wood.

Coatings for fungus resistance studies were obtained by applying the composition with VAO to wooden planks (spruce) of 30×40×15 mm. Different wood moisture conditions were simulated. The wet wood batch was held in desalinated water for 7 days. The dry wood batch was maintained in a thermostat at a constant temperature of +60 °C for 7 days. The specimens of the wood treated and maintained at different moisture conditions were kept under standard storage conditions, at room temperature, without direct exposure to sunlight, heating, or forced air conditioning. The moisture content in the wood was assessed by changes in the weight of the specimens.

The compositions were applied using a four-range rectangular applicator with a gap thickness of 30 µm. The coatings were cured using an ORK-21 M1 unit with a DRT-400 mercury lamp. Radiation intensity was recorded using a UV Power Puck II UV photometer. UV radiation intensity amounted to: HA = 135 mW/cm²; HB = 150 mW/cm²; HC = 24 mW/cm²; HV = 90 mW/cm². The coating thickness was not determined; the concept of “material consumption per surface area” was used for evaluation.

To study the fungus resistance of the compositions considered in this work, three wood specimens (30×40×15 mm) were prepared for

each composition of photo-reactive varnish (without biocide as well as with the addition of biocide in different concentrations); wood without coating served as a control. After that, the specimens were infested with aqueous suspension of spores of the mold fungi mixture, containing the test cultures under consideration, using a sprayer and placed in Petri dishes.

Fungi of the following genera were used as strains of micromycetes for modeling of real operation conditions: *Aspergillus* (as the most active biodegradants of acrylic paint materials (Anikina and Smirnov, 2013)), *Chaetomium*, *Trichoderma*, and *Penicillium* (as those most infesting the open surfaces of timber (Mazanik and Snopkov, 2009)). For instance, the following strains of micromycetes were considered in the course of the study: *Aspergillus niger van Tieghem*; *Aspergillus terreus Thom*; *Chaetomium globosum Kunze*; *Trichoderma viride Pers. ex. Fr.*; *Penicillium ochrochloron Thom*. To prepare spore suspension, dry spores of the selected species of mycelial fungi were transferred into a flask containing 50 cm³ sterile tap water, thoroughly mixed by shaking and rubbing with a glass rod with a rubber tip until all lumps were dispersed. The prepared suspension was filtered through four layers of sterile gauze. The spore concentration of each fungal species in the suspension was 1–2 million/cm³. To prepare spore suspension, a working batch of 14-day-old (counting from the day of inoculation) test-cultures of micromycetes was used. The Petri dishes were stored under conditions for optimal fungal growth: at 29 °C and 90 % relative humidity.

The study was aimed to reveal the nature of growth and development of fungi on the surface of the investigated specimens with and without coating. As a characteristic for the determination of microbiological resistance of materials, their fouling by microscopic fungi was considered, which was established after 28 days from the beginning of the experiment; the degree of fungi development was evaluated on a 5-score scale (Table 1), according to GOST 9.048–89 “Unified system of protection against corrosion and aging. Technical items. Methods of laboratory tests for resistance to mold fungi”.

Vapor permeability and microhardness were evaluated on free films. The films were obtained using the method of obtaining free films according to GOST 14243-78 “Paint and varnish materials” on plates (fluoroplastic-4), previously degreased with acetone.

The hydrophobicity of the applied coating was evaluated by the value of surface energy, evaluation was carried out by the value of the wetting angle on a laboratory unit using the sessile drop method (Fig. 1).

Comparison liquids — water and glycerin — were used, which were applied to the coating with a dispenser, to exclude stochastic error —

Table 1. Intensity of fungi development

Score	Score characteristics
0	No germination of spores and conidia was found under the microscope
1	Under the microscope, germinated spores and slightly developed mycelium can be seen
2	Under the microscope, developed mycelium can be seen, possible sporulation
3	Mycelium and/or sporulation are barely visible to the naked eye, but clearly visible under the microscope
4	Development of fungi covering less than 25 % of the test surface is clearly visible to the naked eye
5	Development of fungi covering more than 25 % of the test surface is clearly visible to the naked eye

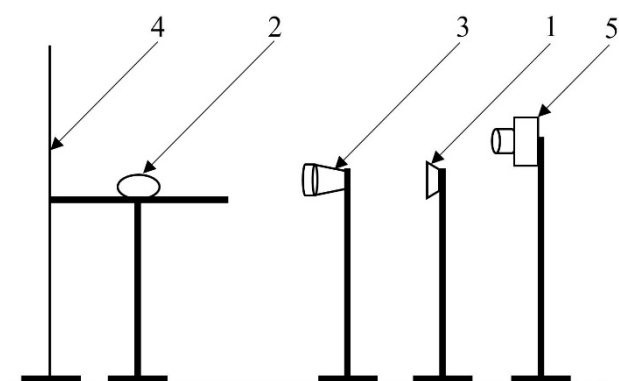


Fig. 1. Unit to determine the wetting angle, where: 1 — light source; 2 — test surface (specimen) on the work table; 3 — set of lenses, 4 — screen, 5 — photo camera

3–5 drops at a time, 2–3 mm in diameter. Imaging was performed under darkened conditions, with a time delay of no more than 30 s after drops were applied to the surface. The photos of the drops were processed in a graphic editor. The values of the wetting angles were calculated in MatLab with a special application by arithmetic mean of five measurements for each point. Based on the data obtained, surface energy values were calculated using the Owens–Wendt–Kaelble equation:

$$\frac{1}{2} \sigma_{lg} (\cos \theta + 1) = \left(\sigma_{lg}^d \right)^2 \left(\sigma_{sg}^d \right)^2 + \left(\sigma_{lg}^p \right)^2 \left(\sigma_{sg}^p \right)^2, \quad (1)$$

where θ — the wetting angle of water or glycerin; σ^d and σ^p — dispersion and polar components of surface energy at the interfaces, SG — solid/gas, LG — liquid/gas.

The vapor permeability of the free films was determined according to GOST 25898-2020 “Building materials and products. Methods for determination of vapor permeability and vapor permeability resistance” (dry cup method), using a laboratory analog as a test vessel.

Mendelev cement was used as a sealant. Phosphoric anhydride according to GOST 212317 was used as an absorbing material. The device was placed in a desiccator where a constant humidity of ~95 % was maintained due to a saturated solution of copper sulfate (GOST 19347-99). The testing devices with the specimens were weighed on analytical scales every 24 hours for 8 days.

Hardness measurements were performed using a PMT-3 microhardness tester (GOST 7865-77). Hardness values were calculated based on the length of the diamond pyramid impression diagonal (mm). Microhardness was calculated according to Eq. 2:

$$H = 1.854 \times P / C, \quad (2)$$

where P — load, g; C — impression diagonal length, mm.

Raman spectroscopy was used to determine the degree of conversion of unsaturated bonds. The study was carried out using a SENTERRA express Raman spectrometer with a Raman spectrum range of 80–4500 cm^{-1} at spectral resolution of 3 cm^{-1} , laser wavelengths of 488 nm, 532 nm, 785 nm.

The optical properties of the finished coating were determined by the optical density of the free films measured using a SR-25M densitometer in transmitted light. The measurement error was determined with an accuracy up to 0.1.

Results and discussion

1. Analysis of hydrophobicity, vapor permeability, and microhardness of the coatings obtained by UV-curing from the base formulation composition

At the initial stage of studies, the hypothesis of the influence of the nature of the vegetable oil used in VAO production on the nature of its behavior in the photo-reactive system was tested. It is known (Drinberg, 2014) that the most demanded natural raw materials for VAO production are linseed, rapeseed and sunflower oils, which belong to different groups in terms of the film formation nature. Corresponding findings on the peculiarities of their behavior in siccative systems are available. However, in synergistic systems, including compositions of VAO with acrylic oligomers, the influence of the nature of the oil used is not so obvious. Only identifying the relationship of the nature of the VAO origin with the physical-mechanical and physical-chemical properties of coatings formed on wooden surfaces can serve as the basis for formulations and development of recommendations on the use of this type of materials for further application.

Based on the results of the hydrophobicity study, in accordance with the obtained values of the surface energy of the formed coatings (Table 2), it is shown that all coatings are hydrophobic. Comparison of the

Table 2. Values of the surface energy of the coatings made of compositions with VAO, prepared based on different types of vegetable oils

Type of vegetable oil	VAO designation	Indicators		
		Surface energy, mJ/m^2	Vapor permeability, $\text{mg}\times\text{cm}^2/\text{day}$	Microhardness, c.u. relative to glass
Sunflower	VAO _{SO}	33	2.7	0.48
Rapeseed	VAO _{RO}	32	3.7	0.34
Linseed	VAO _{LO}	27	9.5	0.76

coatings from the compositions with formulations including VAO obtained based on three types of vegetable oils (sunflower, rapeseed, and linseed oil) shows a minimal preference for linseed oil due to lower surface energy and, as a consequence, higher hydrophobicity. However, in practical terms, the type of oil is not determinant for this characteristic — all values of surface energy lie within the range of 27–33 mJ/m^2 .

In terms of vapor permeability, the best results were demonstrated by the coatings with VAO obtained using linseed oil, which is higher than the values of vapor permeability of the coatings synthesized based on sunflower oil — 3.5 times, rapeseed oil — 2.5 times (Table 2).

The use of oligomer, synthesized with rapeseed or sunflower oil, in the formulations of photo-reactive compositions leads to the formation of low-permeable coatings. This is a positive result for surfaces requiring effective protection in very humid environments, or coatings on metal or other non-porous material. It can also be suitable for coating particleboard or fiberboard, or other composite materials with wood filler and resin binders, but it is hardly suitable for coating porous surfaces, including natural wood.

In terms of microhardness, the best results (almost twofold increase) were demonstrated by the coatings with VAO synthesized using linseed oil.

The values of microhardness in the coatings with VAOLO synthesized using linseed oil compared to VAOSO and VAORO were 1.5–2 times higher.

The observed presence of VAOLO in the compositions is due to the chemical composition of linseed oil, which contains a greater number of acids with two and three double bonds in the molecule (glycerides of linoleic and linolenic acids predominate in the composition), compared to sunflower and rapeseed oils. In comparison, sunflower oil, for example, contains mainly fatty acids with only two double bonds (glycerides of linoleic and oleic acids predominate in the composition). As for rapeseed oil, unsaturated acids with only one double bond (glycerides of oleic acid) predominate in the composition. A large number of double bonds in the raw material molecule determines the greater ability of VAOLO to form a dense spatial polymer mesh, which ultimately leads to the formation of a harder coating.

Thus, on the basis of the foregoing, VAOLO synthesized based on linseed oil was selected for further modification with biocide additive of the benzimidazole class. The coating formed after the complete drying of VAOLO is characterized by the following physical-mechanical and physical-chemical properties: surface energy — 27 mJ/m^2 , vapor permeability — 9.5 $\text{mg}\times\text{cm}^2/\text{day}$, microhardness — 0.76 c.u. relative to glass (Fig. 2).

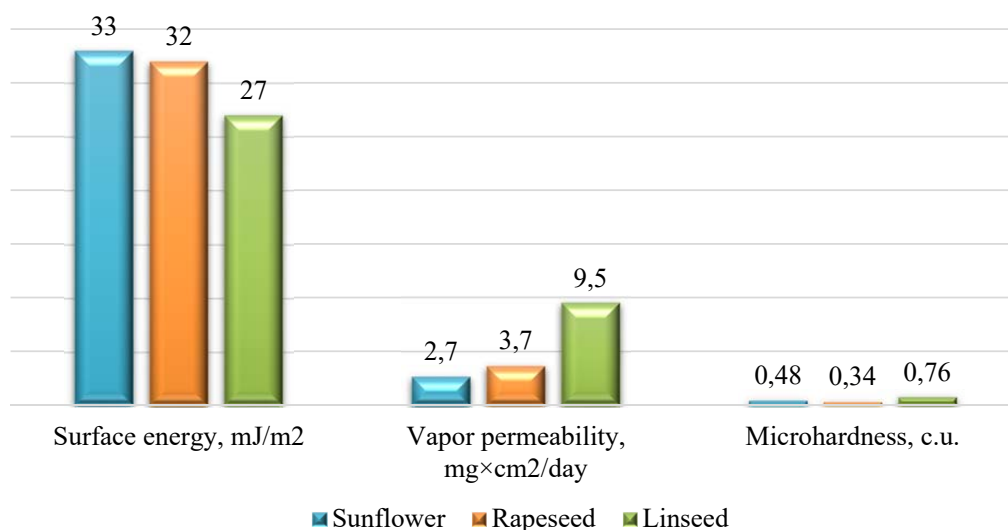


Fig. 2. Changes in the properties of VAO coatings prepared based on different types of vegetable oils

The choice of the amount of biocide additive introduced into acrylic systems modified with alkyd oligomers was justified by the recommendations of paint and varnish manufacturers (Novikova and Chizhova, 2019). It was found that the addition of Polyphase biocide in the amount of 0.24 and 0.66 wt % into the composition does not affect the change of all three parameters (Fig. 3). This fact indicates the indifference of the additive, which does not deteriorate the performance of the compositions and coatings obtained from them. Hence, an important conclusion follows that the biocide additive introduced as free dispersion does not reduce the efficiency of photo-initiated polymerization, which can be judged by the unchanged hardness of the formed coating (0.76 c.u.), which is the main requirement for additives of photo-reactive compositions.

II. Analysis of the fungus resistance of the coatings obtained by UV-curing

To study the fungus resistance of the coated wood specimens, compositions with VAOLO (synthesized based on linseed oil) were selected since this composition ensure the best coating performance, including the highest microhardness values.

During visual inspection (Fig. 4) of the wooden plates, the active growth of the test cultures was noted on the specimens without protective coating. The *Aspergillus niger* van Tieghem mold fungus turned out to be the most aggressive towards the developed materials, which was expected since this mold fungus is an active degradant for both wood and the acrylic coating (Anikina and Smirnov, 2013). In the case of control specimens, 90 % of the surface were infested and the development intensity did not decrease below 5 in all options (Table 3).

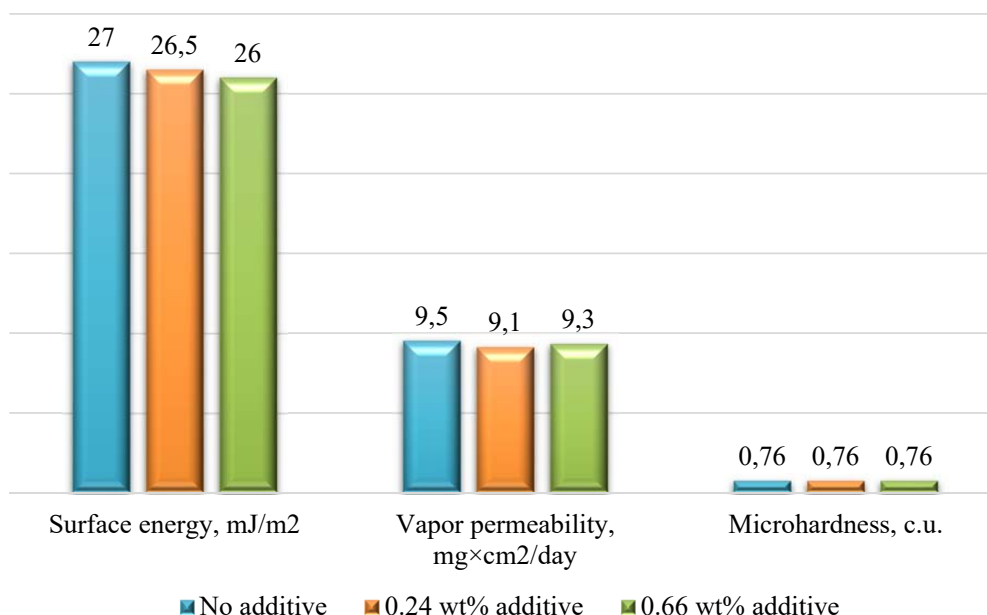


Fig. 3. Changes in the properties of the coatings with compositions with VAOLO and Polyphase additive

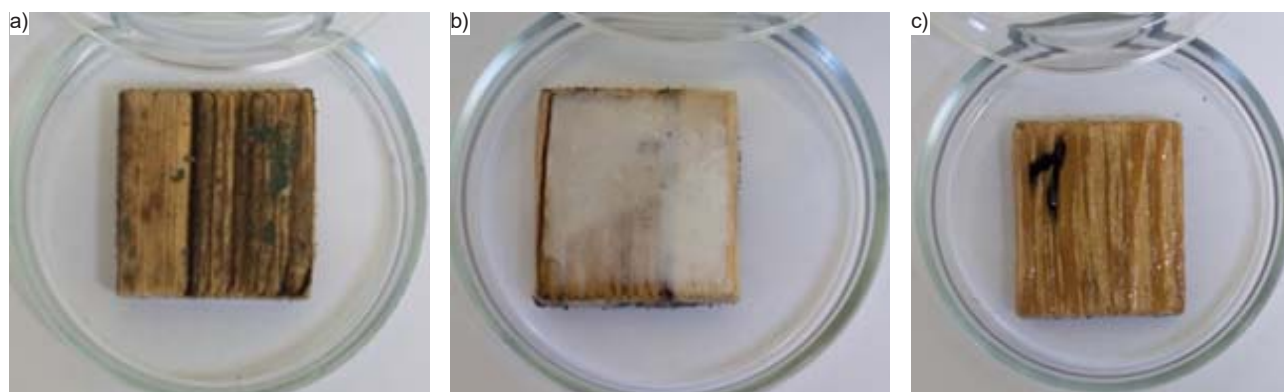


Fig. 4. Resistance of wooden surfaces to mold fungi: a — specimen without coating; b — specimen with coating without biocide; c — with biocide additive 0.24 wt %

Table 3. Fungus resistance of coatings

Specimen characteristics	Species composition of test cultures of fungi (mixture)	Score in points
specimen without coating	<i>Aspergillus niger</i> van Tieghem,	5
specimen with coating without biocide	<i>Aspergillus terreus</i> Thom, <i>Chaetomium globosum</i> Kunze	3
specimen with coating with biocide additive 0.24 wt %	<i>Trichoderma viride</i> Pers. ex. Fr. <i>Penicillium ochrochloron</i> Thom	1
specimen with coating with biocide additive 0.66 wt %		1

The response of microscopic fungi to the new material is ambiguous. Coating the wood with photo-reactive varnish without biocide forms a slight resistive barrier, reducing the intensity of development to 3, but this composition does not allow to achieve 100 % fungus resistance.

The introduction of biocide additive contributes to the reduction of fungi fouling on the surface of the model specimens (Table 2, Fig. 4). There is also a direct correlation between the amount of biocide in the coatings and the absence of growth and development of the considered micromycetes on the surface, which indicates the effectiveness of the resulting coating with account for the minimum biocide dosage.

III. Studying into the possibility of obtaining thick-layer coatings from the proposed acrylic-alkyd photo-reactive composition

Since the coatings obtained by UV-curing from the compositions with VAOLO demonstrate relatively high vapor permeability, the possibility of obtaining thick-layer coatings that simultaneously provide both air exchange of the protected wood surface

and maximum protection against mechanical and biological damage is considered.

It was taken into account that the transparency of the cured coating may decrease with increasing thickness; however, in the measured thickness range of 30–80 μm , the diffuse optical density of the free varnish films was 0–0.2; with no opalescence effect during visual inspection.

Assessment of the double bond conversion by layer depth showed that there was a slight decrease in the double bond conversion by depth (20, 40, 60, and 80 μm) (Fig. 5). This indicates that, despite an increase in the coating thickness, polymerization reactions in the depth of the coating layer take place in full, like on the surface. Therefore, it is possible to obtain thick-layer coatings in a single applied layer without changing the curing conditions.

Thus, based on the mentioned stages of the study, it is worth noting that for photo-reactive materials (UV-curing), it is important to have film formers with unsaturated bonds, capable of opening and participating in chain polymerization, in the formulation.

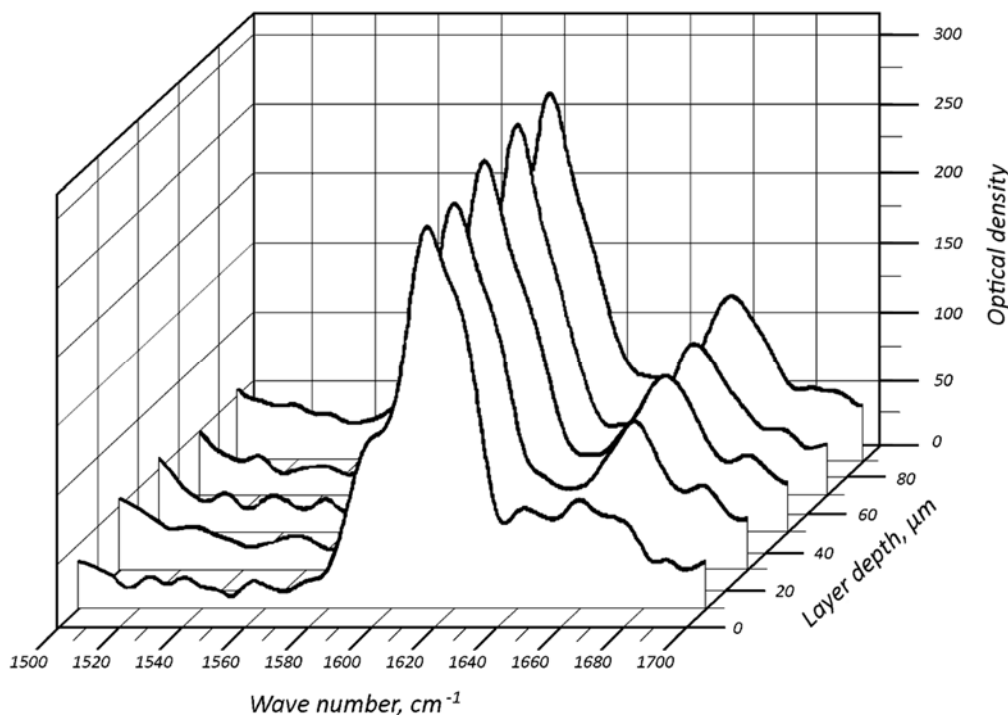


Fig. 5. Changes in the double bond conversion by depth to 80 μm in the coating obtained from the photo-reactive acrylic-alkyd composition

It is explained theoretically and proved in practice that oligomer having a large number of unsaturated bonds in the molecule (VAO) can polymerize with multifunctional (trifunctional) monomer (TMPTA) on each of the unsaturated bonds, forming a three-dimensional cross-linked matrix. The consequence of this is the relatively high microhardness of the formed coating film with the addition of VAO, which has a large number of unsaturated bonds determined by the nature of the raw material (linseed oil).

The combined use of alkyd and acrylic film formers resulted in a coating with high vapor permeability — the resulting coating allows the surface to “breathe”.

In case of such coatings, biological protection important for the surfaces of wooden materials is ensured, in our case, by the presence of alkyd (mild natural antiseptic) in the formulation and is additionally provided by the introduction of process additive in the photo-reactive composition. The main condition for all process additives — indifference to the main ingredients (film formers) — in the case of the recommended additive is indirectly confirmed by the absence of significant quantitative changes in the studied parameters of coatings when the additive is introduced in the recommended amounts.

Conclusions

Technological multitasking of developing coatings for wood — a natural material with

particular qualitative characteristics, including its application environment — implies obtaining a coating that is simultaneously protective (i. e., with maximum moisture, chemical and biological resistance), decorative, and preserving. The solution should ensure the formation of a surface coating preserving all natural qualities of the material and providing it with new characteristics. As a result, it was proposed to use photo-reactive paint and varnish material based on a mixture of artificial (alkyd) and synthetic (acrylic) film formers with the addition of biocide, allowing to form a finished wood coating within 1–2 minutes. The possibility of obtaining single-layer coatings up to 80 μm thick with a high degree of conversion of double bonds from the proposed formulation was shown.

Funding

The study was funded by the National Research University “Moscow State University of Civil Engineering” (2024 grant for fundamental and applied scientific research conducted by the members and strategic partners of the Construction and Architecture Industry Consortium, contract No. BGTU/K-24) using the equipment of the High Technology Center at the Shukhov Belgorod State Technological University.

References

- Anikina, N. A. and Smirnov, V. F. (2013). A study of resistance of some acrylic polymers to microscopic fungi. *Bulletin of Lobachevsky State University of Nizhni Novgorod*, No. 6 (1), pp. 142–145.
- Anikina, N. A., Smirnov, V. F., Kryazhev, D. V., Smirnova, O. N., Zakharova, E. A., and Grigor'eva, E. N. (2014). Investigation of the resistance of paints and varnishes used in construction, instrumentation and mechanical engineering to microscopic fungi. *Bulletin of Lobachevsky State University of Nizhni Novgorod*, No. 2 (1), pp. 100–105.
- Babkin, O. E., Babkina, L. A., Aykasheva, O. S., and Il'ina, V. V. (2019). Principles of composition of recipes, determining the properties of photo-polymer coatings and articles. *Bulletin of the Saint Petersburg State Institute of Technology (Technical University)*, No. 48 (74), pp. 63–67.
- Babkin, O. E., Babkina, L. A., Aykasheva, O. S., Il'ina, V. V., and Vlasov, M. Yu. (2022). UV curing technology. Theory and practice. *Bulletin of the Saint Petersburg State Institute of Technology (Technical University)*, No. 62 (88), pp. 6–11. DOI: 10.36807/1998-9849-2022-62-88-12-15.
- Babkin, O. E., Babkina, L. A., Aykasheva, O. S., and Ilyina, V. V. (2020). Physical-chemical grounds for preparation of formulae of liquid photopolymerized compounds for wide application. Part 1. Influence of monomer nature. *Adhesives. Sealants. Technologies*, No. 5, pp. 20–26. DOI: 10.31044/1813-7008-2020-0-5-20-26.
- Babkin, O. E., Babkina, L. A., Il'ina, V. V., and Aykasheva, O. S. (2021). Photo-curable varnishes for architectural construction and restoration. *Russian Coatings Journal*, No. 11, pp. 30–34.
- Babkin, O. E., Babkina, L. A., Letunovich, O. A., and Yatsenko, I. A. (2014). Vinylalkyd coatings UV-curing. *Russian Coatings Journal*, No. 5, pp. 61–63.
- Babkin, O. E., Il'ina, V. V., Babkina, L. A., and Sirotinina, M. V. (2016). UV-cured coatings for functional protection. *Russian Journal of Applied Chemistry*, Vol. 89, Issue 1, pp. 114–119. DOI: 10.1134/S1070427216010183.
- Chisholm, B. J., Cawse, J. N., Molaison, C. A., and Brennan, M. J. Jr. (2006). *Patent US6998425B2. UV curable coating compositions and uses thereof.*
- Drinberg, A. S. (2014). *Vinylated alkyd oligomers*. Moscow: LKM-Press, 152 p.

- Feng, R., Han, R., and Zhang, B. (2023). Ultraviolet curable materials for 3D printing soft robots: from hydrogels to elastomers and shape memory polymers. In: Yang, H., Liu, H., Zou, J., Yin, Z., Liu, L., Yang, G., Ouyang, X., Wang, Z. (eds.). *Intelligent Robotics and Applications. ICIRA 2023. Lecture Notes in Computer Science*, Vol. 14270. Singapore: Springer, pp. 12–21. DOI: 10.1007/978-981-99-6492-5_2.
- Ge, Q., Chen, Z., Cheng, J., Zhang, B., Zhang, Y.-F., Li, H., He, X., Yuan, C., Liu, J., Magdassi, S., and Qu, S. (2021). 3D printing of highly stretchable hydrogel with diverse UV curable polymers. *Science Advances*, Vol. 7, No. 2, eaba4261. DOI: 10.1126/sciadv.aba4261.
- Il'ina, V. V. and Strokova, V. V. (2023). Photopolymer materials in the practice of restoration and conservation works on objects of historical and cultural value. *Construction Materials*, No. 12, pp. 76–83. DOI: 10.31659/0585-430X-2023-820-12-76-83.
- Kondrashov, E. K. and Kozlova, A. A. (2022a). UV-quantum technologies of formation protective, decorative and functional polymer coatings. Part I. Film-forming agents of UV-polymerized coatings. *Russian Coatings Journal*, No. 7–8 (546), pp. 20–26.
- Kondrashov, E. K. and Kozlova, A. A. (2022b). UV-quantum technologies of formation protective, decorative and functional polymer coatings. Part II. Pigments, fillers, additives and compositions for UV-curable coatings. *Russian Coatings Journal*, No. 9 (547), pp. 14–20.
- Mazanik, N. V. and Snopkov, V. B. (2009). Test-cultures of fungi for testing wood protection products. *Proceedings of BSTU. No. 2. Forest and Woodworking Industry*, No. 2, pp. 194–198.
- Novakov, I. A., Chalykh, A. E., Nistratov, A. V., Frolova, V. I., Khasbiullin, R. R., and Klimov, V. V. (2011). Study of the influence of polysulfide oligomers in compositions based on oligoacrylates on the structure formation and properties of photocured materials. *Plasticheskie Massy*, No. 4, pp. 12–15.
- Novikova, S. I. and Chizhova, M. A. (2019). Protection of paints and coatings from biodeterioration. *Interactive Science*, No. 2 (36), pp. 39–42. DOI: 10.21661/r-473689.
- Petrov, N. S. (2023). Technology and modern market of UV-materials. *Russian Coatings Journal*, No. 5 (554), pp. 12–19.
- Poth, U. (2009). *Polyesters and alkyd resins*. Moscow: Paint-Media, 232 p.
- Ruskol, I. Yu., Alekseeva, E. I., Skripnichenko, L. A., Babin, A. N., Kitaeva, N. S., and Shvets, N. I. (2008). Optically transparent photo-curable organosilicon compositions. *Polymer Science, Series D*, Vol. 1, Issue 3, pp. 207–211. DOI: 10.1134/S1995421208030155.
- Skorokhodov, V. D. and Shestakova, S. I. (2004). *Protection of non-metallic building materials against biocorrosion*. Moscow: Vysshaya Shkola, 204 p.
- Susorov, I. A. and Babkin, O. E. (2015). *Analysis of patterns in synthesis of oligomeric and high molecular weight compounds using chain polymerization method*. Saint Petersburg: Saint Petersburg State University of Film and Television, 236 p.
- Yakhontova, V. I. (1988). *Paints and varnishes based on modified alkyd resins*. Moscow: Research Institute for Technical and Economic Studies in the Chemical Complex, 45 p.

ФОТОРЕАКТИВНАЯ АКРИЛ-АЛКИДНАЯ КОМПОЗИЦИЯ С ДОБАВКОЙ БИОЦИДА ДЛЯ СОЗДАНИЯ ЗАЩИТНЫХ ПОКРЫТИЙ ПО ДРЕВЕСИНЕ

Виктория Валентиновна Ильина¹, Валерия Валерьевна Строкова*¹, Владимир Трофимович Ерофеев², Ирина Васильевна Степина²

¹Белгородский государственный технологический университет им. В. Г. Шухова, г. Белгород, Россия

²Национальный исследовательский Московский государственный строительный университет, г. Москва, Россия

*E-mail: vvstrokova@gmail.com

Аннотация

Введение. Изучение фотореактивных лаков может служить основой для выбора альтернативных путей в реставрационно-консервационных работах на объектах историко-культурной ценности. **Цель исследования:** изучение возможности использования фотореактивной акрил-алкидной композиции с добавкой биоцида в качестве лакокрасочного материала для строительных и реставрационно-консервационных работ. **Методы.** Методом экспресс-рамановской спектроскопии показана возможность получения защитных толстослойных покрытий из предложенных композиций толщиной до 80 мкм без ущерба эффективности процесса полимеризации в слое. **Результаты.** Проведены испытания покрытий, полученных технологией УФ-отверждения из композиции с винилированными алкидными олигомерами, по параметрам паропроницаемости, твердости и гидрофобности. Изучена резистентность образцов с покрытиями из разработанных составов по отношению к смеси плесневых грибов. В качестве штаммов микромицетов были использованы грибы родов: *Aspergillus*, *Chaetomium*, *Trichoderma* и *Penicillium*, как наиболее заселяющие открытые поверхности деревянных материалов. Показана эффективность введения добавки биоцида в количестве 0,24 масс.%. Разработанные фотореактивные лаки позволяют формировать готовое покрытие по древесине в течение 1–2 минут.

Ключевые слова: фотореактивные лаки, покрытия по древесине, реставрационно-консервационные и строительные работы, алкидные олигомеры.

REDUCING THE INFLUENCE OF THERMAL BRIDGES IN THE BASEMENT SLAB OF CAST-IN-SITU FRAME BUILDINGS IN EXTREMELY COLD REGIONS

Terentii Afanasevich Kornilov*, Petr Anatolevich Fedotov, Alexey Terentevich Kornilov

M. K. Ammosov North-Eastern Federal University, Russian Federation

*Corresponding author: kornt@mail.ru

Abstract

Introduction. Heat insulation of multi-story buildings with a reinforced concrete frame on pile foundations under climatic conditions with extremely low outdoor air temperatures is complicated by high air infiltration. When such buildings are used in winter, the most characteristic are temperature regime violations on the first floor. **Purpose of the study:** The study aimed to evaluate various methods to reduce the influence of thermal bridges in the basement floor of a cast-in-situ frame building with pile foundations under extreme climatic conditions. **Methods:** Thermal performance of 3D models of enclosing structures was determined using the certified HEAT3 program. Options of internal and external heat insulation of the basement floor with thermal breaks in the structures were considered. **Results:** As a result of numerical analysis of standard basement floor designs, it was established that low temperature on the inner surface and significant heat losses are associated with the presence of through thermal bridges: reinforced concrete raft — basement slab — column — concrete block masonry. The most effective solution for heat insulation of cast-in-situ frame buildings is external heat insulation of the basement floor with a thermal break in the raft. Compared to the standard solution, heat losses through the corner section of the slab with the offset column are reduced by 33.6 %, and the minimum temperature on the inner surface is higher than the dew point.

Keywords: thermal bridge, basement floor, thermal break, column, raft.

Introduction

Nowadays, the construction of low-energy buildings has become one of the ways to improve the world's environment. Many developed countries have adopted legislative acts and energy saving programs that encourage the construction of energy efficient buildings and introduction of energy saving technologies. The countries of Europe and the United States of America were the first in the world to pay special attention to the issue of energy saving. According to the global ranking of energy-efficient countries published at the end of 2018 by the American Council for an Energy-Efficient Economy (ACEEE), Western European countries are the most advanced and developed in terms of development and application of energy efficiency measures (Castro-Alvarez et al., 2018; Gushchin et al., 2020). Looking forward, Germany is focused on only passive buildings with an energy consumption of less than 15 kW·h/m² or even zero energy consumption.

Energy-efficient buildings are, first of all, characterized by a high level of heat insulation of external enclosing structures. The minimum requirements for heat insulation of external enclosing structures in the regulatory documents of various countries are determined by economic criteria with account for natural and climatic conditions, and, therefore, have different levels. Buildings of any design have thermal bridges that increase heat losses through the enclosing structures. Therefore,

one of the basic rules for designing energy-efficient buildings is to reduce the influence of thermal bridges by structural methods and properly take them into account when determining the thermal performance. The development of innovative thermal breaks using advanced heat insulation and structural materials is paramount to reduce the influence of thermal bridges (Alhawari and Mukhopadhyaya, 2018).

Numerous works address mathematical modeling of heat flow through enclosing structures with thermal bridges under steady and unsteady influence of air temperature (François et al., 2019; Fuchs, 2022; Gagarin and Kozlov, 2010; Kang et al., 2021; Kim and Yeo, 2020; Kim et al., 2022b). It should be noted that the thermal performance of thermal bridges in operating buildings may differ from the design performance of thermal bridges obtained theoretically due to the actual construction conditions. Currently, there are methods available to quantify heat losses of enclosing structures due to thermal bridges inside using IR thermography (François et al., 2019; Kang et al., 2021; Mayer et al., 2021). In sections of enclosing structures with thermal bridges, in addition to increasing heat losses, the temperature on the inner surface decreases, which can lead to condensate formation both inside and on the surface of the structures.

The applicable regulatory documents on heat insulation of buildings employ engineering methods for calculating the reduced resistance of external enclosing structures with account for different

types of thermal bridges. In European countries, standards for thermal bridges are established separately, and in most cases their influence is not fully taken into account in the design of enclosing structures (Citterio, 2008; Gagarin and Dmitriev, 2013; Theodosiou et al., 2021). Modern software suites enable heating and heat insulation analysis of spatial units of building structures under steady and unsteady influence of air temperature.

Currently, the technology of frame construction with the use of cast-in-situ reinforced concrete structures is the most widely used in the construction of multi-story buildings. To ensure heat insulation of such buildings, depending on the climatic region of construction, two external wall options are usually used: a two-layer wall made of concrete blocks with external heat insulation made of mineral wool boards and a ventilated facade or a single-layer wall made of aerated concrete or other lightweight blocks. As for the first type of external wall, numerical and experimental studies have resulted in the development of methods for calculating the thermal performance of ventilated facades, with account for the thermally conductive elements of the cladding support, fasteners of heat insulation boards, air gap, and air filtration (Gagarin et al., 2016; Kornilov and Ambrosyev, 2008; Tushina et al., 2013).

When using a single-layer external wall, one of the traditional solutions to reduce the influence of thermal bridges is the use of perforations in the reinforced concrete floors around the perimeter of the external walls. Umnyakova et al. (2012) presented the results of evaluating heat engineering homogeneity of external walls in the area of contact with balcony slabs with perforations depending on the thickness of the reinforced concrete slab, dimensions of perforations and the wall. In buildings with a reinforced concrete frame, when single-layer external walls are used, thermal bridges occur at the locations of columns. In this case, partial heat insulation of columns using aerated concrete blocks is suggested for cold regions in China. The results of numerical studies on the effect of thermal bridges in L-shaped and T-shaped aerated concrete wall structures were confirmed by a full-scale experiment (Li et al., 2018b). Additional heat insulation of the outer surface of columns with an EPS plate leads to a greater effect in reducing heat losses (Li et al., 2018a). Unfortunately, these works did not consider the sections of the external wall with columns, including reinforced concrete floors, especially in the corner sections of the building. It is known that at these sections of external walls, the reduced resistance and temperature on the inner surface decrease sharply as the angle between adjacent walls decreases (Ingeli, 2018a, 2018b). Evola and Gagliano (2024) performed numerical and experimental studies of the corner

section of a lightweight block wall with a reinforced concrete column and established the thermal bridging effect.

In Russia, longitudinal perforation with a thermal liner made of polystyrene foam board in a reinforced concrete slab is most commonly used to reduce the impact of the balcony slab. In European countries and South Korea, load-bearing thermal breaks are used. Umnyakova et al. (2013b) presented the results of studies on the thermal performance of a section of a balcony slab and cast-in-situ external wall with perforations in the slab and installation of a Schöck (Germany) load-bearing heat insulation element. Umnyakova et al. (2013a) also demonstrated the effectiveness of using a load-bearing heat insulation element in the joints of a cast-in-situ reinforced concrete slab and balcony slab, external wall.

Numerical studies of a concrete balcony slab–wall section were conducted in South Korea by applying two types of thermal breaks using extruded polystyrene: TB — stainless steel reinforcement and TB-GFRP — glass fiber reinforcement. It was shown that the fragments of the balcony slab with the TB-GFRP thermal break in case of external wall heat insulation and floor heating system show the best thermal performance (Zhang et al., 2022). In other heat engineering studies (Kim et al., 2022a), a corner balcony with a thermal break along the long side was considered. In that case, heat losses of a three-story building were evaluated and their general reduction upon the application of thermal breaks in the balcony slabs by 4.5 % was established. In many other studies, based on numerical calculations, the thermal performance of balcony slabs of various designs was determined and the effectiveness of thermal break application was demonstrated (Aghasizadeh et al., 2022; Alhawari and Mukhopadhyaya, 2018).

The northern climatic zone of the Russian Federation is characterized by extreme climatic conditions with outdoor air temperatures below $-40\text{ }^{\circ}\text{C}$ for 50–60 days and permafrost soils. Under these conditions, multi-story buildings are mainly constructed using a cast-in-situ reinforced concrete frame on pile foundations with a ventilated under-floor space to preserve permafrost. The piles in a cluster under the frame column are united by a cast-in-situ reinforced concrete structure — a raft. Heat insulation of buildings is complicated by high air infiltration during the period of extremely low outdoor air temperatures. In the basement part of cast-in-situ frame buildings, there are extensive thermal bridges: reinforced concrete columns, rafts and piles, which significantly increase heat losses through the basement floor. Several studies (Kornilov and Vasilyeva, 2022; Kornilov et al., 2021) showed that particularly in these sections, the temperature regime of buildings is not observed and at the design outside air temperature of $-52\text{ }^{\circ}\text{C}$, the

temperature on the inner surface of the corner joints of external walls is lower than the dew point.

High air infiltration in winter especially affects the heat insulation of the basement part of buildings on pile foundations. For example, for the design outside air temperature $t_{\text{ext}} = -52\text{ }^{\circ}\text{C}$, the difference in air pressure on the outer and inner surfaces of the enclosing structures on the first floor of a 9-story and 16-story buildings is $\Delta p = 72.0\text{ Pa}$ and $\Delta p = 116.9\text{ Pa}$, respectively. Nowadays, mostly 16-story frame cast-in-situ buildings are being constructed in Yakutsk. The experience of operating such buildings showed that high air infiltration of more than 110 Pa in winter and the presence of defects in the heat insulation of the basement floor leads to intensive penetration of cold air (Kornilov and Vasilyeva, 2022).

The studies aimed to evaluate methods to reduce the influence of thermal bridges in the basement floor of multi-story buildings with a reinforced concrete frame and pile foundations under extreme climatic conditions. In standard buildings, the basement floor is heat insulated from the inside for ease of installation. With this solution, there are extensive thermal bridges in the basement slab sections: reinforced concrete columns, rafts, and the slab itself, which are load-bearing structures. In case of 16-story buildings with a reinforced concrete frame, the columns have a cross-section of $600 \times 600\text{ mm}$, the size of the raft for clusters of four piles can reach $2500 \times 2500\text{ mm}$ in plan and up to 1200 mm in height. Since the under-floor space of buildings on pile foundations is ventilated, then the cold space is located in the middle of the building on the bottom side, at the edges of the building on the bottom side and the outer side of the wall, and in the corner sections of the basement floor on three sides. All these structural features of cast-in-situ frame buildings with pile foundations pose difficulties in ensuring heat insulation of buildings under extreme climatic conditions. In case of long-lasting outside air temperatures below $-40\text{ }^{\circ}\text{C}$, a massive reinforced concrete raft with high thermal conductivity and inertia essentially represents a cold storage.

Methods

To evaluate the proposed methods of thermal bridge reduction for the basement floor of buildings with a reinforced concrete frame, the thermal performance of structural fragments was determined using the certified HEAT3 program. This computer program is designed for 3D modeling of steady and unsteady heat transfer processes. The software has been tested for compliance with EN ISO 10211–2022. In thermal bridge modeling, the design outside air temperature of the coldest five-day period with a probability of 0.92 was assumed to correspond to the climatic conditions of Yakutsk (Russia): $t_o = -52\text{ }^{\circ}\text{C}$, while the indoor air temperature was as follows: $t_i = +21\text{ }^{\circ}\text{C}$. Heating and heat insulation analysis was performed for 3D models of enclosing structures.

Thermal bridge reduction methods are evaluated based on the following thermal performance:

- minimum temperature on the inner surface of the enclosing structures (in this case, the minimum temperature on the floor);
- minimum distance from the floor surface to the zero temperature line inside the structure;
- heat losses through a fragment of the enclosing structure.

The dew point on the inner surface of the enclosing structures of residential buildings at design parameters of climate in Yakutsk and internal humidity of 50 % is $10.2\text{ }^{\circ}\text{C}$. The second characteristic is very important for comparative evaluation from a practical point of view. The close proximity of the zero temperature line to the floor surface leads to an unfavorable situation in the event of the slightest installation errors under conditions of increased air infiltration. Therefore, in climatic conditions with extremely low outside air temperatures, all connections of external enclosing structures must have high operational reliability.

• Standard solutions

At first, standard solutions of basement floor fragments in the outermost rows with an external wall, a corner basement floor section with a column and external wall are considered as models. In the outermost axes, there may still be structural solutions of the basement floor with a balcony. This case is not considered in this research, given that the first floor of multi-story buildings traditionally houses public spaces where balconies are not provided. The paper does not present the results of heat engineering studies on a basement floor section with a column in the middle rows, where the temperature regime is more favorable than at the edges of the building. For convenience of analysis, let us designate the row section of the basement floor with a column and external wall as type A, and the corner section of the basement floor with a column and two adjacent walls as type B (Fig. 1).

In all models, the reinforced concrete columns are assumed to be $600 \times 600\text{ mm}$ in cross-section, the reinforced concrete raft connecting the piles is $1800 \times 1800\text{ mm}$ in plan and 1200 mm in height. The thermal conductivity coefficient of reinforced concrete structures is $\lambda = 1.92\text{ W}/(\text{m}\cdot^{\circ}\text{C})$. The characteristics of the other materials of the external wall and basement slab are taken in accordance with Russian standards for heat insulation of buildings (Table 1). Taking into account the materials used, the thermal resistance of the flat part of the external wall is $5.26\text{ (m}^2\cdot^{\circ}\text{C)/W}$, and that of the basement slab is $7.74\text{ (m}^2\cdot^{\circ}\text{C)/W}$, which is higher than the standard values for Yakutsk.

Fig. 1 shows that in standard designs of the basement slab with internal heat insulation, there are through thermal bridges in reinforced concrete elements with high thermal conductivity, occurring in

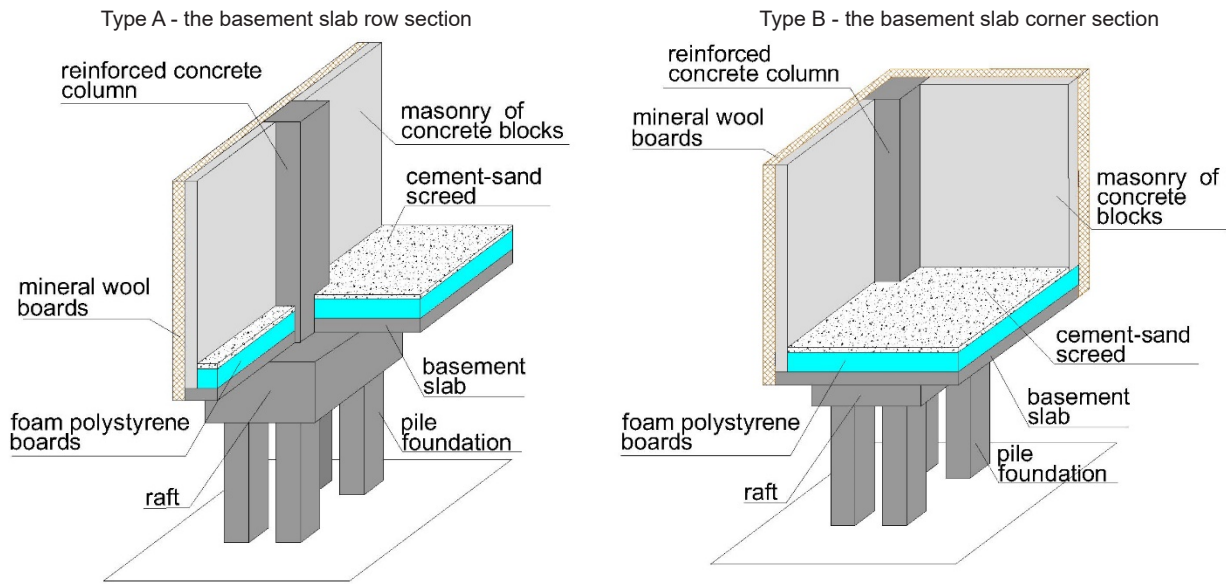


Fig. 1. Standard basement slab designs

Table 1. Characteristics of materials for standard external wall and basement slab designs

Structure	Material	Density, kg/m ³	Thickness, mm	Thermal conductivity, W/(m·°C)
External wall	Cement-sand mortar plastering	1800	20	0.76
	Concrete block masonry	1800	200	0.64
	Mineral wool boards	100	200	0.042
Basement slab	Cement-sand screed	1800	60	0.76
	Foam polystyrene boards	35	300	0.040
	Reinforced concrete slab	2500	220	1.92

the following sequence: raft – basement slab – column and concrete block masonry. In buildings with a reinforced concrete frame, the use of concrete blocks as the base of the external wall leads to the rupture of thermal protection. These thermal bridges have a particular adverse effect in the corner sections of the basement floor where two adjacent external walls are connected with the column and cold space is located on three sides (Fig. 1, type B).

• **Energy-efficient solutions**

The basic rule for reducing the influence of thermal bridges is to create thermal breaks using efficient heat insulation materials. With this in mind, the authors of the paper developed methods of constructing a basement floor with a column over cold and ventilated under-floor spaces and obtained corresponding patents. The idea is to install a thermal break made of extruded polystyrene foam between the reinforced concrete raft and the basement slab. Such a structural solution of the frame is quite possible if the load-bearing capacity of the reinforced concrete basement slab is ensured. In this case, the column is continuous and rests on the raft, which combines all the piles into a single cluster.

When a thermal break is made in the raft, there are two options of basement floor heat insulation:

internal and external. It should be noted that labor intensity of installation for internal heat insulation is much lower than that for external heat insulation under the basement slab in constraint environment.

In case of internal heat insulation of the basement slab, it is suggested to use polystyrene foam boards as individual layers (Table 2). In case of internal heat insulation, all that is left to do is to solve the issue of thermal bridging occurring in areas where the concrete block masonry rests on the basement slab. Here, two options are possible to reduce the influence of this thermal bridge:

1. Types A-1 and B-1. Use of a perforated beam with a thermal insert made of extruded polystyrene foam instead of the first row of concrete block masonry (Patent RU117943U1 (Danilov et al., 2012) obtained by one of the authors). The perforated beam can be either cast-in-situ or prefabricated. The width of the beam should be equal to the width of the concrete block masonry, i. e., 200 mm. The thermal insert is made of 200 mm thick extruded polystyrene foam. The beam supports are spaced at 1500 mm. At the wall-column junctions, the beam has a cantilever, which reduces the influence of thermally conductive elements — beam supports (Fig. 2).

Table 2. Characteristics of the materials for the proposed solutions for the internal and external heat insulation of the basement slab

Type of heat insulation	Material	Density, kg/m ³	Thickness, mm	Thermal conductivity, W/(m·°C)
Internal	Cement-sand screed	1800	60	0.76
	Foam polystyrene boards	35	300	0.040
	Reinforced concrete slab	2500	220	1.92
External	Cement-sand screed	1800	60	0.76
	Reinforced concrete slab	2500	220	1.92
	Mineral wool boards	125	300	0.042

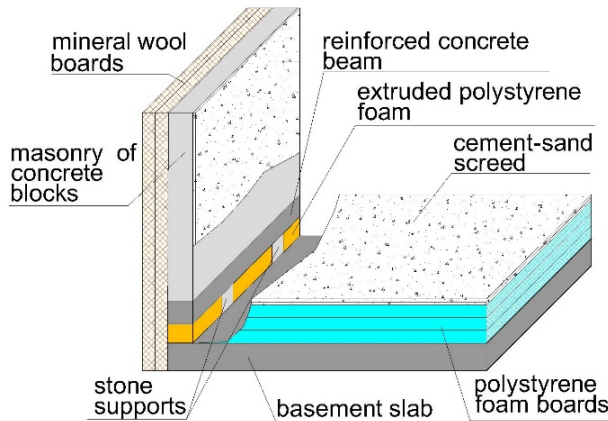


Fig. 2. Thermal break in masonry with the use of a perforated beam

2. Types A-2 and B-2. Use of lightweight blocks, e. g., polystyrene concrete blocks as the first row of wall masonry (Patent RU170253U1 (Kornilov et al., 2017) obtained by one of the authors). Polystyrene concrete blocks with a density of 500 kg/m³ have a thermal conductivity coefficient of 0.14 W/(m·°C). It is recommended to use blocks of 200×300 mm cross-section. This ensures an L-shaped connection; the joint between the lightweight masonry blocks and the end of the heat insulation boards is covered by the top layer (Fig. 3).

3. Types A-3 and B-3. External heat insulation of the basement floor from the bottom side with thermal breaks in the raft ensures the continuity of thermal protection (Patent RU2780187C1 (Kornilov et al., 2022) obtained by the authors). For external heat insulation of the basement floor, mineral wool boards with a density of 90–125 kg/m³ and a tensile strength perpendicular to the front surfaces of not less than 15 kPa should be used. The external heat insulation layer is recommended to be made of mineral wool boards with a laminated surface or to be covered

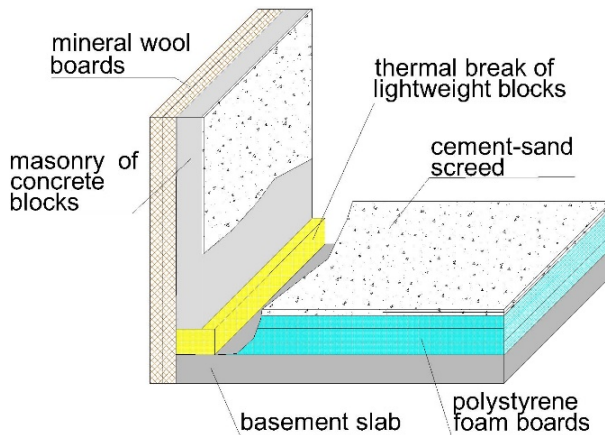


Fig. 3. Thermal break in masonry with the use of lightweight blocks

with a non-combustible water- and wind-proofing membrane. To ensure the integrity of the corner joint between the external heat insulation of the wall and the basement slab, galvanized wire mesh should be fixed in this area (Fig. 4).

Table 2 lists the materials used for the heat insulation of the basement slab. The fragments of the basement slab with internal and external heat insulation analyzed in the paper are summarized in Table 3. All the considered fragments of the enclosing structures have a thermal insert between the raft and the basement slab made of extruded polystyrene with a density of 30 kg/m³ and thermal conductivity coefficient $\lambda = 0.030 \text{ W/(m}\cdot\text{°C)}$. Extruded polystyrene is also used in the perforated wall beam.

Results

• Standard solutions

In the middle part of a cast-in-situ frame building, the heat flow passes through the column to the raft, which form a through thermal bridge (Fig. 5A). In the outermost row sections of the basement floor, the heat flow (in addition to the column with the raft) also passes through the concrete block masonry, but with less intensity (Fig. 5B). In this section of the basement floor, the minimum temperature is observed in the corner area between the column, wall and floor and amounts to +5.59 °C, which is lower than the dew point (Table 4, type A).

The worst situation is observed in the corner section of the basement slab with the column. In this section, the minimum floor temperature occurs in the corner between the column and the external wall and has a negative value of -1.52 °C, which is significantly below the dew point. The zero temperature line is 60 mm from the floor surface, i. e., under the cement-sand screed (Table 5, type B). Such a temperature regime on the inner surface of the enclosing structures in the corner section of the basement floor is due to not only the influence of thermal bridges but also the presence of cold space on three sides.

To determine the significance of thermal bridges, the thermal performance of the corner section of the standard basement slab (Type B) was determined depending on the size of the column or raft cross-section. The following variable cross-sections were assumed for the calculations:

- columns of 0.3×0.3 m, 0.4×0.4 m, 0.6×0.6 m, and 0.8×0.8 m, with a fixed raft cross-section of 1.8×1.8 m;
- raft of 1.5×1.5 m, 1.8×1.8 m, 2.2×2.2 m, and 2.5×2.5 m with a fixed column cross-section of 0.6×0.6 m;

As a result of heating and heat insulation analysis, it was found that the thermal protection of the corner section of the basement slab is mostly affected by

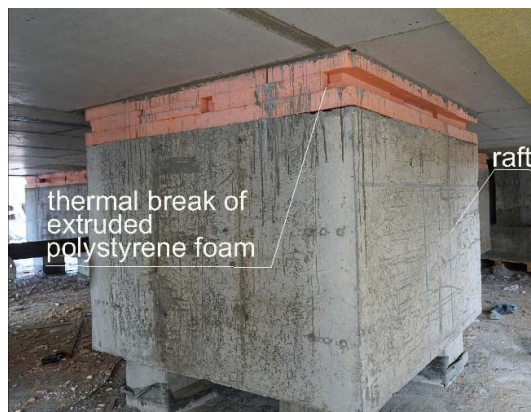
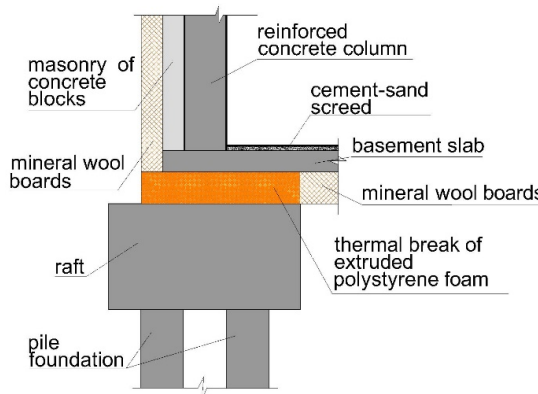


Fig. 4. External heat insulation of the basement slab with a thermal break in the raft in the section of the slab with a column of the outermost rows

Table 3. Energy-efficient solutions for the basement slab with a column in the outermost axes in the row (A) and corner (B) sections

Type	Heat insulation of the basement slab	Thickness of the basement floor heat insulation layer, mm		Thickness of the thermal break in the masonry wall, mm	Thickness of the thermal break in the raft, mm
		Polystyrene foam	Mineral wool board		
A-1 B-1	Internal	300		200 (perforated beam)	100
A-2 B-2	Internal	300		200 (lightweight block)	100
A-3 B-3	External	-	300	-	300

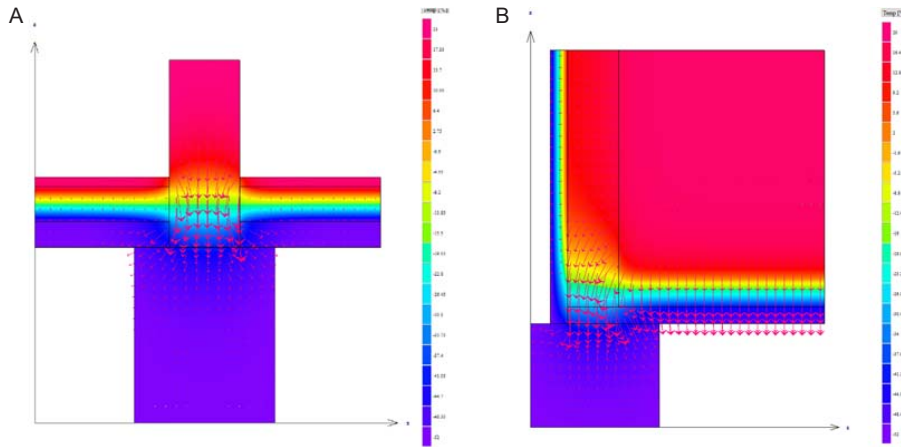


Fig. 5. Heat flow diagrams for the standard rafts and basement slab with a column of the middle (A) and outermost (B) rows

Table 4. Results of heat transfer modeling in the basement slab row section

Temperature distribution in the vertical section along the inner surface of the wall	
Type A, standard: $t_{\min} = +5.59 \text{ }^{\circ}\text{C}$; $L = 100 \text{ mm}$	Type A-1: $t_{\min} = +6.82 \text{ }^{\circ}\text{C}$; $L = 150 \text{ mm}$
Type A-2: $t_{\min} = +6.00 \text{ }^{\circ}\text{C}$; $L = 155 \text{ mm}$	Type A-3: $t_{\min} = +11.88 \text{ }^{\circ}\text{C}$; $L = 340 \text{ mm}$

L — the distance from the inner corner of the structure to the zero temperature line

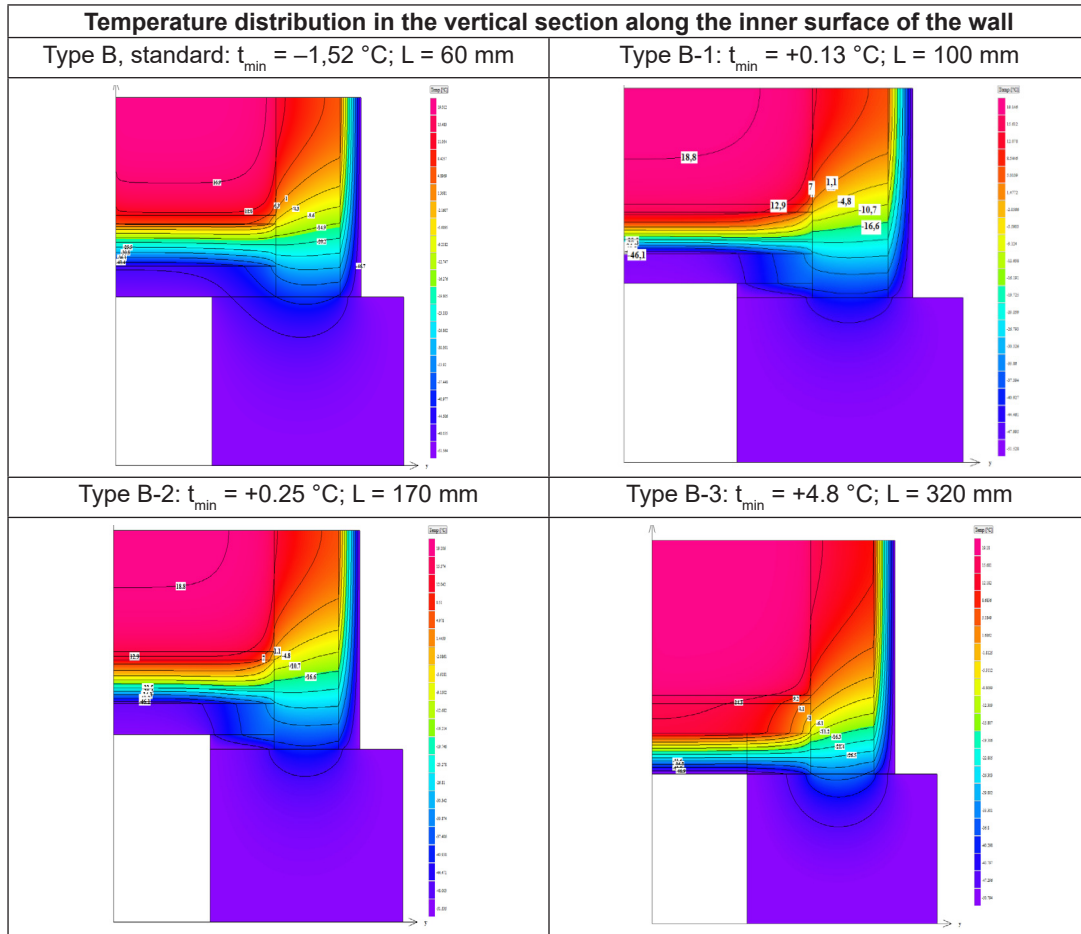
the size of the column cross-section. When the column cross-section is changed from $0.3 \times 0.3 \text{ m}$ to $0.8 \times 0.8 \text{ m}$, the minimum floor temperature decreases from $+0.2 \text{ }^{\circ}\text{C}$ to $-2.88 \text{ }^{\circ}\text{C}$, and heat losses increase by 37.0 % (Fig. 6A).

In standard designs, the reinforced concrete raft is completely in the cold zone and freezes through

the entire volume, therefore, an increase in the cross-section results in a slight increase in the minimum floor temperature within $1 \text{ }^{\circ}\text{C}$ and a decrease in heat losses by only 3.9 % (Fig. 6B).

Thus, in standard basement floor designs, in all areas under consideration, the temperature regime does not meet the regulatory requirements and the

Table 5. Results of heat transfer modeling in the basement slab corner section



L — the distance from the inner corner of the structure to the zero temperature line

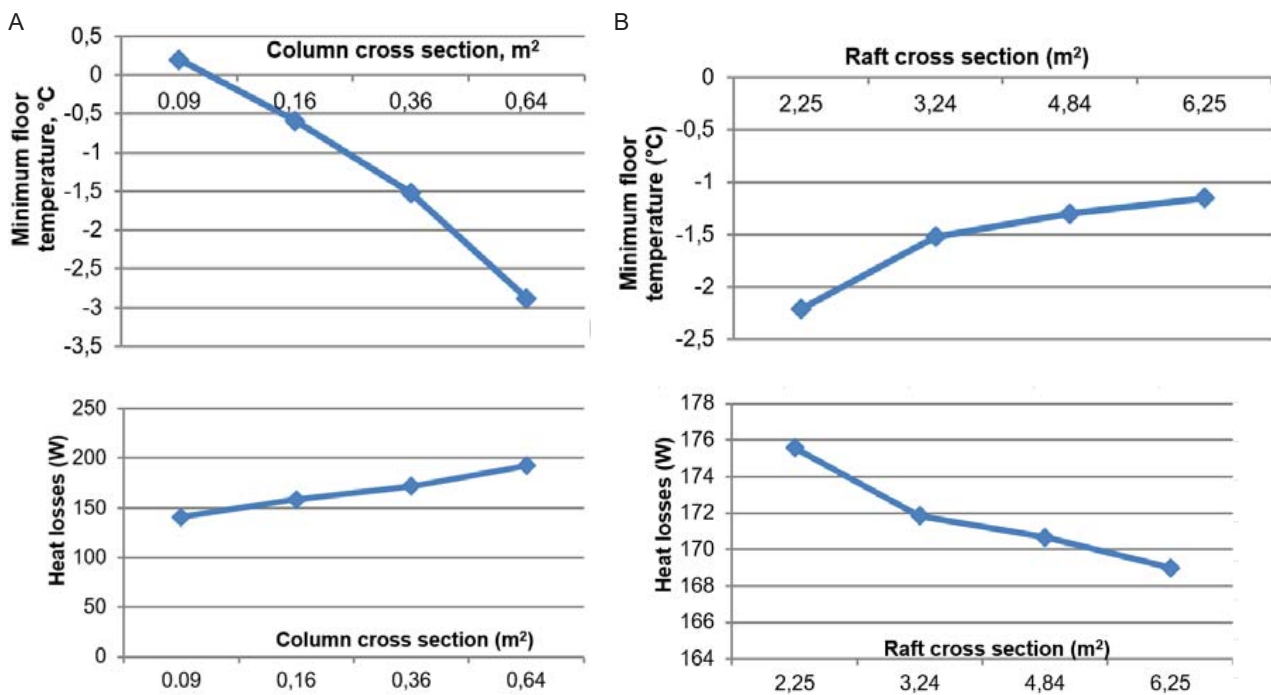


Fig. 6. Graphs of the minimum floor temperature and heat losses through the corner section of the slab as a function of the cross-section of the column (A) and raft (B)

minimum temperature on the inner surface of the enclosing structures is below the dew point.

• **Energy-efficient solutions with internal heat insulation of the basement slab**

In the proposed designs of the basement slab with internal heat insulation, the total heat flow passes through the column and raft. The heat flow through the concrete block masonry is interrupted by a perforated beam (Type A-1) or lightweight block (Type A-2) thermal insert.

In the row section of the basement slab with a column of the outermost rows, the minimum floor temperature increases by only 1.23–0.41 °C compared to the standard solution. The minimum floor temperature $t_{\min} = +6.82$ °C and $t_{\min} = +6.00$ °C when creating a thermal break in the masonry using a perforated beam and lightweight blocks, respectively, is significantly lower than the dew point. The zero temperature lines are 150 mm apart (Table 4, Types A-1 and A-2).

In the corner section of the basement slab with a column, the minimum floor temperature is observed in the corner between the column and the external wall and amounts only to +0.13 °C with the use of a perforated beam and +0.25 °C with the use of a lightweight concrete thermal insert, which is significantly below the dew point (Table 5, Types B-1 and B-2).

Particularly in these sections with the column, the thermal bridge in the form of the column has a significant influence on the temperature regime inside the structure. At a distance of 0.6 m from the column at the junction of the external wall to the basement slab, the minimum floor surface temperature is +12.5 °C when a perforated beam outside the support is used and +12.2 °C in case of a thermal insert made of lightweight concrete.

• **Energy-efficient solutions with external heat insulation of the basement slab**

The external heat insulation of the basement slab, along with the thermal break between the raft and the slab, significantly improves the thermal protection of all structural fragments under consideration. In the outermost sections of the basement slab with the column and the external wall, the thermal break between the raft and the slab completely excludes the concrete block masonry from the thermal bridge, which is confirmed by the heat flow distribution. The thermal protection of the building in these sections has no breaks, which has a positive effect on the temperature distribution inside the enclosing structures.

In the row section of the basement floor, the minimum floor temperature is +11.88 °C, which is higher than the dew point. The zero temperature line is in the external heat insulation layer of the basement floor (Table 4, Types A-3). When external basement floor heat insulation is used, the zero temperature line is shifted outwards and is far away from the

inner surface at a distance of 320–340 mm. This is facilitated by the presence of a thermally conductive element in the form of a reinforced concrete slab on the inner side, which can be clearly seen in the heat flow distribution pattern within the structure (Table 4, Type A-3 and Table 5, Type B-3).

In the problematic corner section of the basement floor with the column and adjacent external walls, the minimum floor temperature rises to +4.80 °C, which is significantly higher compared to the temperature on the inner surface of the standard design. However, this temperature value is below the dew point. In the corner section of the basement floor, the presence of a through thermal bridge in the form of a reinforced concrete column with a cross-section of 600×600 mm has a negative impact on the temperature regime. The zero temperature line is at a significant distance from the floor — 320 mm (Table 5, Type B-3).

Discussion

The results of heat transfer modeling in different designs of basement slab sections showed that the use of a thermal break between the raft and the basement slab is crucial for reducing heat losses through the basement floor. In case of internal heat insulation of the basement slab, the formation of thermal breaks in the raft and wall masonry does not lead to a significant improvement in thermal protection. Compared to the standard design, heat losses through the row section of the basement floor with the column and the external wall are reduced by only 5.1–14.3 %, through the corner section — by 4.1–13.9 % (Fig. 7).

The use of external heat insulation of the basement slab together with the thermal break in the raft significantly reduces heat losses through all the sections considered. Compared to standard solutions, heat losses are reduced (Fig. 7):

- through the row section of the slab with the column of the outermost rows and the external wall — by 20.9 %;

- through the corner section of the slab with the column of the outermost rows and two adjacent walls — by 33.6 %.

At the design outside air temperature of –52.0 °C, the minimum temperature in the corner section with the use of external heat insulation of the basement floor and a thermal break in the raft is significantly lower than the dew point, which results in condensate formation (Table 5, Type B-3). To improve the situation, the option of shifting the column from the edge of the basement slab inward was considered. In this case, the thermal bridge in the form of a reinforced concrete column is completely eliminated in the corner area. When the column is displaced by 600 mm, the temperature on the floor in the corner between the adjacent external walls is $t_{\min} = +13.6$ °C, the temperature in the corner between the column

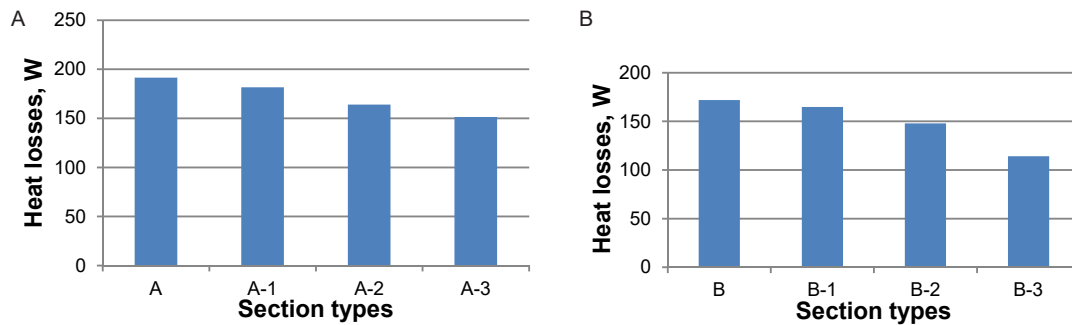


Fig. 7. Heat losses through the section of the slab with the column of the outermost rows (A) and the corner section of the slab (B)

Table 6. Results of heat transfer modeling in the corner section of the basement slab with the column displacement from the edge of the basement slab

Temperature distribution in the vertical section along the inner surface of the wall	
Displacement of 600 mm: $t_{1min} = +13.6\text{ }^{\circ}\text{C}$ and $t_{2min} = +9.5\text{ }^{\circ}\text{C}$; $L = 350\text{ mm}$	Displacement of 1200 mm: $t_{1min} = +14.8\text{ }^{\circ}\text{C}$ and $t_{2min} = +9.6\text{ }^{\circ}\text{C}$; $L = 360\text{ mm}$

and the wall is $t_{2min} = +9.5\text{ }^{\circ}\text{C}$, and when displaced by 1200 mm: $t_{1min} = +14.8\text{ }^{\circ}\text{C}$ and $t_{2min} = +9.6\text{ }^{\circ}\text{C}$ (Table 6).

Conclusion

The specifics of constructing multi-story cast-in-situ frame buildings in permafrost soils is related to massive thermal bridges in the basement part and cold ventilated under-floor space. In the period of especially low outside air temperatures of $-45\text{ }^{\circ}\text{C}$ and below, a significant difference of air pressure on the inner and outer surface of the enclosing structures on the lower floors of more than 100 Pa leads to intensive infiltration processes. As a result of heat engineering analysis of standard design of the basement part of cast-in-situ frame buildings, it was shown that the main cause of low temperature on the inner surface of the enclosing structures is the presence of extensive through thermal bridges: reinforced concrete raft — basement slab — column — concrete block masonry. In this case, the cross-section of the reinforced concrete column has a greater negative effect. There is also a rupture of thermal protection in the connections between the external wall and the basement slab.

To reduce the influence of thermal bridges in the basement part of buildings, several options of structural solutions with internal and external heat insulation of the basement slab were proposed. The results of heat engineering analysis showed that external heat insulation of the basement floor with a thermal break between the raft and the basement slab is the most efficient for thermal protection of cast-in-situ frame buildings on pile foundations. Compared to the standard solutions, heat losses through the row section of the floor with the column of the outermost rows and external wall were reduced by 20.9 %, through the corner section of the floor with the column of the outermost rows and two adjacent walls — by 33.6 %. To improve the temperature regime in the corner section of the basement floor, it is recommended to locate the columns at the ends of the building with the inward displacement from the edge of the slab.

Funding: comprehensive research project “Development of scientifically-substantiated solutions in the design, construction, and operation of Arctic settlements meeting modern standards of sustainable development and comfortable living. Stage 1” (SC No. 8019).

References

- Aghasizadeh, S., Kari, B. M., and Fayaz R. (2022). Thermal performance of balcony thermal bridge solutions in reinforced concrete and steel frame structures. *Journal of Building Engineering*, Vol. 48, 103984. DOI: 10.1016/j.job.2021.103984.
- Alhawari, A. and Mukhopadhyaya P. (2018). Thermal bridges in building envelopes – An overview of impacts and solutions. *International Review of Applied Sciences and Engineering*, Vol. 9, Issue 1, pp. 31–40. DOI: 10.1556/1848.2018.9.1.5.
- Castro-Alvarez, F., Vaidyanathan, S., Bastian, H., and King, J. (2018). *The 2018 International Energy Efficiency Scorecard*. [online] Available at: <https://www.aceee.org/sites/default/files/publications/researchreports/i1801.pdf> [Date accessed February 18, 2024].
- Citterio, M., Cocco, M., and Erhorn-Kluttig, H. (2008). *Thermal bridges in the EBPD context: overview on MS approaches in regulations*. [online] Available at: https://build-up.ec.europa.eu/sites/default/files/P064_EN_ASIEPI_WP4_IP1_p3073.pdf [Date accessed February 18, 2024].
- Danilov, N. D., Sobakin, A. A., Semyonov, A. A., and Fedotov, P. A. (2012). *Patent RU117943U1. Wall and monolithic floor covering assembly over cool or ventilated underground*.
- Evola, G. and Gagliano, A. (2024). Experimental and numerical assessment of the thermal bridging effect in a reinforced concrete corner pillar. *Buildings*, Vol. 14, Issue 2, 378. DOI: 10.3390/buildings14020378.
- François, A., Ibos, L., Feuillet, V., and Meulemans, J. (2019). Building thermal bridge heat losses quantification by infrared thermography. Steady-state evaluation and uncertainty calculation. *Journal of Physics: Conference Series*, Vol. 1343, 012171. DOI: 10.1088/1742-6596/1343/1/012171.
- Fuchs, M. (2022). Conductive heat transfer in thermal bridges. *Encyclopedia*, Vol. 2, Issue 2, pp. 1019–1035. DOI: 10.3390/encyclopedia2020067.
- Gagarin, V. G. and Dmitriev, K. A. (2013). Consideration of heat engineering heterogeneities in the analysis of thermal protection of enclosing structures in Russia and European countries. *Construction Materials*, No. 6, pp. 14–16.
- Gagarin, V. G. and Kozlov, V. V. (2010). Theoretical prerequisites for calculating the reduced resistance to heat transfer of enclosing structures. *Construction Materials*, No. 12, pp. 4–12.
- Gagarin, V. G., Kozlov, V. V., Lushin, K. I., and Plyushchenko, N. Yu. (2016). Accounting of heat-conducting inclusions and a ventilated layer when calculating the resistance to heat transfer of a wall with hinged façade system (HFS). *Construction Materials*, No. 6, pp. 32–35.
- Gushchin, S. V., Seminenko, A. S., and Shen, C. (2020). Global trends in the development of energy-saving technologies. *Bulletin of BSTU named after V.G. Shukhov*, No. 5, pp. 31–43. DOI: 10.34031/2071-7318-2020-5-5- 31-43.
- Ingeli, R. (2018a). *Analysis of atypical thermal bridges by a 3D method*. [online] Available at: https://www.researchgate.net/publication/329916337_Analysis_of_atypical_thermal_bridges_by_a_3D_method [Date accessed February 18, 2024].
- Ingeli, R. (2018b). *Detection of thermal bridges in the building*. [online] Available at: https://www.researchgate.net/publication/329916338_Detection_of_thermal_bridges_in_the_building [Date accessed February 18, 2024].
- Kang, E., Kim, D., Lee, H., and Yoon, J. (2021). In-situ thermal bridge evaluation of a building using bayesian inference with measured infrared thermography. *Journal of Energy Resources Technology*, Vol. 144, Issue 7, 070905. DOI: 10.1115/1.4052858.
- Kim, M.-Y., Kim, H.-G., Kim, J.-S., and Hong, G. (2022a). Investigation of thermal and energy performance of the thermal bridge breaker for reinforced concrete residential buildings. *Energies*, Vol. 15, Issue 8, 2854. DOI: 10.3390/en15082854.
- Kim, H., Kim, J., and Yeo, M. (2022b). Thermal bridge modeling according to time-varying indoor temperature for dynamic building energy simulation using system identification. *Buildings*, Vol. 12, Issue 12, 2178. DOI: 10.3390/buildings12122178.
- Kim, H. and Yeo, M. (2020). Thermal bridge modeling and a dynamic analysis method using the analogy of a steady-state thermal bridge analysis and system identification process for building energy simulation: methodology and validation. *Energies*, Vol. 13, Issue 17, 4422. DOI: 10.3390/en13174422.
- Kornilov, T. A. and Ambrosyev, V. V. (2008). Specifics of ventilated facade operation under conditions of steady low temperature based on the results of a field experiment. *Housing Construction*, No. 1, pp. 32–35.
- Kornilov, T. A., Fedotov, P. A., Nazarov, T. A., and Vasilyeva, A. T. (2022). *Patent RU2780187C1. Method for constructing a basement floor unit with a column over cold and ventilated undergrounds*.
- Kornilov, T., Fedotov, P., and Nikiforov, A. (2021). Evaluation of the effectiveness of additional thermal insulation of the basement floor of frame-monolithic buildings in extreme operating conditions. *E3S Web of Conferences*, Vol. 263, 04041. DOI: 10.1051/e3sconf/202126304041.
- Kornilov, T. A., Kardashevsky, A. G., and Kychkin, I. R. (2017). *Patent RU170253U1. The junction of the building envelope and basement over cold and ventilated undergrounds*.
- Kornilov, T. A. and Vasilyeva, A. T. (2022). Heat losses through the coupling of three-layer walls with reinforced concrete floors. *Industrial and Civil Engineering*, No. 8, pp. 25–31. DOI: 10.33622/0869-7019.2022.08.25-31.

- Li, B., Guo, L., Li, Y., Zhang, T., and Tan, Y. (2018a). Partial insulation of aerated concrete wall in its thermal bridge regions. *IOP Conference Series: Earth and Environmental Science*, Vol. 108, Issue 2, 022068. DOI: 10.1088/1755-1315/108/2/022068.
- Li, B., Guo, L., Li, Y., Zhang, T., and Tan, Y. (2018b). Thermal bridge effect of aerated concrete block wall in cold regions. *IOP Conference Series: Earth and Environmental Science*, Vol. 108, Issue 2, 022041. DOI: 10.1088/1755-1315/108/2/022041.
- Mayer, Z., Heuer, J., Volk, R., and Schultmann, F. (2021). Aerial thermographic image-based assessment of thermal bridges using representative classifications and calculations. *Energies*, Vol. 14, Issue 21, 7360. DOI: 10.3390/en14217360.
- Theodosiou, T., Tsikaloudaki, K., Kontoleon, K., and Giarma, C. (2021). Assessing the accuracy of predictive thermal bridge heat flow methodologies. *Renewable and Sustainable Energy Reviews*, Vol. 136, 110437. DOI: 10.1016/j.rser.2020.110437.
- Tusnina, O. A., Emelianov, A. A., and Tusnina, V. M. (2013). Thermal insulation properties of various ventilated facade systems. *Magazine of Civil Engineering*, No. 8 (43), pp. 54–63.
- Umnyakova, N. P., Andreytseva, K. S., and Smirnov, V. A. (2013a). The engineering method of calculating the temperature in the outer wall, monolithic floor and balcony slab interface with use of load-bearing heat-insulating element Shoock Isokorb. *Building and Reconstruction*, No. 6 (50), pp. 53–64.
- Umnyakova, N. P., Egorova, T. S., Andreytseva, K. S., Smirnov, V. A., and Lobanov, V. A. (2013b). New structural solution for the junction of exterior walls with cast-in-situ floor and balcony slabs. *Construction Materials*, No. 6, pp. 28–31.
- Umnyakova, N. P., Egorova, T. S., Cherkas, V. E., Belogurov, P. B., and Andreytseva, K. S. (2012). Improving the energy efficiency of buildings by increasing the heat engineering homogeneity of exterior walls in the area of contact with balcony slabs. *Construction Materials*, No. 6, pp. 17–19.
- Zhang, X., Jung, G.-J., and Rhee, K.-N. (2022). Performance evaluation of thermal bridge reduction method for balcony in apartment buildings. *Buildings*, Vol. 12, Issue 1, 63. DOI: 10.3390/buildings12010063.

СНИЖЕНИЕ ВЛИЯНИЯ ТЕРМИЧЕСКИХ МОСТОВ ЦОКОЛЬНОЙ ПЛИТЫ КАРКАСНО-МОНОЛИТНЫХ ЗДАНИЙ В ЭКСТРЕМАЛЬНО ХОЛОДНЫХ РАЙОНАХ

Терентий Афанасьевич Корнилов*, Петр Анатольевич Федотов, Алексей Терентьевич Корнилов

Северо-Восточный федеральный университет имени М. К. Аммосова, Российская Федерация

*E-mail: kornt@mail.ru

Аннотация

Введение. Обеспечение теплозащиты многоэтажных зданий с железобетонным каркасом на свайных фундаментах в климатических условиях с экстремально низкой температурой наружного воздуха усложняется высокой инфильтрацией воздуха. При эксплуатации таких зданий в зимний период наиболее характерными являются нарушения температурного режима на первом этаже. **Цель:** оценка различных методов снижения влияния термических мостов в цокольном перекрытии каркасно-монолитного здания со свайными фундаментами в экстремальных климатических условиях. **Методы:** Теплотехнические характеристики 3D моделей ограждающих конструкций определены с использованием сертифицированной программы HEAT3. Рассмотрены варианты внутренней и наружной теплоизоляции цокольного перекрытия с термическими разрывами в конструкциях. **Результаты:** В результате численного анализа типовых решений цокольных перекрытий зданий установлено, что низкая температура на внутренней поверхности и значительные тепловые потери связаны с наличием сквозных термических мостов: железобетонный ростверк – цокольная плита – колонна – кладка из бетонных блоков. Наиболее эффективным для тепловой защиты каркасно-монолитных зданий является наружная теплоизоляция цокольного перекрытия с термическим разрывом в ростверках. По сравнению с типовым решением тепловые потери через угловой участок перекрытия со смещенной колонной снижаются на 33,6 %, а минимальная температура на внутренней поверхности выше температуры точки росы.

Ключевые слова: термический мост, цокольное перекрытие, терморазрыв, колонна, ростверк.

A COMPARISON OF SHEAR STRENGTH CALCULATION METHODS FOR PERFOBOND LEISTE SHEAR CONNECTORS USING THE CONTROLLED VARIABLE METHOD

Xu Yun¹, Chen Bin^{1*}, Wang Xuejiao², Liu Yingxin¹, Wang Heng³, Aleksandr Chernykh⁴, Egor Danilov⁴, Pavel Koval⁴, Du Mingli¹, Zhang Zhonghua¹, Shi Saisai¹, Song Chunbo¹

¹School of Civil Engineering and Communication, North China University of Water Resources and Electric Power, Zhengzhou, People's Republic of China

²School of International Education, Zhengzhou Railway Vocational and Technical College, Zhengzhou, People's Republic of China

³Architectural Design Corporation Limited, Beijing, People's Republic of China

⁴Saint Petersburg State University of Architecture and Civil Engineering, Saint Petersburg, Russia

*Corresponding author's email: chenbncwu@163.com

Abstract: This paper provides a brief overview of the current research on timber-concrete composite beams and PBL shear connectors. Five representative calculation formulas were selected, and the effects of concrete strength and opening diameter on the ultimate bearing capacity of shear connectors were compared and analyzed using the controlled variable method. This study can serve as the basis for further optimizing the design parameters of composite beams.

Keywords: timber-concrete composite beam; PBL shear connector; shear capacity calculation method; design optimization.

Introduction

The Perfobond Leiste (PBL) shear connector consists of a perforated steel plate, concrete tenon, and through steel reinforcement. The PBL shear connector has become the most promising connector due to its high shear stiffness, high bearing capacity, good fatigue resistance, and convenient construction. da C. Vianna et al. (2013) analyzed PBL shear key composite structures experimentally and discovered that the thickness of the steel plate had a significant impact on the anti-slip performance of the shear key. Yang and Chen (2018) conducted monotonic loading push-out tests on PBL connectors and found that the end-bearing type specimens had higher shear bearing capacity and shear stiffness than the non-end-bearing type specimens. Huang et al. (2021) introduced a new type of bent-through steel reinforcement PBL shear key and conducted push-out tests, which revealed that bent-through steel reinforcement could effectively enhance the ductility of PBL shear keys and extend the service life of structures. Zhao et al. (2015) utilized ANSYS 12.0, a large-scale nonlinear finite element analysis software, to investigate the impact of parameters such as concrete grade and diameter of penetrating rebars on the stress distribution and shear bearing capacity of PBL shear keys. This study emphasized the significant influence of factors such as rebar diameter, concrete strength grade, and the bond strength between concrete and steel plate on shear bearing capacity. Zhu and Wang (2016) conducted experimental research on PBL shear keys in steel-

concrete composite beam bridges, considering the effect of transverse prestressing. It proved that increasing the diameter of penetrating rebars, the aperture size of steel plate openings, and the thickness of the steel plate effectively increases the shear bearing capacity of PBL shear keys. However, it also noted that the introduction of transverse prestressing accelerated concrete cracking, which limited the full utilization of the potential strength and stiffness of concrete, steel plates, and penetrating rebars, thereby reducing the bearing capacity of PBL shear keys. Cui et al. (2017) conducted a statistical analysis on the load-slip curves of single-hole PBL connectors, which included 22 groups without penetrating rebars and 21 groups with penetrating rebars. According to them, in the plastic phase, the residual shear bearing capacity of single-hole PBL connectors results from the combined effects of bonding force along the shear failure surface of the concrete tenon, the shear bearing capacity provided by lateral restraint, and the anchoring effect of penetrating rebars. Zhao et al. (2018) conducted push-out tests on wave-shaped PBL connectors, varying the diameter of the penetrating rebars. It was found that beyond a certain rebar diameter, the rate of increase in the connector's shear bearing capacity started to decrease. Shi (2019) performed comprehensive experimental research and finite element simulations on lightweight aggregate concrete PBL shear connectors. The research highlighted that the shear bearing capacity of these connectors is mainly influenced by concrete strength,

opening size, and rebar diameter. A formula for calculating the ultimate bearing capacity of lightweight aggregate concrete PBL shear connectors was proposed. Wang (2020) investigated the impact of additional constraints on the bearing mechanism of PBL shear connectors. It was shown that such factors as restraining rebars and friction between the specimen and the test base had a significant effect on the failure mode, rebar strain, and load-slip curve of PBL connectors. Furthermore, a method for calculating the bearing capacity of PBL connectors was proposed, taking into account the influence of these additional constraints. Xue et al. (2020) applied finite element analysis to conduct push-out tests on perforated plate connectors. They highlighted the significant influence of both yield strength and rebar diameter on the ultimate shear bearing capacity of these connectors. This study demonstrated a linear relationship, where increased yield strength and rebar diameter led to enhanced shear bearing capacity. Zhang (2021) conducted static push-out tests on 16 U-shaped PBL shear keys across four groups of specimens. Zhang noted that the ultimate bearing capacity of these shear keys was mainly determined by the compressive concrete at the end steel plate, along with the penetrating rebars and concrete tenon. Liao (2022) conducted push-out tests and finite element analysis on UHPC-reinforced PBL connectors. The tests indicated that the use of UHPC approximately doubled the bearing capacity and increased shear stiffness by about 1.75 times. They also confirmed the accuracy of the nonlinear finite element analysis. Ren (2023) conducted a lateral bending static test with varying diameters of perforated rebars. Ren stated that the diameter of the perforated rebars had a relatively minor impact on the failure mode of T-PBL connector specimens. It was suggested that the current industry standard for calculating the lateral bending bearing capacity of T-PBL connectors might be relatively conservative. Yang et al. (2024) conducted push-out tests on bolted PBL connectors in waveform steel-UHPC composite bridge decks, along with finite element analysis of beam tests. This study illustrated that increasing the diameter of short bolts, PBL aperture, and UHPC strength effectively increases the shear bearing capacity of the composite connectors. A modern timber-concrete composite structure is a novel construction that combines wood and concrete materials. By combining wood and concrete flanges with shear connectors, the corresponding good tensile and compressive properties can be fully utilized, effectively transferring longitudinal shear forces and preventing the separation of the wood beams and concrete flanges. Modern timber-concrete composite beams have significantly higher overall integrity, bending stiffness, and fire resistance compared to traditional timber beams. PBL shear

connectors have been widely used in timber-concrete composite structures. Many researchers have conducted experimental and theoretical studies on mechanical performance. Schanack et al. (2015) conducted shear, static, and numerical tests on timber-concrete composite beams and compared the numerical results with the experimental ones. It was found that the finite element model could better predict the test results. Li (2017) conducted static tests and numerical simulations on glued laminated timber composite beam bridges, and demonstrated that the support type influenced the beam end slip. Yuan (2019) investigated the bearing capacity of modern timber-concrete composite beam bridges and proposed a formula for bending resistance. The numerical results agreed with the theoretical ones. Kim et al. (2014) conducted static load tests on composite beams with Y-shaped PBL shear keys and demonstrated that Y-shaped PBL shear keys had higher stiffness and ultimate loads than traditional ones.

There is no unified design theory or method for calculating the shear capacity of PBL shear connectors. In the course of this study, five representative calculation formulas were selected and combined with the load characteristics of PBL shear connectors. Using the controlled variable method, the effects of concrete compressive strength and aperture diameter on the shear capacity of PBL connectors were compared and analyzed using different calculation equations. The design parameters of composite beams were also optimized. The research results can serve as a reference for the design of modern timber-concrete composite beam bridges and for optimizing PBL shear connector designs.

Calculation Methods

(1) The Specifications for the Design of Highway Steel Bridges (JTG D64-2015) (Ministry of Transport of the People's Republic of China, 2015) provide a calculation equation for the shear bearing capacity of PBL shear connectors. This equation mainly takes into account the shear resistance of concrete keys and the effect of penetrating steel bars.

$$V_{up} = 1.4(d^2 - d_s^2)f_c + 1.2d_s^2f_{sd}, \quad (1)$$

where:

V_{up} — ultimate shear capacity of the connection, N;

d — diameter of the opening, mm;

d_s — diameter of the penetrating reinforcement, mm;

f_c — design value of the compressive strength of concrete at the centroid, MPa;

f_{sd} — design value of the tensile strength of the penetrating reinforcement, MPa.

(2) Eurocode 4 (European Committee for Standardization, 2004) provides specific calculation

formulas that account for the influence of through-bars and concrete, based on a statistical analysis of a large number of test results.

$$V_{up} = \left[1.85 \left(\frac{\pi(d^2 - d_s^2)f_c}{4} + \frac{\pi d_s^2 f_{sd}}{4} \right) - 106.1 \cdot 10^3 \right] \quad (2)$$

(3) Hu et al. (2006) derived a calculation formula for the bearing capacity of the connection member consisting of transverse ordinary steel bars, penetrating steel bars, and concrete tenons.

$$V_{up} = \frac{\alpha \pi d_s^2 f_y}{4} + \beta A'_{tr} f'_y + \frac{\gamma \pi (d^2 - d_s^2) \sqrt{f_c}}{4} \quad (3)$$

where:

α — coefficient of influence of the penetrating steel bar, taken as 1.32;

f_y — yield strength of the penetrating steel bar, MPa;

β — coefficient of influence of the transverse steel bar, taken as 1.204479;

A'_{tr} — sectional area of hoop reinforcement, mm²;

f'_y — yield strength of hoop reinforcement, MPa;

γ — coefficient of influence of concrete keys, taken as 1.95.

(4) Zheng et al. (2016) derived a calculation formula for the connection capacity of PBL shear connectors, which takes into account the contributions of the end concrete, hole concrete, and penetrating steel bars. Their formula was based on the experimental results.

$$V_{up} = 1.76 \alpha_A \left(\frac{\pi d^2}{4} - \frac{\pi d_s^2}{4} \right) f_c + 1.58 \frac{\pi d_s^2}{4} f_y; \quad (4)$$

$$\alpha_A = 3.8 \left(\frac{d_s^2}{d^2} \right)^{2/3},$$

where: α_A reflects the restraining effect of the penetrating steel bars on the concrete in the hole.

Yang and Chen (2018) argued that the compressive action of the concrete at the end of the perforated plate, the shear resistance of the concrete in the hole, and the shear resistance of the penetrating steel bar are the main components of the shear bearing capacity of the PBL shear connector. The following calculation formula was derived:

$$V_{up} = 5.15 h t f_{cu} + 5.41 \left(\frac{\pi d^2}{4} - \frac{\pi d_s^2}{4} \right) f_{cu}^{0.57} + 2.24 \frac{\pi \times d_s^2}{4} f_y, \quad (5)$$

where:

f_{cu} — compressive strength of concrete in cubic form, MPa;

h — height of the perforated plate, mm;

t — thickness of the perforated plate, mm.

Comparison and Analysis

To compare the effects of concrete compressive strength and opening diameter on the shear bearing capacity of PBL shear connectors using different calculation formulas, Eqs. (1)–(5) were used, and a PBL opening diameter of 50 mm was selected. The relationship between the concrete compressive strength and the shear bearing capacity of PBL shear connectors is presented in Fig. 1. The relationship between the opening diameter and shear bearing capacity of PBL shear connectors is clear from Fig. 2, when a concrete cube compressive strength of 40 MPa is selected.

As shown in Figs. 1 and 2, the relationship between the concrete compressive strength, opening diameter, and PBL shear capacity exhibits a linear positive correlation among Eqs. (1)–(5). The shear capacity calculated by Eqs. (1) to (4) mainly ranges

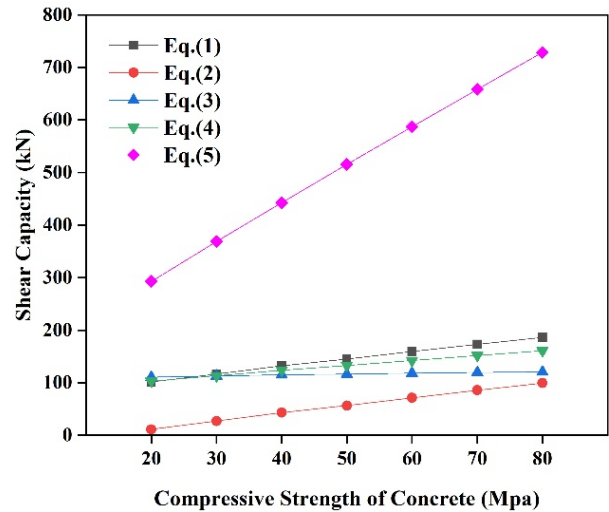


Fig. 1. Relationship between the concrete compressive strength and the shear bearing capacity of PBL shear connectors

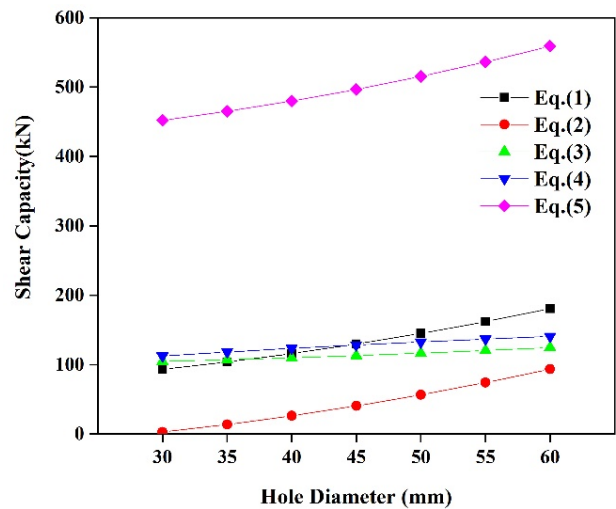


Fig. 2. Relationship between the opening diameter and the shear bearing capacity of PBL shear connectors

around 100 kN, while the shear capacity calculated by Eq. (5) is much higher than that of other formulas, with a maximum difference of 629 kN. Yang and Chen (2018) explained that Eq. (5) accounts for the compressive action at the end of the perforated plate, while other formulas only account for the shear resistance of the concrete tenon and the penetrating steel bar, neglecting the compressive action of the end concrete. Furthermore, the slopes of the curves obtained by calculating Eqs. (1), (3), and (5) are relatively gentle, indicating that the calculated shear capacity is less sensitive to the concrete compressive strength and opening diameter. In summary, the shear capacity calculated by Eqs. (2) and (5) deviates considerably from other calculation formulas. Given the general nature of the calculation method, it is important to specifically consider the applicability of the formulas in the design of modern timber-concrete composite beam bridges and in the optimization of PBL shear connector design. Alternatively, Eqs. (1), (3), and (4) can be used for calculation to prevent significant errors in the results. As a result, some suggestions for the optimal use of the formulas are shown below:

- Eqs. (1) and (3) are suitable for estimating the shear capacity of PBL shear connectors with low concrete compressive strength and small opening diameter, as they are relatively conservative and stable.

- Eq. (4) is suitable for estimating the shear capacity of PBL shear connectors with moderate concrete compressive strength and opening diameter, as it is close to the average value of other formulas.

Conclusions

In the course of this study, five representative calculation formulas were selected and combined with the load characteristics and test data of PBL shear connectors. The study analyzed the effects of concrete strength and aperture diameter on the ultimate bearing capacity of the connectors using the controlled variable method. The main conclusions were as follows: concrete strength and aperture diameter had a significant impact on the shear capacity of Eqs. (2) and (5), but a minor impact on the other three formulas. Concrete strength had a significant impact on Eq. (4), while the impact of aperture diameter was not significant and requires further verification by increasing the variables. The calculation results using Eq. (5) indicate that the compressive effect at the end of the perforated plate might cause a significant deviation in the calculated bearing capacity, which could affect the evaluation of the shear capacity of PBL connectors.

Funding

This research work was jointly supported by: Annual Project of Henan Province Philosophy and Social Sciences Planning (grant No. 2023BZH004); Training Program for Young Backbone Teachers of Undergraduate Colleges and Universities in Henan Province (grant No. 2023GGJS075); Research Project of Colleges and Universities in Henan Province (grant No. 23A560007); Research Project of Zhengzhou Railway Vocational and Technical College (Social Sciences) (grant No. 2023KY031).

Funding acquisition: Xu Yun, Wang Xuejiao.

References

- Cui, Y., Zhu, W., and Liu, Y. (2017). Shear resistance mechanism and load-slip curve features of perfbond rib connectors during plastic stage. *Journal of Building Structures*, 2017, Vol. 38, Issue S1, pp. 315–323. DOI: 10.14006/j.zjgxb.2017.S1.044.
- da C. Vianna, J., de Andrade, S. A. L., da S. Vellasco, P. C. G., and Costa-Neves, L. F. (2013). Experimental study of Perfbond shear connectors in composite construction. *Journal of Constructional Steel Research*, Vol. 81, pp. 62–75. DOI: 10.1016/j.jcsr.2012.11.002.
- European Committee for Standardization (2004). *Eurocode 4: Design of composite steel and concrete structures. Part 1-1: General rules and rules for buildings*. Brussels: European Committee for Standardization, 118 p.
- Hu, J., Ye, M., and Huang, Q. (2006). Experiment bearing capacity of PBL shear connectors. *China Journal of Highway and Transport*, Vol. 6, pp. 65–72.
- Huang, C., You, W., Tan, J., Yang, Y., and Gan, S. (2021). Experimental on mechanical properties of PBL shear connector with bent passing rebar. *Journal of Civil Engineering and Management*, Vol. 38, No. 6, pp. 113–120.
- Kim, S.-H., Choi, J., Park, S.-J., Ahn, J.-H., and Jung, C.-Y. (2014). Behavior of composite girder with Y-type perfbond rib shear connectors. *Journal of Constructional Steel Research*, Vol. 103, pp. 275–289. DOI: 10.1016/j.jcsr.2014.09.012.
- Liao, X. (2022). *Research on static and fatigue properties of PBL shear connectors in UHPC*. Master Degree Thesis.
- Li, L. (2017). *The research on the overall performance of LVL-concrete composite beam bridge*. Master Degree Thesis.
- Ministry of Transport of the People's Republic of China (2015). *People's Republic of China Industry Standard. JTG D64-2015. Specifications for the Design of Highway Steel Bridges*. People's Transportation Publishing House, pp. 1-70.
- Ren, X. (2023). Study on transverse bending behavior of twin perfbond rib shear connectors in composite girder bridge with corrugated steel webs. *Bridge Construction*, Vol. 53, No. 4, pp. 87–93. DOI: 10.20051/j.issn.1003-4722.2023.04.012.
- Schanack, F., Ramos, O. R., Reyes, J. P., and Low, A. A. (2015). Experimental study on the influence of concrete cracking on timber concrete composite beams. *Engineering Structures*, Vol. 84, pp. 362–367. DOI: 10.1016/j.engstruct.2014.11.041.
- Shi, L. (2019). *Experimental study on shearing capacity of lightweight aggregate concrete PBL connector*. Master Degree Thesis.
- Wang, F. (2020). *Research on the influence of additional constraints in push-out test on the bearing mechanism of perfbond shear connectors*. Master Degree Thesis.
- Xue, D., Huang, Y., Wan, Q., and Zhang, Y. (2020). Nonlinear analysis of the influence of perforated rebar on the shear capacity of perfbond rib shear connector. *Industrial Construction*, Vol. 50, No. 11, pp. 65–70. DOI: 10.13204/j.gjz201904290005.
- Yang, Y. and Chen, Y. (2018). Experimental study on the shear capacity of PBL shear connectors. *Engineering Mechanics*, Vol. 35, No. 9, pp. 89–96. DOI: 10.6052/j.issn.1000-4750.2017.05.0365.
- Yang, X., He, J., Hu, D., Xiao, B., and Wang, N. (2024). Numerical study on shear performance of stud-PBL shear connector in corrugated steel plate-UHPC layer composite deck. *Journal of Railway Science and Engineering*, Vol. 21, No. 2, pp. 697–708.
- Yuan, S. (2019). *Study on design of flexural capacity of modern timber-concrete composite beam bridge*. Master Degree Thesis.
- Zhang, Q. (2021). *Research on shear performance of U-shaped PBL shear connectors*. Master Degree Thesis.
- Zhao, W., Chen, D., Bao, L., and Yu, L. (2015). Study on mechanical behavior of the PBL shear connector and its bearing capacity influence factors. *Journal of Shenyang Jianzhu University (Natural Science)*, Vol. 31, No. 5, pp. 864–871. DOI: 10.11717/j.issn:2095-1922.2015.05.12.
- Zhao, H., Li, M., and Zhu, X. (2018). Research on influence of through rebar to corrugated PBL connector. *Journal of University of South China (Science and Technology)*, Vol. 32, No. 6, pp. 22–27.
- Zheng, S., Liu, Y., Yoda, T., and Lin, W. (2016). Parametric study on shear capacity of circular-hole and long-hole perfbond shear connector. *Journal of Constructional Steel Research*, Vol. 117, pp. 64–80. DOI: 10.1016/j.jcsr.2015.09.012.
- Zhu, B. and Wang, X. (2016). Experimental study on PBL shear connectors of steel-concrete composite bridge considering transverse prestressing. *Journal of Southwest Jiaotong University*, Vol. 51, No. 4, pp. 621–631.

СРАВНЕНИЕ МЕТОДОВ РАСЧЕТА ПРОЧНОСТИ НА СДВИГ СОЕДИНИТЕЛЬНЫХ ЭЛЕМЕНТОВ PERFOBOND LEISTE, РАБОТАЮЩИХ НА СДВИГ, С ИСПОЛЬЗОВАНИЕМ МЕТОДА КОНТРОЛИРУЕМЫХ ПЕРЕМЕННЫХ

Сюй Юнь¹, Чэнь Бинь^{1*}, Ван Сюэцзяо², Лю Инсинь¹, Ван Хэн³, Александр Черных⁴, Егор Данилов⁴, Павел Коваль⁴, Ду Минли¹, Чжан Чжунхуа¹, Ши Сайсай¹, Сун Чуньбо¹

¹Факультет гражданского строительства и коммуникаций, Северо-китайский университет водных ресурсов и электроэнергетики, Чжэнчжоу, Китайская Народная Республика

²Факультет международного образования, высшее профессионально-техническое железнодорожное училище Чжэнчжоу, Чжэнчжоу, Китайская Народная Республика

³Architectural Design Corporation Limited, Пекин, Китайская Народная Республика

⁴Санкт-Петербургский государственный архитектурно-строительный университет, Санкт-Петербург, Россия

*E-mail: chenbncwu@163.com

Аннотация: В данной статье представлен краткий обзор современных исследований составных деревобетонных балок и соединительных элементов PBL, работающих на сдвиг. Выбраны пять репрезентативных расчетных формул, проведены сравнение и анализ влияния прочности бетона и диаметра отверстия на предельную несущую способность соединительных элементов, работающих на сдвиг, с использованием метода контролируемых переменных. Данное исследование может послужить основой для дальнейшей оптимизации параметров проектирования составных балок.

Ключевые слова: составная деревобетонная балка; соединительный элемент PBL, работающий на сдвиг; метод расчета прочности на сдвиг; оптимизация конструкции.

INVESTIGATION OF THE SHEAR STRENGTH OF REINFORCED SILTY SAND

Feknous Hadjer¹, Della Noureddine^{1*}, Denine Sidali², Missoum Benziane Mehdi¹, Flitti Abdelhamid¹, Sert Sedat³, Ertan Bol³, Apkyn Ozocak³

¹Laboratory of Materials Science and Environment, Hassiba Benbouali University of Chlef, Algeria

²University Center of Tipaza, Tipaza, Algeria

³Geotechnical Laboratory Sakarya University, Sakarya, Turkey

*Corresponding author's email: n.della@univ-chlef.dz

Abstract

Introduction: This paper presents an experimental investigation that aims to study the influence of silt content, glass fiber content, and their combined effect on the shear behavior of silty sand. For this **purpose**, a series of tests using direct shear apparatus (as **methods**) were carried out on sand mixed with various silt and fiber contents. Samples were prepared with a relative density of 50 %, and each mixture was tested at three different normal stresses. The experimental **results** indicated an increase in shear strength at 10 % silt content, followed by a decrease in shear strength with increasing silt content from 10 % to 30 %. It was also found that 0.5 % is the optimal content that can be added to sand-silt mixtures to enhance their shear strength and friction angle, although the mixtures become more contractive.

Keywords: sand, silt, glass fiber, shear strength, cohesion, friction angle.

Introduction

It is widely recognized that the behavior of sand-fines mixtures, frequently encountered in nature, is largely affected by the type, plasticity, and content of the fine particles they contain. These soils can have instability problems under certain conditions due to their unfavorable geotechnical properties, which make them incapable of supporting the loads to which they are subjected. This type of soil, therefore, needs its properties enhanced to make it exploitable and suitable for construction. Soil improvement methods, widely used today, are numerous and varied. Han (2015) classified soil improvement methods according to their function into six categories: densification, replacement, drainage and consolidation, chemical stabilization, reinforcement, and thermal and biological treatment.

Geotechnical engineering has recently witnessed an increasing interest in the study of soils reinforced with randomly distributed fibers (Benziane et al., 2019; Chen and Loehr, 2008; Consoli et al., 2007; Diambra et al., 2010; Gray and Al-Refeai, 1986; Khebizi et al., 2019; Michalowski and Cermák, 2003; Benziane et al., 2022; Romero, 2003; Safdar et al., 2020; Tang et al., 2007). Various synthetic fibers are currently in use, including polypropylene, polyethylene, polyester, nylon, steel, and glass fibers (Rabab'ah et al., 2021). Glass fibers have been extensively utilized in common and demanding

applications due to their numerous advantageous features, such as high tensile strength, low fabrication costs, and superior chemical resistance (Derradji et al., 2018). The mechanical behavior of soils mixed with glass fibers has been studied by numerous researchers. Consoli et al. (1998) found that glass fiber reinforcement increases both peak and residual triaxial strengths, decreases stiffness, and changes the brittle behavior of the cemented soil to a more ductile one. Consoli et al. (2004) also found that the peak friction angle of both cemented and uncemented sand increased, and the peak cohesive intercept decreased slightly when glass fibers were added to the sand-cement mixture. According to Ahmad et al. (2012), the inclusion of randomly distributed glass fibers with soil particles creates a soil-fiber matrix that provides an interlocking effect to reinforce soil by implicitly preserving soil integrity and improving its interparticle frictional interface. By conducting direct shear tests on sand samples mixed with different percentages of glass fibers (0 %, 0.1 %, 0.3 %, and 0.5 %), Benessalah et al. (2016) found that sand containing 0.3 % fiber content generally exhibits higher shear strength and friction angle than other mixtures. Additionally, it is the most dilatant, particularly in the dense state. Bouaricha et al. (2017) found that specimens of sand mixed with glass fiber have a maximum shear strength greater than that of unreinforced soil, and that the optimal

value of the fiber content is 0.2 %. Bouaricha et al. (2017) also found that, for this optimal fiber content, adding fibers of 20 mm length gave the highest shear strength for both types of sand. The results obtained by Rabab'ah et al. (2021) showed that the addition of glass fiber to an expansive soil increases its unconfined compressive strength, indirect tensile strength, and CBR values, and decreases its swell potential. Benziane et al. (2022) found that glass fiber significantly improved the shear strength, cohesion interception, and friction angle of sand.

While there has been a significant amount of research on the mechanical behavior of granular and fine soils mixed with glass fibers, the impact of these fibers on the shear behavior of silty sands has not received as much attention as other soil types. The present study aims to investigate the shear behavior of sand mixed with different percentages of silt and glass fiber, focusing on the effect of silt content and fiber content, as well as their combined effect.

Methods and Materials

Sand-silt mixtures

The soil used in this study is sand extracted from the banks of the Chlef river, which flows through the city of Chlef to the west of Algiers. The decision to use this soil in an effort to improve it was not made randomly. Several researchers (Arab, 2009; Belkhatir et al., 2014; Della et al., 2011, 2014) showed that

the soil in this region can exhibit instability problems under certain conditions. Durville and Meneroud (1982) also reported that, during the 1980 earthquake, liquefaction phenomena had appeared in the valley of the Chlef river where the soil was located.

After collecting the sand and transporting it to the laboratory, sand particles with a diameter greater than 2 mm were removed through dry sieving. Particles smaller than 0.08 mm, which typically represent silt grains used in this study, were separated from the sand by dry sieving and washing. The clean sand and silt were then dried to a constant mass (Fig. 1).

The silty sand samples were obtained by mixing clean sand ($S_c = 0\%$) with different silt fractions ($S_c = 10\%, 20\%, \text{ and } 30\%$ by dry soil mass). Fig. 2 presents the grain size distribution curve of sand-silt mixtures, and their properties are given in Table 1.

Glass fiber

The fibers used are white glass fibers with circular cross-sections, which have a length of 12 mm and a diameter of 18 μm (Fig. 4). The physical and mechanical characteristics of fibers are presented in Table 2.

Testing procedure

To investigate the combined effect of silt and fiber reinforcement on the shear behavior of fiber-reinforced sand-silt mixture at a medium-dense state ($D_r = 50\%$), a series of 48 direct shear tests, divided

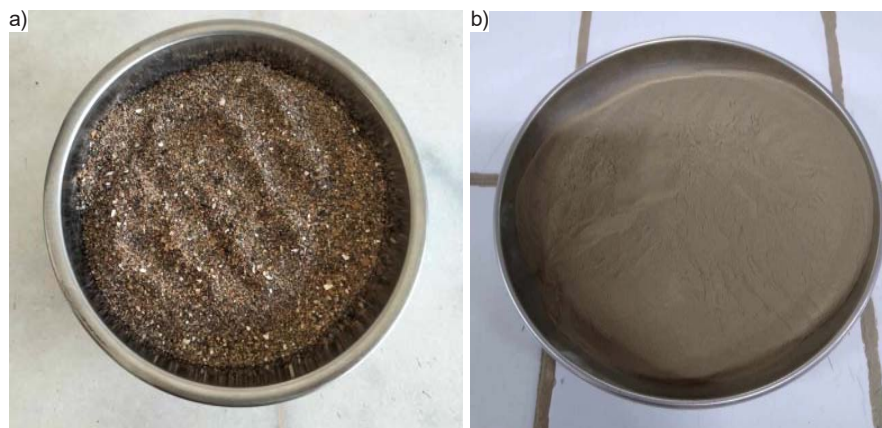


Fig. 1. Basic materials used: (a) clean Chlef sand, (b) Chlef silt

Table 1. Physical properties of sand and sand-silt mixtures

Properties	Sand	Sand-silt			Silt
		10 %	20 %	30 %	
Silt content	0 %	10 %	20 %	30 %	100 %
Uniformity coefficient C_u	2.00	5.00	13.33	21.11	–
Coefficient of curvature C_c	0.82	1.95	4.41	3.29	–
Medium size D_{50} (mm)	0.45	0.36	0.34	0.30	0.029
Maximum diameter D_{max} (mm)	2.00	2.00	2.00	2.00	0.08
Specific density G_s	2.741	2.698	2.692	2.686	2.667
Maximum void ratio e_{max}	0.91	0.81	0.77	0.76	1.563
Minimum void ratio e_{min}	0.61	0.49	0.42	0.40	0.991

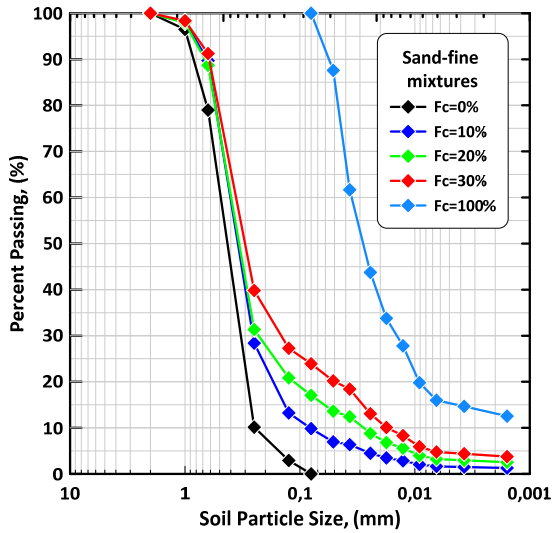


Fig. 2. Grain size distribution curve of Chlef sand-silt mixtures

into three sets, was considered for this laboratory experiment. The first set of samples was obtained by mixing clean Chlef sand with various silt fractions ($Sc = 0, 10, 20,$ and 30%) to investigate the impact of silt fractions on the behavior of the sand-silt matrix. The second set was obtained using clean Chlef sand reinforced with various fiber contents ($Fc = 0, 0.3, 0.5,$ and 0.8%) to assess the reinforcing potential of glass fibers. The final set was obtained using unreinforced and reinforced sand-silt mixtures with glass fibers to evaluate the combined effect of silt fractions and fiber contents on the shear behavior of Chlef sand.

All tests were conducted at the Laboratory of Materials Science and Environment (LMSE) at the Hassiba Benbouali University of Chlef in Algeria. This experimental study was carried out using a standard laboratory direct shear apparatus with a square box measuring 60×60 inches. Fig. 5 presents a general

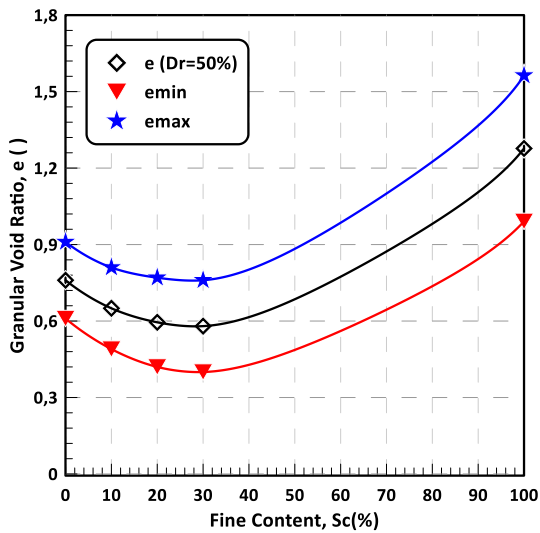


Fig. 3. Variation of the minimum and maximum void ratio as a function of fines content



Fig. 4. Glass fiber reinforcement



Fig. 5. View of the direct shear apparatus

Table 2. Glass fiber characteristics

Properties	Specific gravity	Length (m)	Diameter (mm)	Mean tensile strength (MPa)	Elastic modulus (GPa)
Glass fiber	2.62	12	18	485	73

view of the setup, showing the direct shear apparatus and the data acquisition system. Each test was repeated multiple times to ensure the reliability of the results. All the parameters considered in the testing program are listed in Table 3.

Sample preparation

The tested samples are mixtures composed of sand, silt, and glass fibers, prepared in a dry state ($w = 0\%$). The initial height of the samples is constant and equal to 2.5 mm. To determine the dry mass of the sand-silt mixture needed to fill the required volume, the initial density of the sample is proposed, and the following equations are used:

$$W_s = \frac{V_T \cdot G_s}{1 + e_{max} - Id(e_{max} - e_{min})}$$

where V_T and Id are the total sample volume and the desired density index, respectively. The fiber mass was then calculated. The fiber concentration (F_c) to be added is defined as a percentage of the dry mass of the sand-silt mixture.

Sample preparation begins by securing the half-boxes with two screws. Next, the holding plate is placed at the bottom of the shear box, followed by the grid plate. Once the masses of the constituents are determined, the sand, silt, and fibers are perfectly mixed until a homogeneous mixture is obtained (Fig. 6). This mixture is then deposited in the cavity of the shear box in three layers using the dry deposition method. To achieve the medium dense state ($Dr = 50\%$), no compaction was necessary; only the surface of each layer was leveled off.

After depositing the sample, the second grid plate is placed above it, followed by the loading piston.



Fig. 6. Sand-silt-fiber mixtures

The shear box must then be returned to its place in the frame if it has been moved to prepare the sample.

Consolidation and shearing

Each mixture was tested under three different normal stresses: 50, 100, and 200 kPa. Consolidation is considered complete when the vertical displacement stabilizes.

At the end of the consolidation, the two fixing screws of the two half-boxes are removed. Then, the sample is sheared at a constant speed of 1 mm/min until a horizontal displacement of approx. 7.5 mm is reached.

Results and Analysis

Influence of silt content

The results of direct shear tests conducted on sand-silt mixtures under a normal stress of 200 kPa are illustrated in Fig. 7. The shear stress (τ) evolution

Table 3. Experimental program

Test set	Fine fractions, F_c (%)	Glass fiber content, Sc (%)	Normal stress, σ (kPa)
1 st set	0; 10; 20, and 30	0	50; 100, and 200
2 nd set	0	0; 0.3; 0.5, and 0.8	
3 rd set	10; 20, and 30	0; 0.3; 0.5, and 0.8	

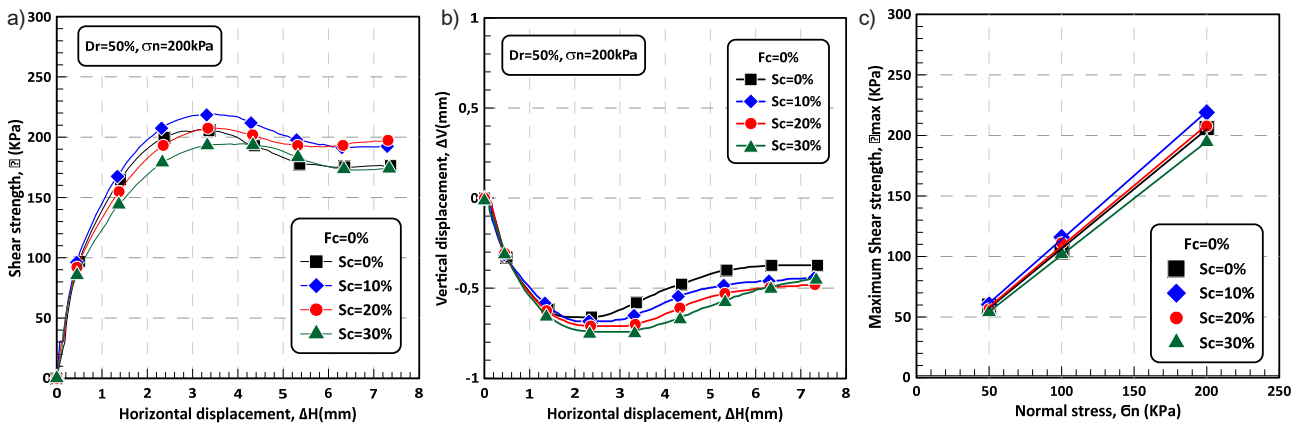


Fig. 7. Effect of silt content on the shear behavior of Chlef clean sand, $Dr = 50\%$, $\sigma_N = 200$ kPa: (a) variation of shear strength versus horizontal displacement, (b) variation of vertical displacement versus horizontal displacement, (c) intrinsic curve equation $\tau = \sigma \cdot \tan\phi + c$

curves show that all mixtures reach a maximum shear stress (τ_{max}) between approx. 2 and 5 mm of horizontal displacement (ΔH), after which the shear stress decreases slightly with the development of ΔH (Fig. 7a). Additionally, an increase in maximum shear strength is observed with increasing silt content up to 10 %, which represents a threshold content ($Sc_{th} = 10\%$). Beyond this point, the maximum shear strength decreases proportionally with increasing silt content (Fig. 7a). This result is in good agreement with those of Aouali et al. (2019) and Missoum Benziane et al. (2022). According to Belkhatir et al. (2010), the overall void ratio does not accurately represent the intergranular interface in sand-silt mixtures. When granular soil contains fines, the overall soil void ratio (e) can no longer accurately describe soil behavior. Below the threshold, fines only occupy the void spaces and do not significantly affect the mechanical behavior of the mixture. However, if the fines content increases beyond the threshold level, the behavior of the soil is governed by the fine matrix, and the coarse grains float in the fines. The interchange of this governing role can be expressed through the intergranular void ratio concept (Fig. 8). The intergranular void ratio e_s is defined according to Monkul and Ozden (2007) as the following relationship:

$$e_s = \frac{e + \frac{G \cdot Fc}{G_f \cdot 100}}{\frac{G}{G_s} \left(1 - \frac{Fc}{100}\right)},$$

where G_s and G_f are the specific gravity of the sand and finer grain matrices forming the soil, respectively. G is the specific gravity of the soil. G values are assumed to be the weighted average of the specific gravities of the grain matrices forming the mixtures.

The curves showing vertical displacement versus horizontal displacement for medium-density sand-silt mixtures under a confining pressure of 200 kPa

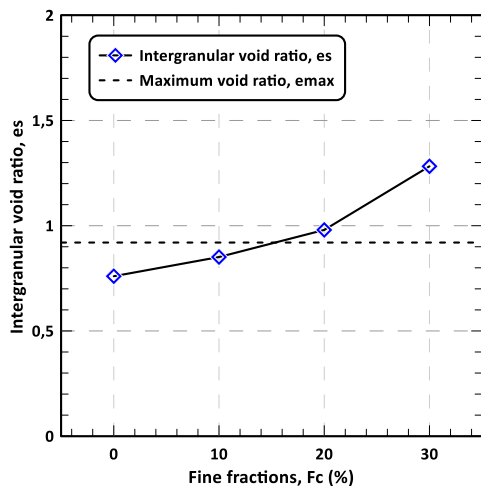


Fig. 8. Variation of intergranular void ratio versus fine fraction

are depicted in Fig. 7b. The results obtained show an increase in the contractive nature of the silty sand soil with the addition of silt content. Yamamuro and Lade (1997) attributed this behavior to the tendency of fines to occupy the void spaces after shearing, which generates a contractive behavior that results in the phenomenon of static liquefaction under undrained conditions.

Fig. 7c represents the evolution of maximum shear strength as a function of normal stress and silt content. It is clear that the maximum shear strength of the samples increased with increasing normal stress. However, sand-silt mixtures showed a decrease in maximum shear strength values after reaching the threshold fines content. Additionally, the shear strength parameters of sand-silt mixtures, obtained from the Mohr–Coulomb failure envelope (Fig. 7c) and summarized in Table 4, indicate that an increase in silt content leads to an increase in cohesion and internal friction angle up to a silt content of 10 %. After this point, the cohesion and friction angle of the mixture decrease. Missoum Benziane et al. (2022) attributed this loss of strength to the large volume that silt occupies in the voids between sand grains, causing them to dissociate and preventing them from interacting with each other.

Influence of fiber content

Fig. 9 illustrates the effect of glass fibers on the shear strength behavior of sand at a relative density of 50 % under a normal stress of 200 kPa. It has been found that the shear stress of unreinforced and fiber-reinforced sand increases steadily until it reaches its maximum value, and then it begins to decrease slightly with the development of horizontal displacement until the end of the test (Fig. 9a). Furthermore, it should be noted that the maximum shear strength (τ_{max}) increases with increasing fiber content up to 0.5 % (Fig. 9a). Once the optimal fiber content is exceeded, the maximum shear strength of the sand-fiber composite decreases. Wei et al. (2018) stated that this behavior is attributed to the reinforcing mechanism of fibers. Initially, fiber-reinforced specimens show an increase in strength due to the rise in interfacial friction between the soil particles and fibers. As the shearing process continues, the shear stresses in the soil mobilize tensile resistance in the fibers, which in turn imparts greater strength to the soil. At the same time, fibers produce numerous crossing sites and form fiber networks that create a spatial confinement effect on the soil, resulting in an increase in the composite strength to its maximum. However, after reaching peak strength, the fiber content exceeds the permissible value, leading to an uneven distribution of fibers due to overlapping and stacking. This creates weak interfaces that decrease the resistance of the soil-fiber mixture.

The variation of the vertical displacement (ΔV) of the sand-glass fiber mixtures as a function of the

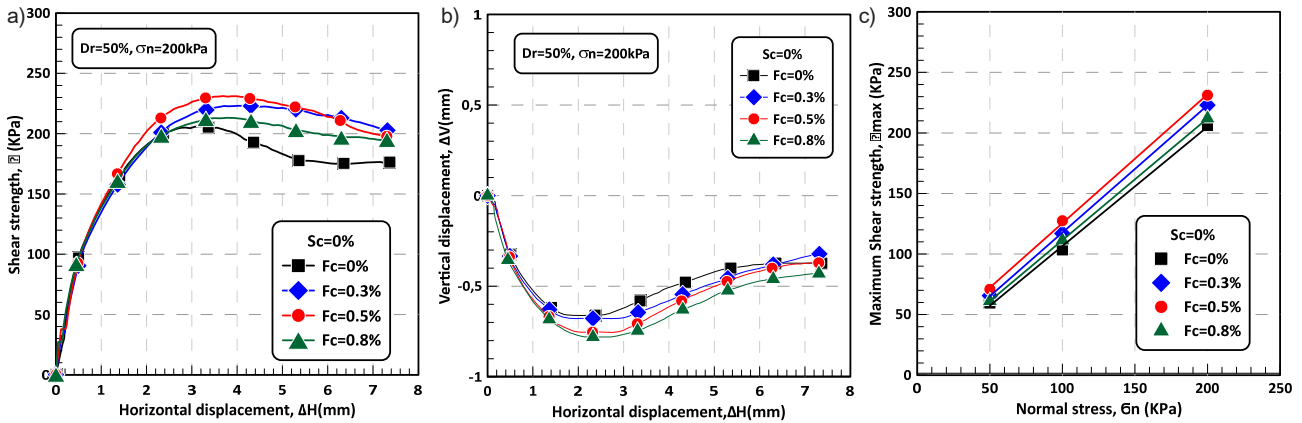


Fig. 9. Effect of fiber content on the shear behavior of Chlef clean sand, $Dr = 50\%$, $\sigma_N = 200$ kPa: (a) variation of shear strength versus horizontal displacement, (b) variation of vertical displacement versus horizontal displacement, (c) intrinsic curve equation $\tau = \sigma \tan\phi + c$

horizontal displacement (ΔH) is presented in Fig. 9b. All specimens initially show a contraction phase until a threshold is reached, at approx. 2 to 3 mm of horizontal displacement, after which a slight increase in their volume is noted. Additionally, adding glass fiber to the sand promotes its contractive behavior. This can be attributed to the role of fibers in improving the soil confinement stress. A similar observation was made by Romero (2003).

Fig. 9c illustrates the evolution of maximum shear strength as a function of fiber content (F_c) and normal stress (σ_n). It can be observed from this figure that the maximum shear resistance increases proportionally with increasing normal stress, and that the optimal fiber content is 0.5% ($F_{c_{opt}} = 0.5\%$), which provides the best shear resistance for the three normal stresses. The shear strength parameters obtained from the Mohr–Coulomb failure envelope for the sand-fiber mixtures are presented in Table 4. An increase in the internal friction angle and cohesion of the sand-fiber mixture is observed when the fiber content increases from 0 to 0.5%. This can be attributed to the special confinement effect of the fiber network. These results are in good agreement with those found by Benziane et al. (2022). Increasing the fiber content beyond 0.5% leads to opposite results.

Influence of silt-fiber combination

The results of direct shear tests carried out on unreinforced and fiber-reinforced sand-silt mixtures, at an initial density of 50% under a constant normal stress of 200 kPa, are presented

in Figs. 10, 11, and 12. The evolution of the shear strength of unreinforced and reinforced sand-silt mixtures as a function of horizontal displacement (ΔH) shows that it increases significantly at the beginning until reaching a maximum value, then it gradually decreases with the development of horizontal displacement (Fig. 10). Fig. 10a shows that the maximum shear stress of the mixture containing 10% silt ($Sc = 10\%$) increases with the rising fiber content from 0 to 0.5% ($F_{c_{opt}} = 0.5\%$), and then decreases when the fiber content increases to 0.8%. The same trend is observed for sand-silt mixtures containing 20% and 30% silt ($Sc = 20\%$ and 30%) (Figs 10b and 10c). However, it can be seen from Fig. 10 that the maximum shear strength of fiber-reinforced sand-silt mixtures increases with an increase in silt content until it reaches a ratio of 20%. Then it starts to decrease. This result is due to an opposing effect between the fines matrix and the fiber inclusions. As mentioned earlier, when the fines content exceeds the threshold, the fines matrix dissociates the sand grains and prevents their interaction, leading to a decrease in strength. The fines matrix governs the behavior of the entire specimen. Conversely, fiber inclusion increases the contact area between the sand grains as a consequence of the confining effect of the fiber network, reducing the influence of the fines matrix and therefore increasing the strength of the sand-silt-fiber composite. The shear strength behavior of fiber-reinforced sand-silt mixtures is mainly

Table 4. Shear strength parameters of unreinforced and fiber-reinforced sand-silt mixtures

Fiber content	Sc = 0 %		Sc = 10 %		Sc = 20 %		Sc = 30 %	
	c (kPa)	f (°)	c (kPa)	f (°)	c (kPa)	f (°)	c (kPa)	f (°)
Fc = 0 %	8.14	44.54	8.74	46.52	8.55	45.01	7.99	42.9
Fc = 0.3 %	12.63	46.41	13.91	46.61	11.59	45.17	10.81	43.2
Fc = 0.5 %	19.05	46.78	14.71	47.19	15.26	45.85	11.12	44.12
Fc = 0.8 %	10.8	45.16	13.55	45.75	12.86	44.95	4.6	43.5

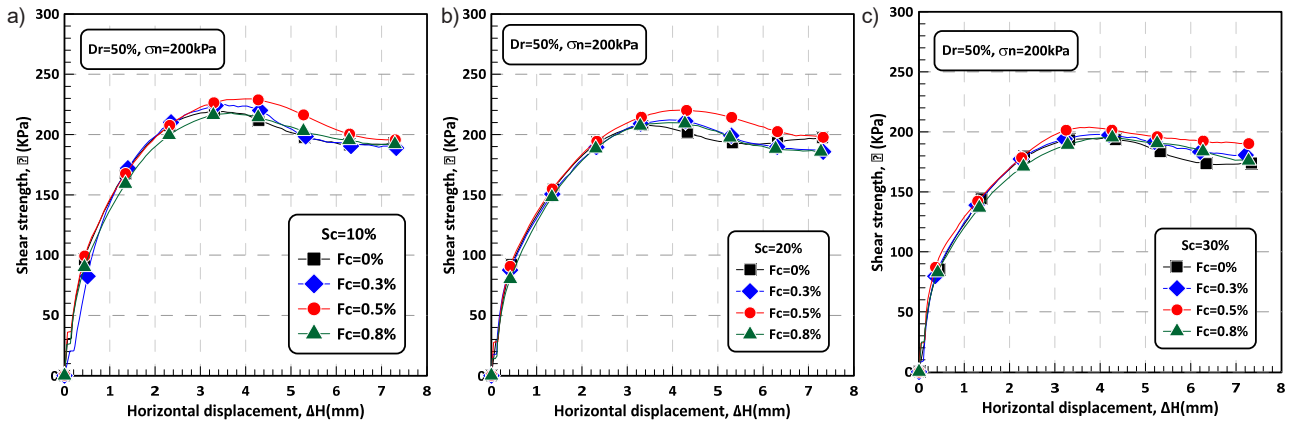


Fig. 10. Shear strength versus horizontal displacement of Chlef sand-silt mixtures reinforced with glass fibers: (a) $Sc = 10\%$, (b) $Sc = 20\%$, (c) $Sc = 30\%$

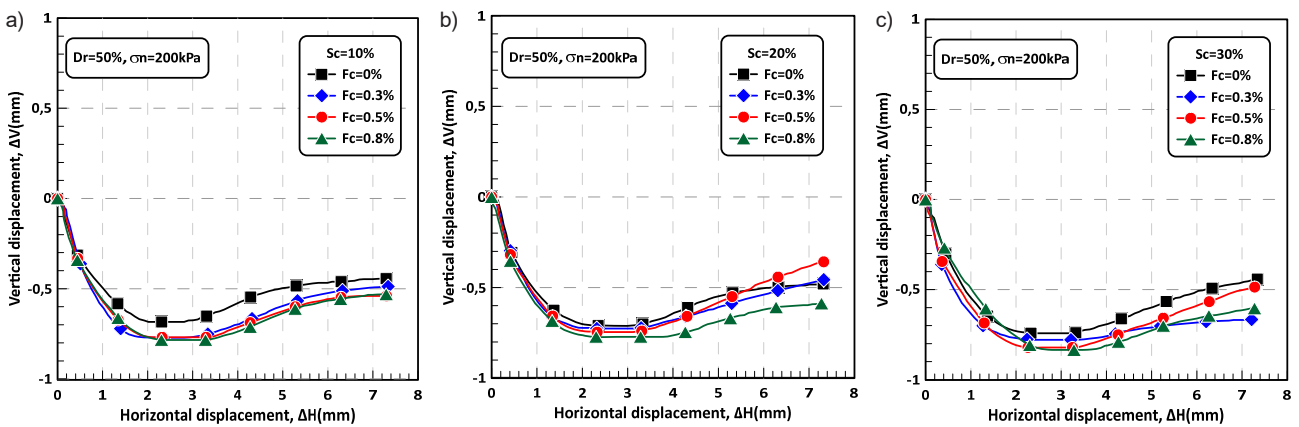


Fig. 11. Vertical displacement versus horizontal displacement of Chlef sand-silt mixtures reinforced with glass fibers: (a) $Sc = 10\%$, (b) $Sc = 20\%$, (c) $Sc = 30\%$

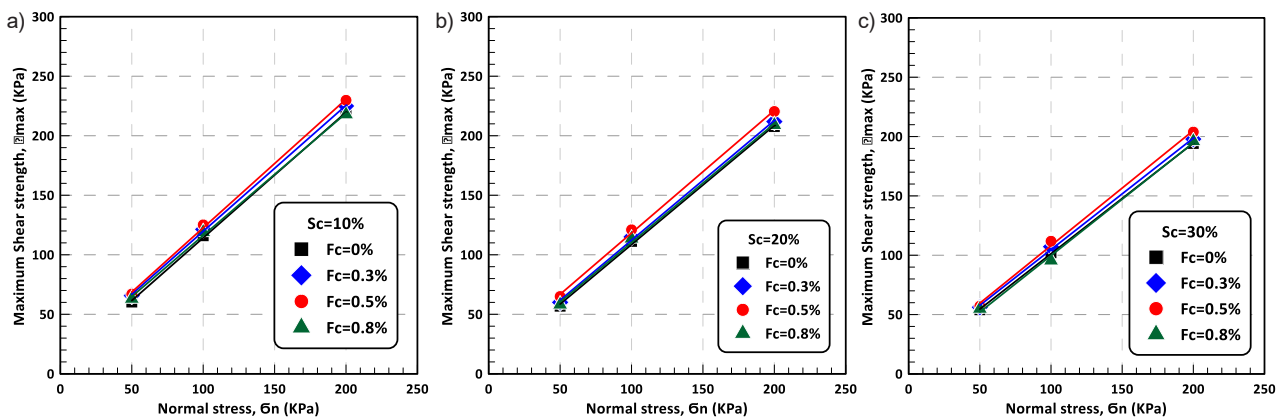


Fig. 12. Variation of maximum shear stress versus normal stress of Chlef sand-silt mixtures reinforced with glass fibers: (a) $Sc = 10\%$, (b) $Sc = 20\%$, (c) $Sc = 30\%$

governed by the silt threshold content and the optimum fiber content. It was found that the specimens with the most unsatisfactory results were those with $Sc_{th} > 20\%$ and $Fc_{opt} = 0.5\%$.

The variation of vertical displacement of unreinforced and fiber-reinforced sand-silt samples as a function of horizontal displacement

is shown in Fig. 11. It is clear that all samples generally exhibit a contractive character followed by a dilative one at approx. 2–3 mm of horizontal displacement. The figure also shows that an increase in fiber content and silt content tends to accentuate the contractive behavior of fiber-reinforced sand-silt mixtures.

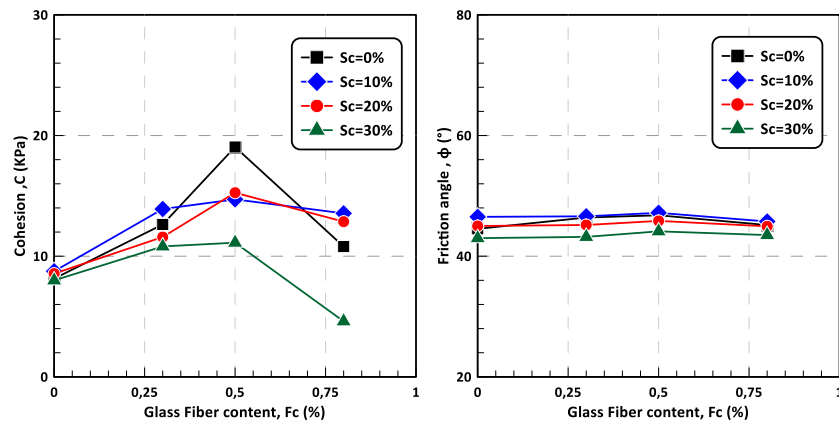


Fig. 13. Evolution of cohesion and friction angle as a function of silt content and glass fiber content

Fig. 12 represents the variation of the intrinsic curves for unreinforced and fiber-reinforced silty sand. The silty sand containing 0.5 % fiber generally exhibits the highest maximum shear stress ($F_{c_{opt}} = 0.5$ %), regardless of silt content or applied normal stress. The maximum shear stress for sand-silt mixtures reinforced with fibers increases with an increase in silt content from 10 % to 20 %, then decreases at 30 %. Fig. 13 shows the variation of shear strength coefficients for unreinforced and fiber-reinforced sand-silt mixtures, as summarized in Table 4, as a function of fines content and fiber inclusion. It can be noted that adding 10 % to 20 % silt to the sand, along with a 0.5 % increase in fibers, generally enhances the cohesion and internal friction of the sand-silt mixture. However, a further increase in fines content to 30 % leads to a decrease in both shear strength parameters, even with an increase in fiber content. This decrease in resistance is probably due to the presence of fine particles between the grains of sand, which promotes a reduction in the contact between sand particles. Arab (2009) found a similar trend in saturated sand. Additionally, Fig. 13 demonstrates that the shear strength parameters of sand-silt mixtures increase with the rising fiber content from 0 % to 0.5 %, and then decrease as the fiber content increases to 0.8 %.

Discussion

An experimental investigation was conducted to study the effects of glass fiber and silt content, as well as their combined effect, on the shear behavior of silty sand. Direct shear tests were conducted on sand mixed with different percentages of silt (0 %, 10 %, 20 %, and 30 %) and glass fibers (0 %, 0.3 %, 0.5 %, and 0.8 %). Samples were prepared with an initial relative density of 50 %, and each mixture was tested under three normal stresses (50, 100,

and 200 kPa). Based on the experimental evidence, the following conclusions can be drawn:

The silt content has a significant effect on the shear behavior of the sand-silt mixture. Indeed, adding 10 % silt to sand increases its shear strength, cohesion, and friction angle. Beyond the threshold content ($Sc = 10$ %), a further increase in the silt content leads to an opposite trend.

The shear strength and shear strength characteristics of fiber-reinforced sand increase with increasing fiber content up to an optimum content of 0.5 %. On the other hand, the addition of glass fiber reinforces the contractive nature of the sand.

The shear behavior of fiber-reinforced silty sand is mainly governed by the silt and fiber content. The results obtained indicate that 0.5 % of glass fibers is the optimum content, which can be used to improve the shear strength of sand-silt mixtures and their shear strength parameters. However, it is necessary to consider the increase in the contractive behavior of the mixture when adding glass fibers.

Reinforcing silty sand with fibers is a promising solution for problematic soils because of the presence of fines fractions. Further studies on the subject should be carried out to assess the influence of other parameters on its shear response, such as relative density (loose and medium dense states), water content, and different types of fiber.

Acknowledgments

All tests were carried out in the Laboratory of Materials Science and Environment at the Hassiba Benbouali University of Chlef, Algeria. The authors express their gratitude to the technicians who contributed to this experimental program.

Funding

This work was supported by the General Directorate for Scientific Research and Technological Development (DGRSDT) in Algeria.

References

- Ahmad, F., Mujah, D., Hazarika, H., and Safari, A. (2012). Assessing the potential reuse of recycled glass fibre in problematic soil applications. *Journal of Cleaner Production*, Vol. 35, pp. 102–107. DOI: 10.1016/j.jclepro.2012.05.047.
- Aouali, N., Benessalah, I., Arab, A., Ali, B., & Abed, M. (2019). Shear strength response of fibre reinforced Chlef (Algeria) silty sand: laboratory study. *Geotechnical and Geological Engineering*, Vol. 37, Issue 2, pp. 1047–1057. DOI: 10.1007/s10706-018-0641-5.
- Arab, A. (2009). Comportement monotone et cyclique d'un sable limoneux. On monotonic and cyclic behavior of silty sand. *Comptes Rendus Mécanique*, Vol. 337, Issue 8, pp. 621–631. DOI: /10.1016/j.crme.2009.08.001.
- Belkhatir, M., Arab, A., Della, N., Missoum, H., & Schanz, T. (2010). Influence of inter-granular void ratio on monotonic and cyclic undrained shear response of sandy soils. *Comptes rendus. Mécanique*, 338(5), 290-303.
- Belkhatir, M., Schanz, T., Arab, A., & Della, N. (2014). Experimental study on the pore water pressure generation characteristics of saturated silty sands. *Arabian Journal for Science and Engineering*, 39, 6055-6067.
- Benessalah, I., Arab, A., Villard, P., Sadek, M., and Kadri, A. (2016). Laboratory study on shear strength behaviour of reinforced sandy soil: effect of glass-fibre content and other parameters. *Arabian Journal for Science and Engineering*, Vol. 41, pp. 1343–1353. DOI: 10.1007/s13369-015-1912-6.
- Benziane, M. M., Della, N., Denine, S., Sert, S., and Nouri, S. (2019). Effect of randomly distributed polypropylene fiber reinforcement on the shear behavior of sandy soil. *Studia Geotechnica et Mechanica*, Vol. 41, Issue 3, pp. 151–159. DOI: 10.2478/sgem-2019-0014.
- Benziane, M. M., Della, N., Sert, S., Denine, S., Nouri, S., Bol, E., and Elroul, A. B. (2022). Shear behaviour of sandy soil from Chlef river reinforced with different types of fibres. *Marine Georesources & Geotechnology*, Vol. 40, Issue 10, pp. 1232–1241. DOI: 10.1080/1064119X.2021.1984619.
- Bouaricha, L., Henni, A. D., and Lancelot, L. (2017). A laboratory investigation on shear strength behavior of sandy soil: effect of glass fiber and clinker residue content. *Studia Geotechnica et Mechanica*, Vol. 39, Issue 4, pp. 3–15. DOI: 10.1515/sgem-2017-0032.
- Chen, C. W. and Loehr, J. E. (2008). Undrained and drained triaxial tests of fiber-reinforced sand. In: *Li, G., Chen, Y., and Tang, X. (eds.). Geosynthetics in Civil and Environmental Engineering*. Berlin, Heidelberg: Springer, pp. 114–120. DOI: 10.1007/978-3-540-69313-0_25.
- Consoli, N. C., Heineck, K. S., Casagrande, M. D. T., & Coop, M. R. (2007). Shear strength behavior of fiber-reinforced sand considering triaxial tests under distinct stress paths. *Journal of Geotechnical and Geoenvironmental Engineering*, Vol. 133, Issue 11, pp. 1466–1469. DOI: 10.1061/(ASCE)1090-0241(2007)133:11(1466).
- Consoli, N. C., Montardo, J. P., Donato, M., and Prietto, P. D. (2004). Effect of material properties on the behaviour of sand—cement—fibre composites. *Proceedings of the Institution of Civil Engineers - Ground Improvement*, Vol. 8, Issue 2, pp. 77–90. DOI: 10.1680/grim.2004.8.2.77.
- Consoli, N. C., Prietto, P. D. M., and Ulbrich, L. A. (1998). Influence of fiber and cement addition on behavior of sandy soil. *Journal of Geotechnical and Geoenvironmental Engineering*, Vol. 124, Issue 12, pp. 1211–1214. DOI: 10.1061/(ASCE)1090-0241(1998)124:12(1211).
- Della, N., Arab, A., and Belkhatir, M. (2011). A laboratory study of the initial structure and the overconsolidation effects on the undrained monotonic behavior of sandy soil from Chlef region in northern Algeria. *Arabian Journal of Geosciences*, Vol. 4, Issue 5–6, pp. 983–991. DOI: 10.1007/s12517-010-0178-2.
- Della, N., Belkhatir, M., Arab, A., Canou, J., and Dupla, J.-C. (2014). Effect of fabric method on instability behavior of granular material. *Acta Mechanica*, Vol. 225, Issue 7, pp. 2043–2057. DOI: 10.1007/s00707-013-1083-z.
- Derradji, M., Wang, J., and Liu, W. (2018). Fiber-reinforced phthalonitrile composites. *Phthalonitrile Resins and Composites*, pp. 241–294. DOI: 10.1016/B978-0-12-812966-1.00005-6.
- Diambra, A., Ibraim, E., Wood, D. M., and Russell, A. R. (2010). Fibre reinforced sands: Experiments and modelling. *Geotextiles and Geomembranes*, Vol. 28, Issue 3, pp. 238–250. DOI: 10.1016/j.geotextmem.2009.09.010.
- Durville, J. L. and Meneroud, J. P. (1982). Phenomenes geomorphologiques induits par le seisme d'El Asnam, Algerie - comparaison avec le seisme de Campanie, Italie. *Bull Liaison Lab Ponts Chauss*, Issue 120, pp. 13–23.
- Gray, D. H., & Al-Refeai, T. (1986). Behavior of fabric-versus fiber-reinforced sand. *Journal of Geotechnical Engineering*, Vol. 112, Issue 8, pp. 804–820. DOI: 10.1061/(ASCE)0733-9410(1986)112:8(804).
- Han, J. (2015). *Principles and practice of ground improvement*. Hoboken: John Wiley & Sons, 432 p.
- Khebizi, W., Della, N., Denine, S., Canou, J., and Dupla, J.-C. (2019). Undrained behaviour of polypropylene fibre reinforced sandy soil under monotonic loading. *Geomechanics and Geoengineering*, Vol. 14, Issue 1, pp. 30–40. DOI: 10.1080/17486025.2018.1508855.

- Michalowski, R. L. and Čermák, J. (2003). Triaxial compression of sand reinforced with fibers. *Journal of Geotechnical and Geoenvironmental Engineering*, Vol. 129, Issue 2, pp. 125–136. DOI: /10.1061/(ASCE)1090-0241(2003)129:2(125).
- Missoum Benziane, M., Della, N., Bedr, S., Flitti, A., Kaddour Djebbar, M., and Baizid, M. (2022). Mechanical behavior of bio-cemented silty sand. *Arabian Journal of Geosciences*, Vol. 15, Issue 7, 577. DOI: 10.1007/s12517-022-09776-y.
- Monkul, M. M. and Ozden, G. (2007). Compressional behavior of clayey sand and transition fines content. *Engineering Geology*, Vol. 89, Issues 3–4, pp. 195–205. DOI: 10.1016/j.enggeo.2006.10.001.
- Rabab'ah, S., Al Hattamleh, O., Aldeeky, H., and Alfoul, B. A. (2021). Effect of glass fiber on the properties of expansive soil and its utilization as subgrade reinforcement in pavement applications. *Case Studies in Construction Materials*, Vol. 14, e00485. DOI: 10.1016/j.cscm.2020.e00485.
- Romero, R. J. (2003). *Development of a constitutive model for fiber-reinforced soils*. DSc Thesis.
- Safdar, M., Newson, T., Schmidt, C., Sato, K., Fujikawa, T., and Shah, F. (2020). Effect of fiber and cement additives on the small-strain stiffness behavior of Toyoura sand. *Sustainability*, Vol. 12, Issue 24, 10468. DOI: 10.3390/su122410468.
- Tang, C., Shi, B., Gao, W., Chen, F., and Cai, Y. (2007). Strength and mechanical behavior of short polypropylene fiber reinforced and cement stabilized clayey soil. *Geotextiles and Geomembranes*, Vol. 25, Issue 3, pp. 194–202. DOI: 10.1016/j.geotextmem.2006.11.002.
- Wei, L., Chai, S. X., Zhang, H. Y., and Shi, Q. (2018). Mechanical properties of soil reinforced with both lime and four kinds of fiber. *Construction and Building Materials*, Vol. 172, pp. 300–308. DOI: 10.1016/j.conbuildmat.2018.03.248.
- Yamamuro, J. A. and Lade, P. V. (1997). Static liquefaction of very loose sands. *Canadian Geotechnical Journal*, Vol. 34, No. 6, pp. 905–917. DOI: 10.1139/t97-057.

ИССЛЕДОВАНИЕ ПРОЧНОСТИ АРМИРОВАННОГО АЛЕВРИТОВОГО ПЕСКА НА СДВИГ

Фекнус Хаджер¹, Делла Нуреддин^{1*}, Денин Сидали², Миссум Бензиан Мехди¹, Флитти Абдельхамид¹, Серт Седат³, Эртан Боль³, Апкын Озоджак³

¹Лаборатория материаловедения и экологии, Университет имени Хассибы Бен Буали, Эш-Шелифф, Алжир

²Университетский центр Типазы, Типаза, Алжир

³Университет Сакарья, Сакарья, Турция

*E-mail: n.della@univ-chlef.dz

Аннотация

Введение: в данной работе представлено экспериментальное исследование, целью которого является изучение влияния содержания ила, содержания стекловолокна и их совместного воздействия на поведение алевритового песка при сдвиге. С этой **целью** использованы следующие **методы**: проведена серия испытаний песка, смешанного с различным содержанием ила и волокон, с использованием аппарата для испытания на сдвиг. Образцы были подготовлены с относительной плотностью 50 %, и каждая смесь проходила испытания при трех различных нормальных напряжениях. **Результаты** эксперимента показали увеличение прочности на сдвиг при содержании ила 10 %, а также последующее снижение прочности на сдвиг с увеличением содержания ила от 10 до 30 %. Также было установлено, что 0,5 % — это оптимальное содержание, которое может быть добавлено в песчано-иловые смеси для повышения их прочности на сдвиг и угла трения, хотя при этом смеси становятся более сжатыми.

Ключевые слова: песок, ил, стекловолокно, прочность на сдвиг, когезия, угол трения.

Guide for Authors

for submitting a manuscript for publication in the «Architecture and Engineering»

The journal is an electronic media and accepts the manuscripts via the online submission. Please register on the website of the journal <http://aej.spbgasu.ru/>, log in and press "Submit article" button or send it via email aejeditorialoffice@gmail.com.

Please ensure that the submitted work has neither been previously published nor has been currently submitted for publication in another journal.

Main topics of the journal:

1. Architecture
2. Civil Engineering
3. Geotechnical Engineering and Engineering Geology
4. Urban Planning
5. Technique and Technology of Land Transport in Construction

Title page

The title page should include:

The title of the article in bold (max. 90 characters with spaces, only conventional abbreviations should be used); The name(s) of the author(s); Author's(s') affiliation(s); The name of the corresponding author.

Abstract and keywords

Please provide an abstract of 100 to 250 words. The abstract should not contain any undefined abbreviations or unspecified references. Use the IMRAD structure in the abstract (introduction, methods, results, discussion).

Please provide 4 to 6 keywords which can be used for indexing purposes. The keywords should be mentioned in order of relevance.

Main text

It should have the following structure:

- 1) Introduction,
- 2) Scope, Objectives and Methodology (with subparagraphs),
- 3) Results and Discussion (may also include subparagraphs, but should not repeat the previous section or numerical data already presented),
- 4) Conclusions,
- 5) Acknowledgements (the section is not obligatory, but should be included in case of participation of people, grants, funds, etc. in preparation of the article. The names of funding organizations should be written in full).

General comments on formatting:

- Subtitles should be printed in Bold,
- Use MathType for equations,
- Tables should be inserted in separate paragraphs. The consecutive number and title of the table should be placed before it in separate paragraphs. The references to the tables should be placed in parentheses (Table 1),
- Use "Top and Bottom" wrapping for figures. Figure captions should be placed in the main text after the image. Figures should be referred to as (Fig. 1) in the text.

References

The journal uses Harvard (author, date) style for references:

- The recent research (Kent and Park, 1990)...
- V. Zhukov (1999) stated that...

Reference list

The list of references should only include works that are cited in the text and that have been published or accepted for publication. Personal communications and unpublished works should only be mentioned in the text. Do not use footnotes or endnotes as a substitute for a proper reference list. All references must be listed in full at the end of the paper in alphabetical order, irrespective of where they are cited in the text. Reference made to sources published in languages other than English or Russian should contain English translation of the original title together with a note of the used language.

Peer Review Process

Articles submitted to the journal undergo a double blind peer-review procedure, which means that the reviewer is not informed about the identity of the author of the article, and the author is not given information about the reviewer.

On average, the review process takes from one to five months.